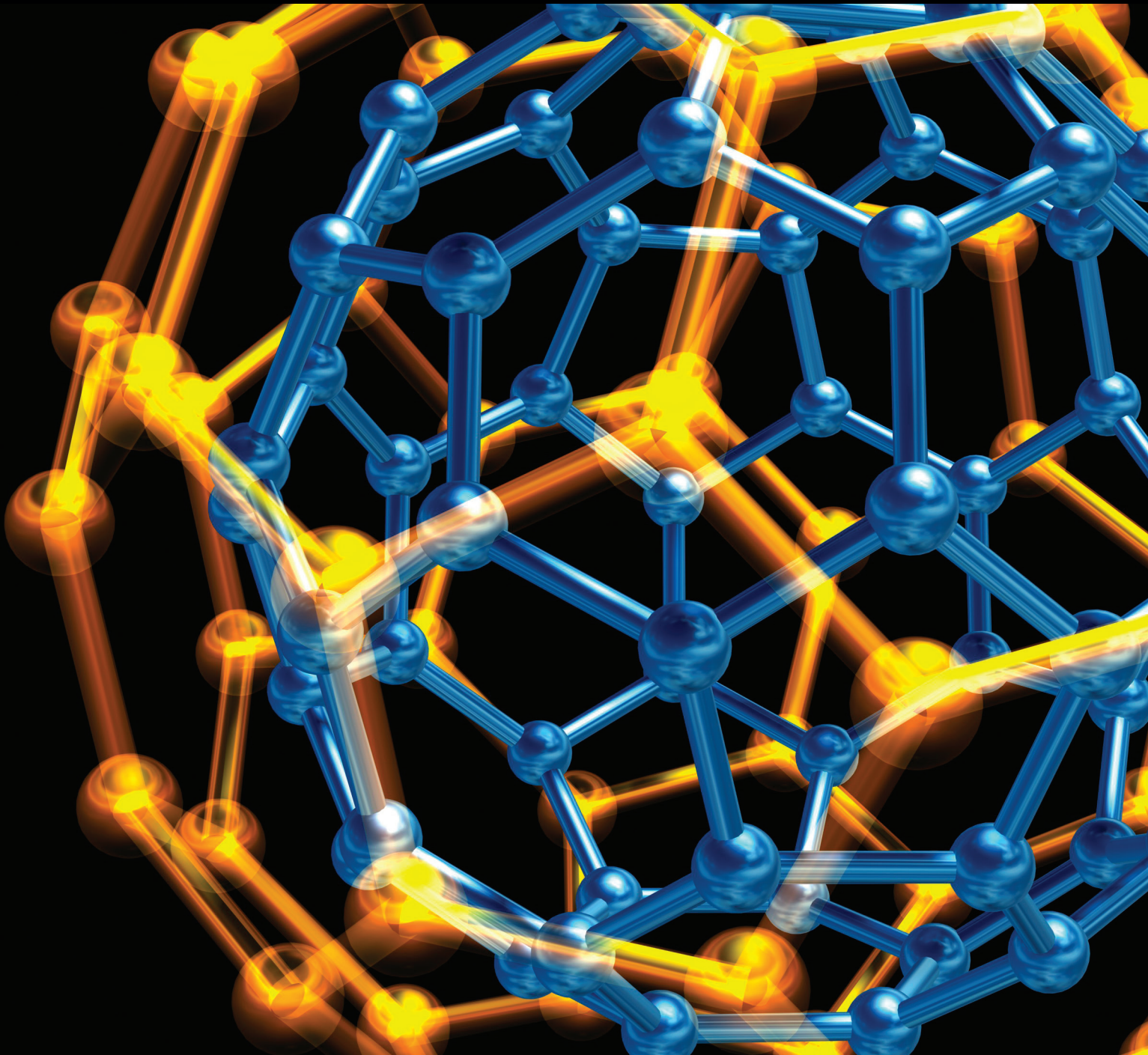


Journal of Nanotechnology

Nanomaterials for Sensing Applications

Guest Editors: Wen Zeng, Hua Wang, and Zhenyu Li





Nanomaterials for Sensing Applications

Journal of Nanotechnology

Nanomaterials for Sensing Applications

Guest Editors: Wen Zeng, Hua Wang, and Zhenyu Li



Copyright © 2016 Hindawi Publishing Corporation. All rights reserved.

This is a special issue published in "Journal of Nanotechnology." All articles are open access articles distributed under the Creative Commons Attribution License, which permits unrestricted use, distribution, and reproduction in any medium, provided the original work is properly cited.

Editorial Board

Simon Joseph Antony, UK
Carlos R. Cabrera, Puerto Rico
Franco Cerrina, USA
Gan Moog Chow, Singapore
Enkeleda Dervishi, USA
Dmitriy A. Dikin, USA
Dimitris Drikakis, UK
John S. Foord, UK
Joseph Irudayaraj, USA
Niraj K. Jha, USA

Miguel Jose-Yacamán, USA
Valery Khabashesku, USA
Sakhrat Khizroev, USA
Abdel Salam H. Makhlouf, Germany
Constantinos Mavroidis, USA
Paolo Milani, Italy
Oded Millo, Israel
Oussama Moutanabbir, Canada
M. Grant Norton, USA
Paresh Chandra Ray, USA

Benjaram M. Reddy, India
Mehmet Sarikaya, USA
Jorge M. Seminario, USA
V. Shalaev, USA
Mahi R. Singh, Canada
Xiaowei Sun, Singapore
Boris I. Yakobson, USA
Nan Yao, USA
Yoke K. Yap, USA
Chuan Jian Zhong, USA

Contents

Nanomaterials for Sensing Applications

Wen Zeng, Hua Wang, and Zhenyu Li
Volume 2016, Article ID 2083948, 2 pages

Nonenzymatic Glucose Biosensors Based on Silver Nanoparticles Deposited on TiO₂ Nanotubes

Zheng Li, Yong Zhang, Jiaye Ye, Meiqing Guo, Jing Chen, and Weiyi Chen
Volume 2016, Article ID 9454830, 7 pages

Hydrothermal Synthesis and Responsive Characteristics of Hierarchical Zinc Oxide Nanoflowers to Sulfur Dioxide

Qu Zhou, Bo Xie, Lingfeng Jin, Weigen Chen, and Jian Li
Volume 2016, Article ID 6742104, 6 pages

Structural and Electrical Studies on ZnO-Based Thin Films by Laser Irradiation

Shanyue Zhao, Yinqun Hua, Ruifang Chen, Jian Zhang, and Ping Ji
Volume 2016, Article ID 9385725, 6 pages

Amorphous Silicon-Germanium Films with Embedded Nanocrystals for Thermal Detectors with Very High Sensitivity

Cesar Calleja, Alfonso Torres, Pedro Rosales-Quintero, and Mario Moreno
Volume 2016, Article ID 5807940, 9 pages

Nanosensing Backed by the Uncertainty Principle

I. Filikhin, A. Karoui, and B. Vlahovic
Volume 2016, Article ID 3794109, 8 pages

Research on Acetylene Sensing Properties and Mechanism of SnO₂ Based Chemical Gas Sensor Decorated with Sm₂O₃

Qu Zhou, Meiqing Cao, Wude Li, Chao Tang, and Shiping Zhu
Volume 2015, Article ID 714072, 7 pages

Optical and Sensing Properties of Cu Doped ZnO Nanocrystalline Thin Films

R. K. Shukla, Anchal Srivastava, Nishant Kumar, Akhilesh Pandey, and Mamta Pandey
Volume 2015, Article ID 172864, 10 pages

Editorial

Nanomaterials for Sensing Applications

Wen Zeng,¹ Hua Wang,² and Zhenyu Li³

¹College of Materials Science and Engineering, Chongqing University, Chongqing 400040, China

²School of Chemistry and Environment, Beihang University, Beijing 100083, China

³Institute for Frontier Materials, Deakin University, Geelong, VIC 3216, Australia

Correspondence should be addressed to Wen Zeng; wenzeng@cqu.edu.cn

Received 12 June 2016; Accepted 13 June 2016

Copyright © 2016 Wen Zeng et al. This is an open access article distributed under the Creative Commons Attribution License, which permits unrestricted use, distribution, and reproduction in any medium, provided the original work is properly cited.

Sensor played a huge role in the field of preventing the fire explosion accident, atmospheric environmental testing, and the industrial production of poisonous and harmful gas detection. However, at present the development of sensitive material is still obvious deficiencies in selectivity, stability, and other aspects; therefore, the research and development of new high performance sensors will have very important realistic meaning and practical value.

The performance of sensing materials depends critically on their microstructures, which requires the development of materials processing techniques to obtain the desired microstructures and morphologies. It is of great importance in future technological applications to understand how the materials behave at nanoscale during working and how controllably are manufactured. No matter physical or chemical preparation, forward-looking theoretical guidance and characterization proof are necessary for explaining the formation mechanism so as to design devices with expected sensing properties. In this issue, different approaches were used to create nanostructures in several nanomaterials to deal with the sensing application.

In the paper “Hydrothermal Synthesis and Responsive Characteristics of Hierarchical Zinc Oxide Nanoflowers to Sulfur Dioxide” Q. Zhou et al. prepare hierarchical ZnO nanoflowers through a simple hydrothermal process and report systematically their responsive characteristics to SO₂ and demonstrate that the sensor fabricated with hierarchical ZnO nanoflowers is a promising candidate for detecting SO₂. In the paper “Structural and Electrical Studies on ZnO-Based Thin Films by Laser Irradiation” S. Zhao et al. studied the structural and electrical properties of the ZnO-based thin film varistors for low-voltage application. They found

that the pressure-sensitive electrical properties of ZnO-based ceramic film of laser irradiation state show excellent property. In the paper “Amorphous Silicon-Germanium Films with Embedded Nanocrystals for Thermal Detectors with Very High Sensitivity” C. Calleja et al. optimized the deposition conditions of amorphous silicon-germanium films with embedded nanocrystals in a plasma enhanced chemical vapor deposition (PECVD) reactor, working at a standard frequency of 13.56 MHz. The results show optimized deposition conditions of amorphous silicon-germanium films with embedded nanocrystals in a plasma enhanced chemical vapor deposition (PECVD) reactor, working at a standard frequency of 13.56 MHz.

In the paper “Nanosensing Backed by the Uncertainty Principle” I. Filikhin et al. studied spectral distributions of localized/delocalized states of a single electron in a double quantum well (DQW) with relation to slight asymmetry perturbations and demonstrated that the DQW is a quantum system suitable for sensing tiny substances adsorbed on one of the quantum dots constituting the DQW or by a defect in one of the dots.

The paper “Research on Acetylene Sensing Properties and Mechanism of SnO₂ Based Chemical Gas Sensor Decorated with Sm₂O₃” by Q. Zhou et al. reports the successful preparation and characterization of samarium oxide Sm₂O₃ decorated tin oxide SnO₂ based sensors with hierarchical rod structure for C₂H₂ gas detection. The obtained materials show an excellent gas sensing performance.

In the paper “Optical and Sensing Properties of Cu Doped ZnO Nanocrystalline Thin Films” R. K. Shukla et al. synthesized nanocrystalline Cu doped ZnO films deposited on glass substrates by spray pyrolysis. They found that

the crystallite size decreases with increase in molarity of precursor solution whereas with doping the crystallite size increases in general. Doping increases the transmittance of the films whereas optical band gap first decreases and then increases as the dopant concentration is gradually increased for both molarities in reference.

By compiling these papers, we hope that this issue will provide some valuable insight to our readers and researchers with respect to field of nanomaterials for sensing applications.

*Wen Zeng
Hua Wang
Zhenyu Li*

Research Article

Nonenzymatic Glucose Biosensors Based on Silver Nanoparticles Deposited on TiO₂ Nanotubes

Zheng Li,^{1,2,3} Yong Zhang,⁴ Jiaye Ye,¹ Meiqing Guo,^{1,3} Jing Chen,¹ and Weiyi Chen^{2,3}

¹College of Mechanics, Taiyuan University of Technology, Taiyuan 030024, China

²Institute of Applied Mechanics and Biomedical Engineering, Taiyuan University of Technology, Taiyuan 030024, China

³Shanxi Key Laboratory of Material Strength and Structural Impact, Taiyuan University of Technology, Taiyuan 030024, China

⁴Academic Affairs Office, Taiyuan University of Technology, Taiyuan 030024, China

Correspondence should be addressed to Meiqing Guo; gmgg82@sina.com and Jing Chen; 1165059779@qq.com

Received 17 September 2015; Revised 7 December 2015; Accepted 13 December 2015

Academic Editor: Thomas Thundat

Copyright © 2016 Zheng Li et al. This is an open access article distributed under the Creative Commons Attribution License, which permits unrestricted use, distribution, and reproduction in any medium, provided the original work is properly cited.

In the present research, a nonenzymatic glucose biosensor was fabricated by depositing Ag nanoparticles (Ag-NPs) using in situ chemical reduction method on TiO₂ nanotubes which were synthesized by anodic oxidation process. The structure, morphology, and mechanical behaviors of electrode were examined by scanning electron microscopy and nanoindentation. It was found that Ag-NPs remained both inside and outside of TiO₂ nanotubes whose length and diameter were about 1.2 μm and 120 nm. The composition was constructed as an electrode of nonenzymatic biosensor for glucose oxidation. The electrocatalytic properties of the prepared electrodes for glucose oxidation were investigated by cyclic voltammetry (CVs) and differential pulse voltammetry (DPV). Compared with bare TiO₂ and Ag-fresh TiO₂ nanotube, Ag-TiO₂/(500°C) nanotube exhibited the best electrochemical properties from cyclic voltammetry (CVs) results. Differential pulse voltammetry (DPV) results showed that, at +0.03 V, the sensitivity of the electrode to glucose oxidation was 3.69 mA · cm⁻² · mM⁻¹ with a linear range from 20 mM to 190 mM and detection limit of 24 μM (signal-to-noise ratio of 3). In addition the nonenzymatic glucose sensors exhibited excellent selectivity, stability, and repeatability.

1. Introduction

The blood glucose detection is of great significance in the application of food process, clinical medicine, and biology [1–3]. In particular accurate glucose determination for diabetics can be very effective to the detection and treatment of diabetes mellitus [4]. The glucose oxidase (GOD) analytical method is the first and most commonly used way for glucose detection in clinical trials [5, 6]. However, the entity of GOD is enzyme which is easily inactive and denatured, resulting in poor stability and repeatability of enzymatic electrodes [7, 8].

Nonenzymatic glucose biosensors can avoid that problem because of direct catalyzed oxidation to glucose on the surface of electrode [9–11]. In order to increase specific surface areas and enhance mass transport ability, these electrodes could use nanomaterials as substrates like carbon nanotubes (CNTs) [12], nanowires [13], mesoporous structure [14], and so forth and decorate with mental nanoparticles such as Pt [15], Ni [16], Ag [17], and Cu [18].

TiO₂ nanotube has been paid more and more attention in chemical reactions and biosensor fields because of their well-aligned nanostructure, large surface area property, thermal stability, chemical inertness, and nontoxicity [19, 20]. Recently, silver doped TiO₂ nanocomposite structures have attracted much attention not only because TiO₂ is a promising material with desirable electronic, but also because Ag displays some unique activities in chemical and biological sensing compared with the other noble metals such as Ru and Pt [19]. However, the electrocatalytic activity of Ag doped TiO₂ nanotubes has not been subjected to intensive report.

Many approaches were developed to fabricate different sizes of Ag doped TiO₂ nanotubes such as sol-gel, “wet” chemical, and ceramic methods. However, drying, heating, or annealing at high temperatures is revolved in the preparation process [21, 22]. In order to modify the TiO₂ nanotubes by Ag nanoparticles, a polyol method at low temperature has been developed. The polyol process was that using polyol such as diethylene glycol [23] and glycerol [24] both as

solvent and reducing agent during reaction which can be conducive to the formation of nanostructures. The Ag^+ ions from silver nitrate (AgNO_3) can be reduced to metallic Ag. The Ag nanoparticles were deposited successfully on the surface of TiO_2 . Moreover the specific surface area will be hugely increased by silver nanoparticles deposited on TiO_2 nanotubes. So TiO_2 nanotubes decorated with silver nanoparticles possess distinct advantages for nonenzymatic glucose sensors.

In this work, the Ag nanoparticles were deposited successfully on the surface of TiO_2 by polyol process. Scanning electron microscope (SEM) and nanoindentation were used for characterization. Furthermore, the electrocatalytic activity of the Ag- TiO_2 electrode was also evaluated by cyclic voltammetry (CVs) and differential pulse voltammetry (DPV).

2. Experimental

2.1. Reagents. Titanium sheet (15 mm * 10 mm * 1 mm) was provided by Tianjin Pengbo Company, China. All of the other chemicals, including glycerol, ammonium fluoride (NH_4F), sodium borohydride (NaBH_4), silver nitrate (AgNO_3), Na_2HPO_4 , NaH_2PO_4 , H_3PO_4 , poly(vinylpyrrolidone) (PVP), and KCl, were of analytical grade and used as received. A 0.1 M phosphate buffer solution (PBS) prepared using Na_2HPO_4 and NaH_2PO_4 was employed as supporting electrolyte. The desired pH of solution was adjusted with 0.1 M NaOH or 0.1 M H_3PO_4 . All aqueous solution was prepared with reagent grade chemicals and double distilled water.

2.2. Apparatus. All the electrochemical measurements were performed on a CH instrument 660E electrochemical workstation (ChenHua Instruments Co. Ltd., Shanghai, China). Scanning electron microscope (FE-SEM, Hitachi S-4800) was used to determine the morphology and composition of the samples. Nanoindentation (NanoIndenter G200, USA) was used to determine the mechanical properties. All measurements were conducted at room temperature.

2.3. Synthesis of TiO_2 Nanotube Arrays on Ti Substrate. Before use, the titanium foils were polished with abrasive paper of 400#, 600#, and 800# until the surfaces were smooth and remained with no scratch and then ultrasonically cleaned in alcohol and double distilled water for 10 min, respectively, and dried in air eventually. Then, titanium sheets were used as the substrate electrode with Pt electrodes as cathode. Samples were anodized in water/glycerol (1:1 Vol.%) mixtures containing 0.3 M NH_4F at a potential of 30 V for 3 h. Finally, the as-prepared TiO_2 nanotube electrode was annealed at 500°C (10°C/min) under nitrogen atmosphere for 2 h.

2.4. Preparation of Ag Nanoparticles on TiO_2 Nanotubes. Ag nanoparticles on TiO_2 nanotubes were prepared by the following process. Firstly, 1 mL AgNO_3 (0.04 M) was mixed with 10 mL PVP (0.01 M) and stirred with ice-bath after adding 50 mL water to the solution. Then, 1 mL NaBH_4 (0.06 M) was dropped quickly into the solution with colour turning brown,

by stirring for 10 min. At last, the above-prepared TiO_2 nanotubes (500°C) were entirely immersed in this electrolyte under static conditions for 7 h and subsequently rinsed with double distilled water and air-dried and then Ag- TiO_2 /(500°C) was obtained.

2.5. Characterization of Electrocatalytic Properties of Ag- TiO_2 Nanotube Electrode. The electrochemical measurements were carried out with a conventional three-electrode system. The prepared electrode (TiO_2 , Ag- TiO_2 and Ag- TiO_2 /(500°C)) was used as a working electrode with a platinum electrode as an auxiliary electrode and a saturated calomel electrode (SCE) as a reference electrode in all cases.

3. Results and Discussions

3.1. Morphology, Composition, and Structure Analysis. The morphologies of the as-formed TiO_2 nanotubes, Ag-fresh TiO_2 , and Ag- TiO_2 /(500°C) were depicted in Figure 1. Figure 1(a) showed clearly the prepared vertically aligned TiO_2 nanotubes arrays with diameter of 120 nm and length of 1.2 μm . It is apparent from Figure 1(b) that the ordered and evenly distributed Ag nanoparticles with average diameter of 20 nm are formed preferentially on the exterior mouth of the amorphous TiO_2 nanotubes. After the nanotubes were annealed at 500°C, the Ag nanoparticles were deposited on them under the same method (see Figure 1(c)). Some Ag nanoparticles were dispersed on the pore openings and showed a distribution that is more dense than that in Figure 1(b), while some were deposited into the nanotubes, as indicated by the arrow. It can be presumed that the nanotubes annealed at 500°C facilitate the Ag formation on the tube surface, and the electrocatalytic properties were also improved as discussed later.

3.2. Nanoindentation Properties. In recent years nanoindentation technology has been widely used to measure the hardness and elasticity modulus of medical materials, especially in implants devices [25]. The description of the samples' (TiO_2 , Ag-fresh TiO_2 and Ag- TiO_2 /(500°C) nanotube) nanomechanical characterization was provided. As observed in Figure 2, the displacement of Ag- TiO_2 /(500°C) nanotubes was the shortest and TiO_2 nanotubes were the longest when load was selected the same. It was easy to figure out Ag- TiO_2 /(500°C) nanotubes were the hardest and the reason could be ascribed to two aspects. Compared with nonannealed sample, the higher hardness observed for Ag- TiO_2 /(500°C) nanotubes can be due to the higher hardness of anatase and rutile phases for annealed samples at 500°C. The hardness results obtained for nonannealed sample and annealed sample were similar to those stated in earlier studies [26]. In addition, it may be ascribed to the deposition of Ag nanoparticles. Both inside and outside of nanotubes were attached with Ag-NPs which densified empty space, resulting in fixed enhancement of hardness.

3.3. Electrocatalytic Oxidation of Glucose on the Prepared Electrodes. CVs were used to investigate the catalytic activities of the Ag- TiO_2 /(500°C) electrode. Figure 3 showed CVs of

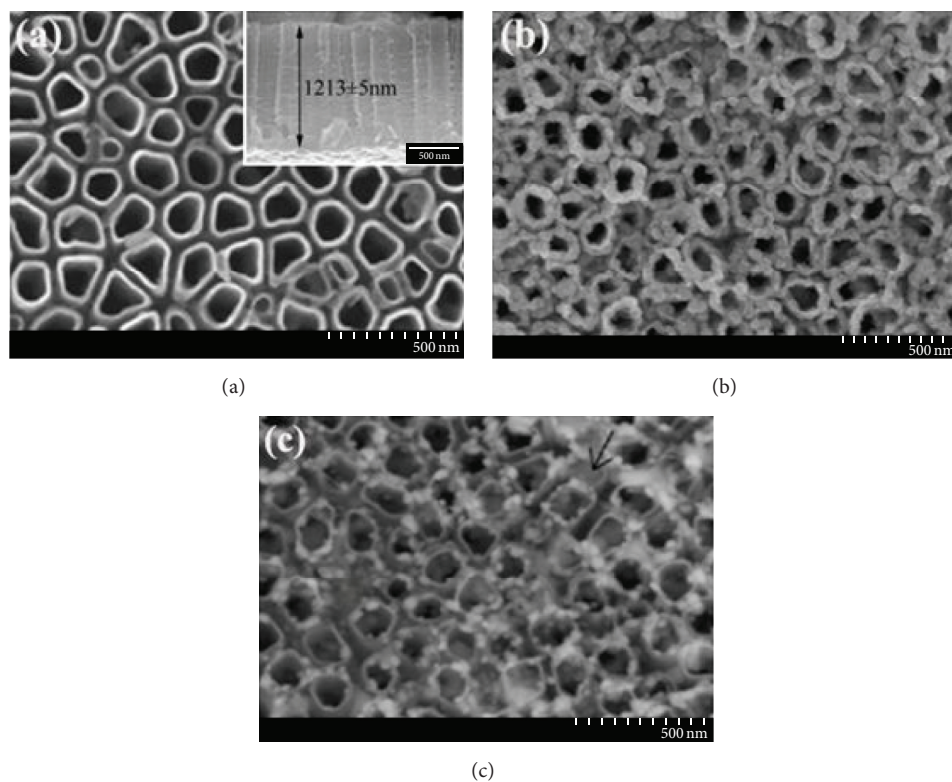


FIGURE 1: SEM images of TiO₂ (a), Ag-TiO₂(b), and Ag-TiO₂(500°C) (c) nanotube. Inset: the sectional view of TiO₂.

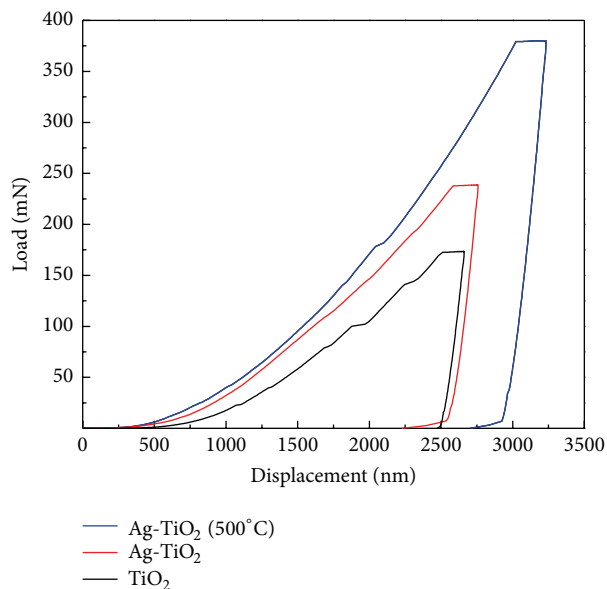


FIGURE 2: Characteristic load versus nanoindentation depth for TiO₂, Ag-TiO₂, and Ag-TiO₂(500°C) nanotube.

the as-formed TiO₂ nanotube, Ag-fresh TiO₂ nanotube, and Ag-TiO₂/(500°C) nanotube electrode in the presence and absence of 0.5 M glucose supported by 0.1 M neutral PBS, respectively. Almost no current increase of TiO₂ and Ag-TiO₂ nanotubes with glucose addition from Figures 3(a) and 3(b)

was observed, which demonstrated that the TiO₂ nanotubes and Ag-TiO₂ nanotubes electrode exhibited no electrocatalytic oxidation activity to glucose while Ag-TiO₂/(500°C) electrode displayed a pair of redox peaks with the anodic and cathodic peak potential positioned at +0.03 V and -0.3 V from Figure 3(c), which can be ascribed to the oxidation of glucose, indicating that the Ag-TiO₂/(500°C) electrode possessed strong catalytic activity towards glucose. There were two possible explanations for this result. The first possibility was relatively weak adherence of Ag nanoparticles onto the nonannealed nanotubular surfaces. The other possibility was that a small amount of silver titanates were obtained by depositing Ag nanoparticles on the TiO₂/500°C nanotubes, which indicated that the Ag can not only be deposited but also be doped in the TiO₂ nanotubes. The crystal structure distortion increased state density of Ag-TiO₂/500°C coating, facilitating the migration of charge carriers, and enhanced catalytic activity [19].

Figure 4 showed CVs of Ag-TiO₂/(500°C) nanotube electrode in 0.5 M glucose supported by 0.1 M neutral PBS, 0.1 M H₂SO₄, and 0.1 M NaOH. As observed in Figure 4, compared with CVs in 0.1 M H₂SO₄ and 0.1 M NaOH, CVs of Ag-TiO₂/(500°C) nanotube electrode in PBS exhibited two oxidation peaks related to the oxidation of glucose, which indicated excellent electrochemical behavior.

Figure 5 showed CVs of the Ag-TiO₂/(500°C) nanotube electrode in blank solution and 0.5 M glucose with the presence of 0.12 M NaCl and without the presence of 0.12 M NaCl supported by 0.1 M neutral PBS. Cl ion was the

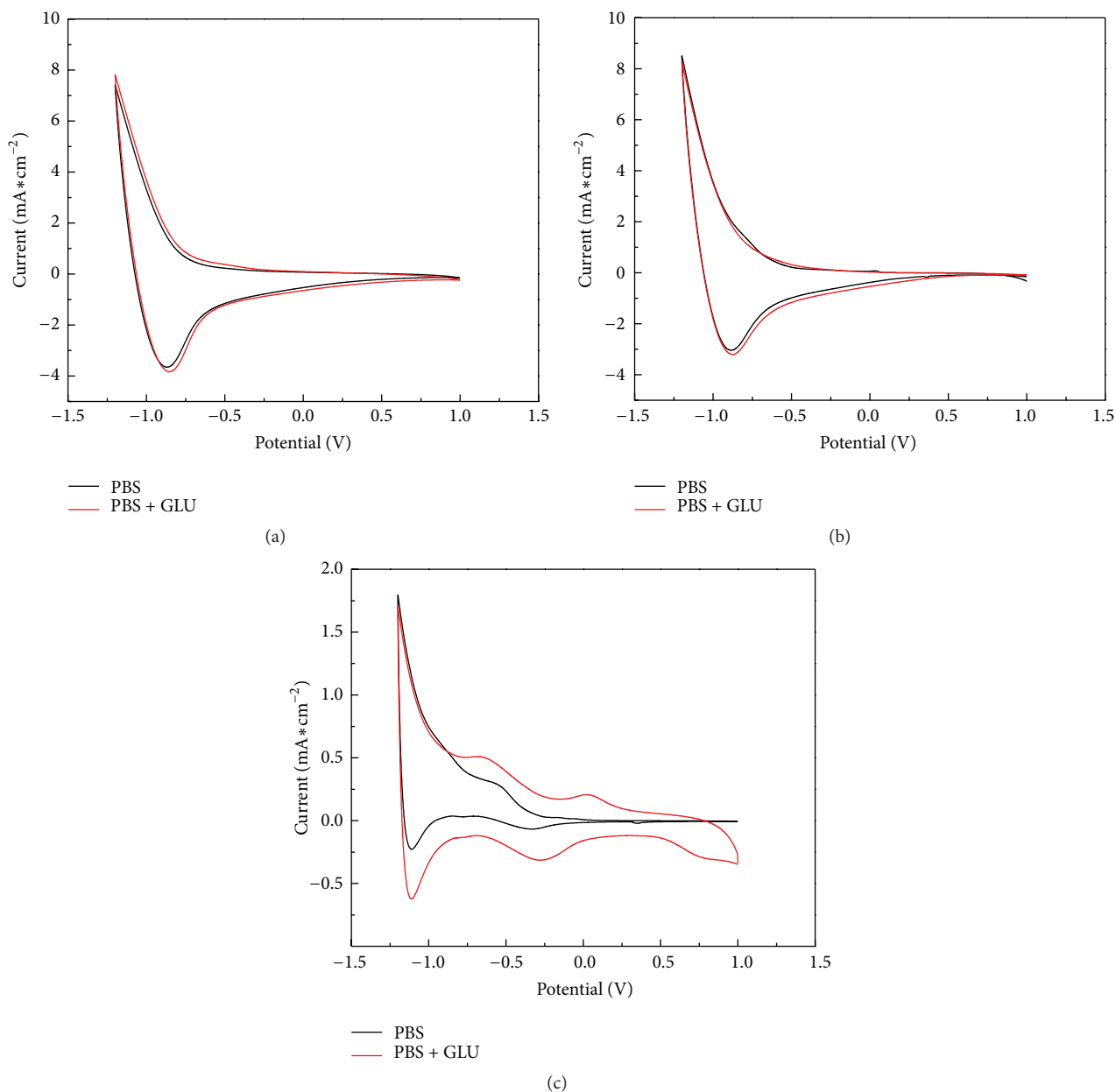


FIGURE 3: CVs of TiO_2 (a), Ag-TiO_2 (b), and $\text{Ag-TiO}_2(500^\circ\text{C})$ (c) electrode in 0.1 M neutral PBS with (red line) or without (black line) 0.2 M glucose.

usual interfering ion which was preferentially adsorbed on the surface of electrodes, resulting in toxicosis and losing electrocatalytic property. As observed in Figure 5, in the blank PBS solution, CVs were characterized by hydrogen adsorption/desorption peaks at negative potentials and a flat double layer region at positive potentials. After 0.5 M glucose was added, an obvious redox peak appeared from -0.3 V to $+0.03\text{ V}$, proving excellent electrocatalytic oxidation ability, whereas in the presence of chloride ions, when Cl ions were dropped into the solution, the redox peak vanished and the oxidation of glucose was suppressed, which could be attributed to the adsorbing of Cl^- preferentially compared with glucose.

According to the adsorption theory proposed by Wang et al. [27], it could be deduced that when there were no Cl ions in the solution, glucose molecules would adsorb on the surface of $\text{Ag-TiO}_2(500^\circ\text{C})$ nanotube electrode in the first place, forming glucose intermediates. During the potential scanned from -0.3 V to $+0.03\text{ V}$ gradually, the intermediates were oxidized leading to current increasing. When potential was over $+0.03\text{ V}$, the oxidized intermediates were adsorbed on the surface, covering the active sites of electrode and decreasing current. When large amounts of chloride ions were present, the poisoning $\text{Ag-TiO}_2(500^\circ\text{C})$ nanotube electrode showed no electrocatalytic properties.

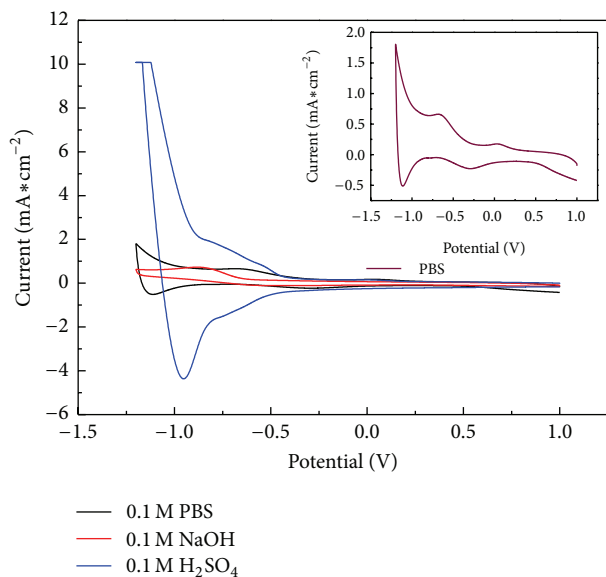


FIGURE 4: CVs of Ag-TiO₂(500°C) nanotube electrode in 0.5 M glucose supported by 0.1 M neutral PBS, 0.1 M H₂SO₄, and 0.1 M NaOH.

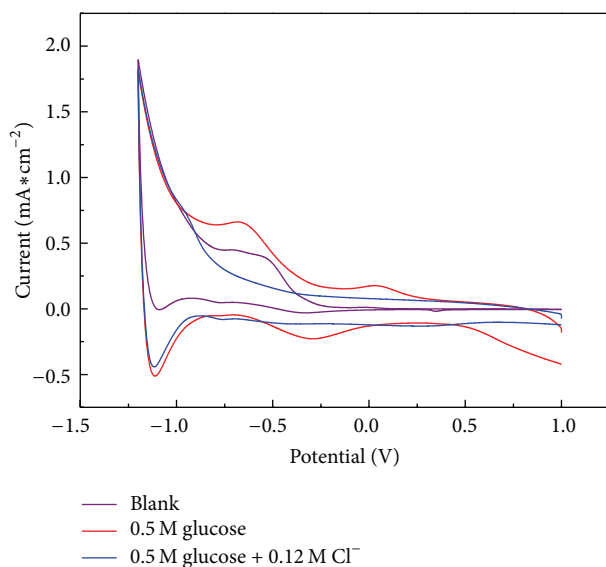


FIGURE 5: CVs of Ag-TiO₂(500°C) nanotube electrode in blank solution, 0.5 M glucose with the presence of 0.12 M NaCl and 0.5 M glucose without the presence of 0.12 M NaCl supported by 0.1 M neutral PBS.

3.4. Amperometric Performance of Ag-TiO₂(500°C) Nanotube Electrode to Glucose Oxidation. Differential pulse voltammetry (DPV) was used to determine the sensor outputs at different glucose concentrations. Figure 6 presented the relationship between currents and variation concentrations of glucose. The prepared electrode exhibited linearity for glucose sensing that ranged from 20 mM to 190 mM with a correlation coefficient of 0.9993. The electrode sensitivity calculated from the slope of the calibration curve was 3.69 mA * cm⁻² * mM⁻¹ with the detection limit of 24 μM.

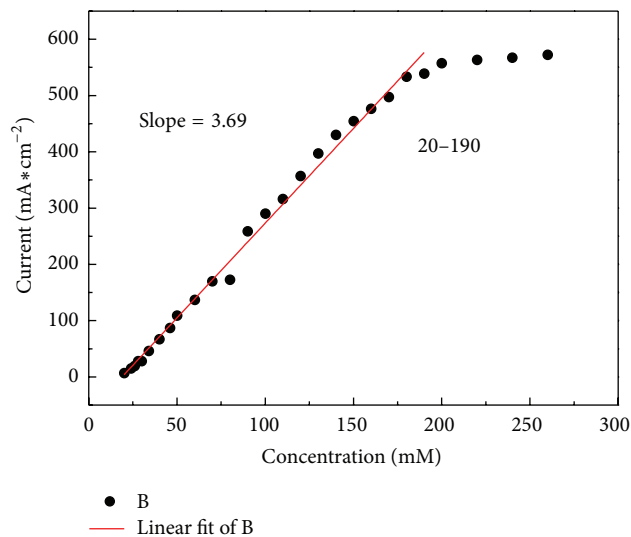


FIGURE 6: Calibration curve for the amperometric responses of the Ag-TiO₂(500°C) nanotube electrode to glucose.

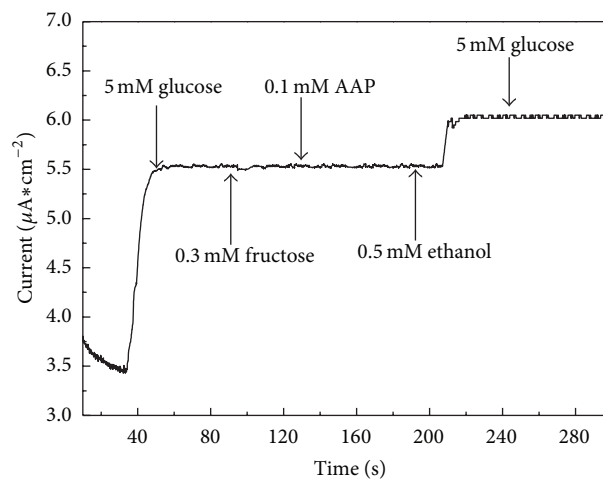


FIGURE 7: The influence of electroactive compounds (ethanol, fructose, and AAP) on the response of 5.0 mM glucose.

Ascorbic acid (AA), uric acid (UA), sucrose, fructose, dopamine, ethanol, and acetaminophen (AAP) were the commonly interfering biomolecules which coexist with glucose in the human blood. To evaluate the selectivity of the Ag-TiO₂(500°C) nanotube electrode, the current responses to ethanol, fructose, and AAP were examined. As shown in Figure 7, it was observed that the response signals of ethanol, fructose, and AAP were negligible for glucose determination. The good selectivity of the nonenzymatic sensor was related to the proper working potential used.

The reproducibility and stability of response current of the Ag-TiO₂(500°C) nanotube electrode were studied. The amperometric response of 10 different Ag-TiO₂(500°C) nanotube electrodes to 1.0 mM glucose was tested independently. As shown in Figure 8, the relative standard deviation (RSD) was 1.5% for 10 successive measurements, revealing that the

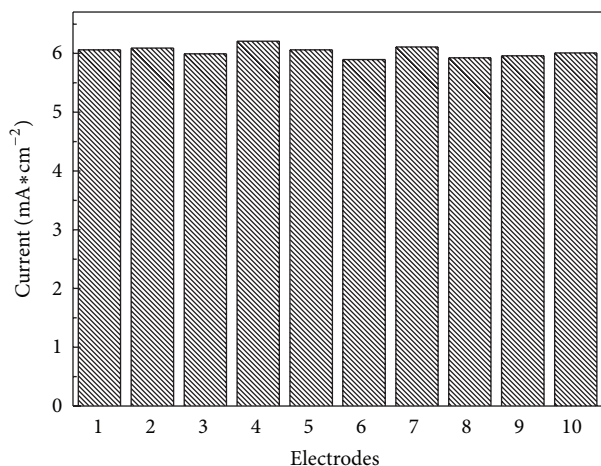


FIGURE 8: Current response of 10 different Ag-TiO₂(500°C) nanotube electrodes to 1.0 mM glucose in PBS (7.0).

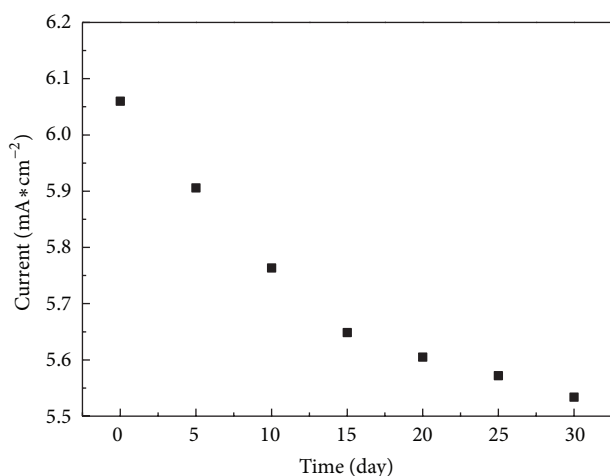


FIGURE 9: Current response of the Ag-TiO₂(500°C) nanotube electrode to 10 mM glucose after storing for different days.

preparation method was acceptably reproducible. The long-term stability was explored by measuring a glucose solution, and the electrode was stored at room temperature. Figure 9 showed that the response current maintained about 92% of the initial value after 30 days, demonstrating the good stability of the Ag-TiO₂(500°C) nanotube electrode based nonenzymatic glucose biosensor.

4. Conclusions

In this work, a simple and effective way to prepare Ag nanoparticles deposited on the surface of TiO₂ nanotube was developed. The Ag deposited and annealing processes made TiO₂ nanotube harder which was conducive to the application of tough condition. The electrochemical results demonstrated that the prepared Ag-TiO₂(500°C) nanotube electrode possessed excellent electrocatalytic performance. The constructed nonenzymatic glucose biosensor exhibited good selectivity, stability, and reproducibility. Because of the

simple preparation method and good catalytic performance, such material has potential application in catalysis and sensor areas.

Competing Interests

The authors declare that they have no competing interests.

Acknowledgments

The authors gratefully acknowledge the financial support from the Natural Science Foundation of China (Grant nos. 51301117 and 31271005) and the Natural Science Foundation for Young Scientists of Shanxi Province, China (Grant nos. 2013021003-1 and 2013021013-5).

References

- [1] Y. Ding, Y. Wang, L. Su, H. Zhang, and Y. Lei, "Preparation and characterization of NiO-Ag nanofibers, NiO nanofibers, and porous Ag: towards the development of a highly sensitive and selective non-enzymatic glucose sensor," *Journal of Materials Chemistry*, vol. 20, no. 44, pp. 9918–9926, 2010.
- [2] V. Poitout, D. Moatti-Sirat, G. Reach et al., "A glucose monitoring system for on line estimation in man of blood glucose concentration using a miniaturized glucose sensor implanted in the subcutaneous tissue and a wearable control unit," *Diabetologia*, vol. 36, no. 7, pp. 658–663, 1993.
- [3] X. Cao, N. Wang, S. Jia, and Y. Shao, "Detection of glucose based on bimetallic PtCu nanochains modified electrodes," *Analytical Chemistry*, vol. 85, no. 10, pp. 5040–5046, 2013.
- [4] E. Reitz, W. Jia, M. Gentile, Y. Wang, and Y. Lei, "CuO nanospheres based nonenzymatic glucose sensor," *Electroanalysis*, vol. 20, no. 22, pp. 2482–2486, 2008.
- [5] L. C. Clark Jr. and J. C. Lyons, "Electrode systems for continuous monitoring in cardiovascular surgery," *Annals of the New York Academy of Sciences*, vol. 102, pp. 29–45, 1962.
- [6] A. Riklin, E. Katz, I. Willner, A. Stocker, and A. F. Buckmann, "Improving enzyme-electrode contacts by redox modification of cofactors," *Nature*, vol. 376, no. 6542, pp. 672–675, 1995.
- [7] Y. B. Vassilyev, O. A. Khazova, and N. N. Nikolaeva, "Kinetics and mechanism of glucose electrooxidation on different electrode-catalysts. Part I. Adsorption and oxidation on platinum," *Journal of Electroanalytical Chemistry*, vol. 196, no. 1, pp. 105–125, 1985.
- [8] B. Beden, F. Largeaud, K. B. Kokoh, and C. Lamy, "Fourier transform infrared reflectance spectroscopic investigation of the electrocatalytic oxidation of D-glucose: identification of reactive intermediates and reaction products," *Electrochimica Acta*, vol. 41, no. 5, pp. 701–709, 1996.
- [9] L. M. Lu, L. Zhang, F. L. Qu et al., "A nano-Ni based ultrasensitive nonenzymatic electrochemical sensor for glucose: enhancing sensitivity through a nanowire array strategy," *Biosensors and Bioelectronics*, vol. 25, no. 1, pp. 218–223, 2009.
- [10] L. Meng, J. Jin, G. X. Yang, T. H. Lu, H. Zhang, and C. X. Cai, "Nonenzymatic electrochemical detection of glucose based on palladium-single-walled carbon nanotube hybrid nanostructures," *Analytical Chemistry*, vol. 81, no. 17, pp. 7271–7280, 2009.
- [11] F. Xiao, F. Q. Zhao, D. P. Mei, Z. R. Mo, and B. Z. Zeng, "Nonenzymatic glucose sensor based on ultrasonic-electrodeposition

- of bimetallic PtM (M = Ru, Pd and Au) nanoparticles on carbon nanotubes-ionic liquid composite film,” *Biosensors and Bioelectronics*, vol. 24, no. 12, pp. 3481–3486, 2009.
- [12] J.-S. Ye, Y. Wen, W. D. Zhang, L. M. Gan, G. Q. Xu, and F.-S. Sheu, “Nonenzymatic glucose detection using multi-walled carbon nanotube electrodes,” *Electrochemistry Communications*, vol. 6, no. 1, pp. 66–70, 2004.
- [13] C. Y. Guo, H. H. Huo, X. Han, C. L. Xu, and H. L. Li, “Ni/CdS bifunctional Ti@TiO₂ core-shell nanowire electrode for high-performance nonenzymatic glucose sensing,” *Analytical Chemistry*, vol. 86, no. 1, pp. 876–883, 2014.
- [14] H.-K. Seo, D.-J. Park, and J.-Y. Park, “Fabrication and characterization of platinum black and mesoporous platinum electrodes for in-vivo and continuously monitoring electrochemical sensor applications,” *Thin Solid Films*, vol. 516, no. 16, pp. 5227–5230, 2008.
- [15] D. Rathod, C. Dickinson, D. Egan, and E. Dempsey, “Platinum nanoparticle decoration of carbon materials with applications in non-enzymatic glucose sensing,” *Sensors and Actuators, B: Chemical*, vol. 143, no. 2, pp. 547–554, 2010.
- [16] J. H. Zhu, J. Jiang, J. P. Liu et al., “CNT-network modified Ni nanostructured arrays for high performance non-enzymatic glucose sensors,” *RSC Advances*, vol. 1, no. 6, pp. 1020–1025, 2011.
- [17] A. Baciú, A. Pop, A. Remes, F. Manea, and G. Burtica, “Nonenzymatic electrochemical determination of glucose on silver-doped zeolite-CNT composite electrode,” *Advanced Science, Engineering and Medicine*, vol. 3, no. 1-2, pp. 13–19, 2011.
- [18] L.-M. Lu, X.-B. Zhang, G.-L. Shen, and R.-Q. Yu, “Seed-mediated synthesis of copper nanoparticles on carbon nanotubes and their application in nonenzymatic glucose biosensors,” *Analytica Chimica Acta*, vol. 715, pp. 99–104, 2012.
- [19] Y. Q. Liang, Z. D. Cui, S. L. Zhu, Y. Liu, and X. J. Yang, “Silver nanoparticles supported on TiO₂ nanotubes as active catalysts for ethanol oxidation,” *Journal of Catalysis*, vol. 278, no. 2, pp. 276–287, 2011.
- [20] Y. Q. Liang, Z. D. Cui, S. L. Zhu, and X. J. Yang, “Formation and characterization of iron oxide nanoparticles loaded on self-organized TiO₂ nanotubes,” *Electrochimica Acta*, vol. 55, no. 18, pp. 5245–5252, 2010.
- [21] J. Joo, S. G. Kwon, T. Yu et al., “Large-scale synthesis of TiO₂ nanorods via nonhydrolytic sol-gel ester elimination reaction and their application to photocatalytic inactivation of *E. coli*,” *Journal of Physical Chemistry B*, vol. 109, no. 32, pp. 15297–15302, 2005.
- [22] S. Yoo, S. A. Akbar, and K. H. Sandhage, “Nanocarving of bulk titania crystals into oriented arrays of single-crystal nanofibers via reaction with hydrogen-bearing gas,” *Advanced Materials*, vol. 16, no. 3, pp. 260–264, 2004.
- [23] Y. Yu, L.-L. Ma, W.-Y. Huang, J.-L. Li, P.-K. Wong, and J. C. Yu, “Coating MWNTs with Cu₂O of different morphology by a polyol process,” *Journal of Solid State Chemistry*, vol. 178, no. 5, pp. 1488–1494, 2005.
- [24] P. V. Suneesh, V. S. Vargis, T. Ramachandran, B. G. Nair, and T. G. Sathesh Babu, “Co–Cu alloy nanoparticles decorated TiO₂ nanotube arrays for highly sensitive and selective nonenzymatic sensing of glucose,” *Sensors and Actuators B: Chemical*, vol. 215, pp. 337–344, 2015.
- [25] S. A. Catledge, J. Borham, Y. K. Vohra, W. R. Laceyfield, and J. E. Lemons, “Nanoindentation hardness and adhesion investigations of vapor deposited nanostructured diamond films,” *Journal of Applied Physics*, vol. 91, no. 8, pp. 5347–5352, 2002.
- [26] E. Zalnezhad, A. M. S. Hamouda, G. Faraji, and S. Shamshirband, “TiO₂ nanotube coating on stainless steel 304 for biomedical applications,” *Ceramics International*, vol. 41, no. 2, pp. 2785–2793, 2015.
- [27] J. P. Wang, D. F. Thomas, and A. C. Chen, “Nonenzymatic electrochemical glucose sensor based on nanoporous PtPb networks,” *Analytical Chemistry*, vol. 80, no. 4, pp. 997–1004, 2008.

Research Article

Hydrothermal Synthesis and Responsive Characteristics of Hierarchical Zinc Oxide Nanoflowers to Sulfur Dioxide

Qu Zhou,¹ Bo Xie,² Lingfeng Jin,² Weigen Chen,² and Jian Li²

¹College of Engineering and Technology, Southwest University, Chongqing 400715, China

²State Key Laboratory of Power Transmission Equipment & System Security and New Technology, Chongqing University, Chongqing 400030, China

Correspondence should be addressed to Qu Zhou; zhouqu@swu.edu.cn

Received 4 December 2015; Revised 19 February 2016; Accepted 21 February 2016

Academic Editor: Thomas Thundat

Copyright © 2016 Qu Zhou et al. This is an open access article distributed under the Creative Commons Attribution License, which permits unrestricted use, distribution, and reproduction in any medium, provided the original work is properly cited.

Sulfur dioxide, SO₂, is one of the most important decomposition byproducts of sulfur hexafluoride, SF₆, under partial discharge in GIS apparatus. The sensing performances of semiconductor gas sensors can be improved by morphology tailoring. This paper reported the synthesis method, structural characterization, and SO₂ responsive characteristics of hierarchical flower-shaped ZnO nanostructures. Hierarchical ZnO nanoflowers were successfully prepared via a facile and simple hydrothermal method and characterized by X-ray powder diffraction, scanning electron microscopy, energy dispersive X-ray spectroscopy, and X-ray photoelectron spectroscopy, respectively. Planar chemical gas sensor was fabricated and its responsive characteristics towards SO₂ were systematically performed. The optimum operating temperature of the fabricated sensor was measured to be about 260°C, and the corresponding maximum responses were 16.72 and 26.14 to 30 and 60 ppm of SO₂. Its saturated gas concentration was 2000 ppm with a response value of 67.41. Moreover, a quick response and recovery feature (7 s and 8 s versus 80 ppm of SO₂) and good stability were also observed. All results indicate that the proposed sensor is a promising candidate for detecting SF₆ decomposition byproduct SO₂.

1. Introduction

Sulfur hexafluoride, SF₆, is a typical kind of colorless, tasteless, nontoxic, and nonflammable inert gas under general conditions with an extreme high thermal decomposition temperature [1, 2]. With the prominent advantages of small floor space, high reliability and stability, excellent insulation strength, non-smearly oil, and lower maintenance cost, gas insulated switchgear (GIS) apparatus filled with pressurized SF₆ gas are widely used in electrical power system in recent decades. Inevitable defects existed during the design, manufacture, transportation, installation, and operation processes of a GIS system [3]. These internal insulation defects, like metal burrs or suspended particles, may cause insulation degradation and even partial discharge in the long-term service cycle. If partial discharge occurs in GIS, SF₆ gas molecules firstly decompose into some low-fluorine sulfides and then react with trace oxygen and water vapor to generate various kinds of decomposition byproducts, for instance,

SO₂, SOF₂, SO₂F₂, SOF₄, H₂S, and HF [4, 5]. These decomposition byproducts would speed up the aging of insulation material and the corrosion of metal, eventually resulting in faults that happened in GIS.

Recent researches at home and abroad demonstrated that the composition and concentration of SF₆ decomposition byproducts are closely related to the insulation status of GIS. Monitoring and analyzing the component contents of these characteristic decomposition products and their generation rates are one of the most effective and convenient methods for GIS condition assessment and fault diagnosis [3, 5]. Till now, the main sensing approaches employed for recognizing SF₆ decomposition byproducts are gas chromatography [1, 2], infrared absorption spectrometry [6, 7], and metal oxide semiconductor [8, 9]. Gas chromatography is mainly used for offline testing in laboratory and cross sensitivity between SF₆ and its decomposition byproducts exists for infrared absorption spectrometry [10, 11]. With the advantages of simple fabrication, low cost, high response, rapid response

and recovery time, and facile integration, metal oxide semiconductor like n-type ZnO [12–14] or n-type SnO₂ [15–18] may represent the most promising sensing technology for sensing SF₆ decomposition byproducts. However, due to the deficiencies of low gas response and high working temperature, the application of using metal oxide semiconductor based sensors detecting SF₆ decomposition byproducts is greatly limited [8, 10].

Hence, in this study, we prepare hierarchical ZnO nanoflowers through a simple hydrothermal process and report systematically their responsive characteristics to SO₂, one of the most important decomposition byproducts of SF₆ under partial discharge in GIS apparatus.

2. Experimental Details

All chemicals were analytical grade reagents purchased from Chongqing Chuandong Chemical Reagent Co. Ltd. and used as received without any further purification. Hierarchical flower-shaped ZnO nanostructures were synthesized with a simple, facile, and environment-friendly hydrothermal method. The detailed synthesis processes were represented as follows.

Typically, 2.0 mmol zinc nitrate hexahydrate, Zn(NO₃)₂·6H₂O, 4.0 mmol NH₄OH, 28 wt% NH₃ in H₂O, 0.83 g CTAB, 30 mL absolute ethanol, and 30 mL distilled water were mixed together with intense magnetic stirring, which were subsequently transferred into a Teflon autoclave, sealed, and heated at 160°C for 24 h in an electric furnace. After reaction, the autoclave was cooled to room temperature naturally, harvested by centrifugation, washed with distilled water and absolute ethanol several times to remove the ions possibly remaining in the final product, and finally dried at 80°C in air for further use.

The crystalline structures of the as-prepared ZnO samples were performed by X-ray powder diffraction (XRD, Rigaku D/Max-1200X, Japan) with Cu K α radiation operated at 40 kV and 200 mA and a scanning rate of 0.02° s⁻¹ from 20° to 80° [12]. Surface morphologies and microstructures of the as-prepared nanostructures were observed with a Nova 400 Nano field emission scanning electron microscope (FESEM, FEI, Hillsboro, OR, USA) equipped with an energy dispersive X-ray spectroscopy (EDS) [15]. X-ray photoelectron spectroscopy (XPS) was performed on an ESCALAB MKII using monochromatic Al K α as the X-ray exciting source to investigate the chemical state of elements existing in the samples.

Planar chemical gas sensors based on the as-prepared powders were fabricated with screen-printing technique, and the planar ceramic substrates were purchased from Beijing Elite Tech Co., Ltd., China [12]. Firstly, the as-prepared nanostructures were mixed with deionized water and absolute ethanol in a weight ratio of 10:2:1 to form a suspension. Then it was subsequently screen-printed onto the planar ceramic substrate to form a sensing film with a thickness of about 50 μ m. Finally, the fabricated sensor was dried in air at 100°C to volatilize the organic solvent and further aged in an aging test chamber for 36 h. Responsive characteristics of the fabricated sensors to SO₂ were measured

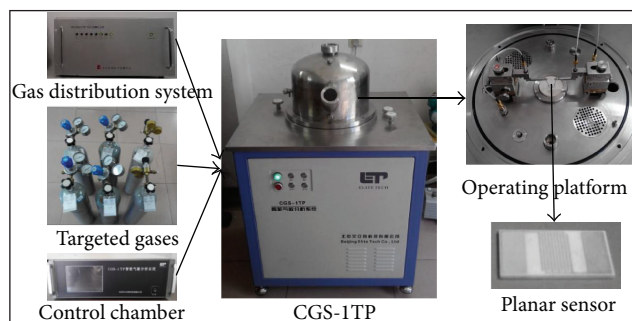


FIGURE 1: Schematic diagram of the CGS-ITP gas sensing analysis system.

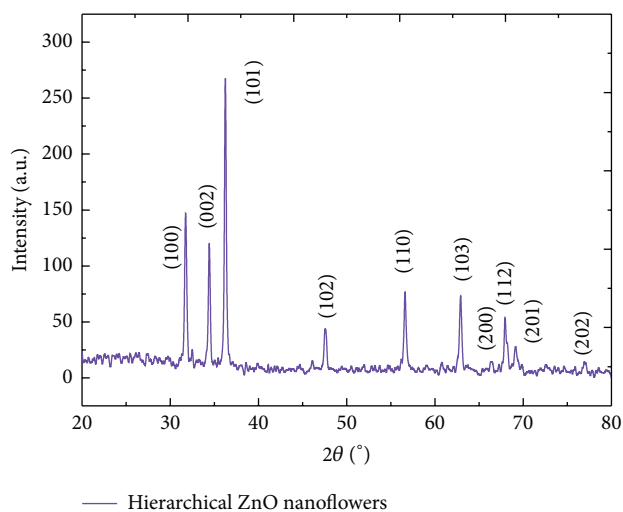


FIGURE 2: Typical XRD patterns of the synthesized hierarchical ZnO nanoflowers.

and automatically recorded by a CGS-ITP intelligent gas sensing analysis system, purchased from Beijing Elite Tech Co., Ltd., China. Figure 1 shows the schematic diagram of the CGS-ITP gas sensing analysis system [15].

In this study, gas response of the sensor to SF₆ partial discharge decomposition byproduct SO₂ was defined as $S = R_a/R_g$ [19, 20], where R_a denotes the resistance value of the sensor in pure N₂ and R_g in certain concentration of target gas mixed with pure N₂. The response and recovery time were defined as the time required by the sensor to achieve 90% of the total resistance change in the case of gas adsorption or gas desorption [21, 22]. All measurements were repeated several times to ensure the repeatability of the sensor.

3. Results and Discussion

The crystalline phases and structures of the as-prepared hierarchical ZnO nanostructures after annealing at 600°C for 5 h were characterized by the X-ray powder diffraction measurement and shown in Figure 2. One can clearly see from this figure that all the peaks are corresponding to wurtzite hexagonal ZnO structure given in the standard data file of JCPDS. 36-1451 [23]. The prominent peaks at 31.7°,

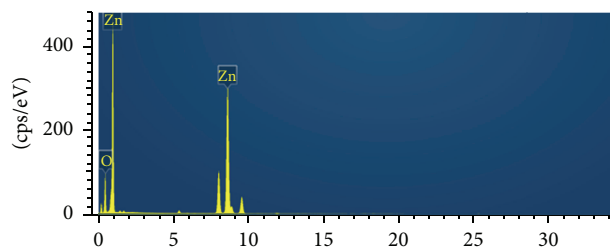


FIGURE 3: EDS spectrum of the synthesized hierarchical ZnO nanoflowers.

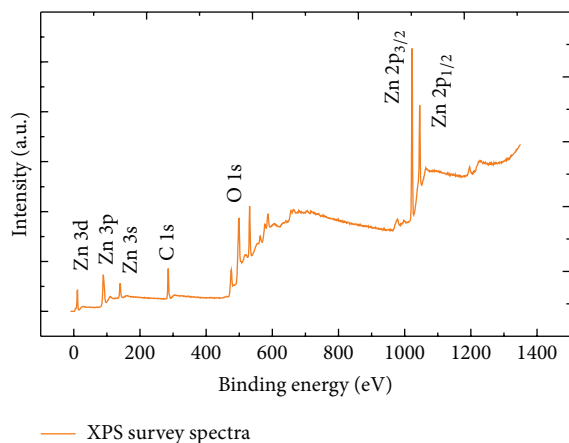


FIGURE 4: XPS survey spectra of the synthesized hierarchical ZnO nanoflowers.

34.4° , and 36.2° can be well indexed as the (100), (002), and (101) planes of wurtzite hexagonal ZnO, respectively [24, 25]. No other diffraction peaks from any impurities are detected, indicating a high purity of the as-prepared samples.

Energy dispersive X-ray spectroscopy measurement was further performed to investigate the element components of the as-synthesized samples. Figure 3 demonstrates the EDS spectrum of the synthesized ZnO nanostructures. As shown in Figure 3, only Zn and O element peaks were observed, which confirms the availability of Zn and O in the synthesized samples [25–27].

To further investigate the composition and the chemical state of the elements existing in the synthesized ZnO nanostructures, X-ray photoelectron spectroscopy XPS measurement was performed and collected. Adventitious hydrocarbon C 1s binding energy at 285 eV was used as a reference to correct the energy shift of O 1s. The XPS wide survey spectrum of the synthesized hierarchical samples as shown in Figure 4 confirms the existence of Zn, O, and C. The binding energies at 1022.3 eV and 1044.9 eV could be well identified as Zn 2p_{3/2} and Zn 2p_{1/2}, which could be attributed to Zn²⁺ ions [25–27]. Thus, based on these XRD, EDS, and XPS results, we can draw a conclusion that pure ZnO nanostructures have been successfully synthesized with the current route [23].

The surface structures and morphologies of the as-synthesized ZnO nanostructures were performed by FESEM. As illustrated in Figure 5 the panoramic image of the as-prepared hierarchical ZnO nanostructures is in flower shape,

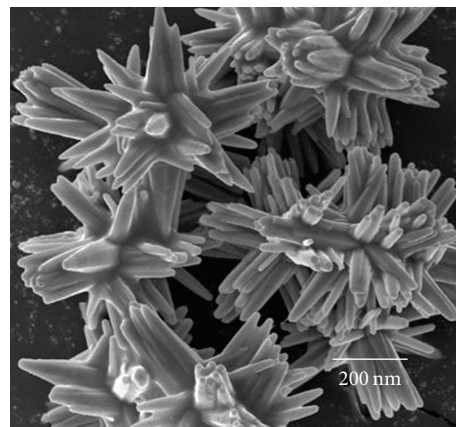


FIGURE 5: FESEM image of the synthesized hierarchical ZnO nanoflowers.

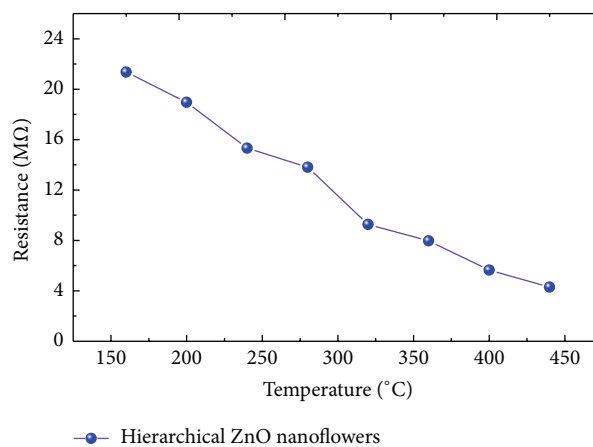


FIGURE 6: Resistance of the hierarchical ZnO nanoflowers sensor versus operating temperature.

which consisted of a large number of nanorods. These nanorods are rectangular with high uniformity in shape and size. No other morphologies have been detected, suggesting a high yield of the flower-like ZnO nanostructures.

Figure 6 shows the electrical resistance curve of the sensor fabricated from the as-prepared hierarchical ZnO nanoflowers versus various operating temperatures from 160 to 440°C in pure N₂. As shown in Figure 6, the resistance value of the sensor decreases with increasing temperature in the whole temperature range, which is an intrinsic characteristic of an n-type semiconductor gas sensor.

Figure 7 illustrates the gas responses of the fabricated sensors to 30 ppm and 60 ppm of SO₂ at various working temperatures. As shown in Figure 7, each response curve of the sensor increases rapidly and achieves the maximum value and then decreases quickly with further increasing temperature. The optimum operating temperature of the fabricated hierarchical ZnO nanoflowers sensor to SO₂ gas was measured at 260°C, where the sensor exhibits the maximum gas response. And the corresponding maximum response value is 16.72 and 26.14, respectively.

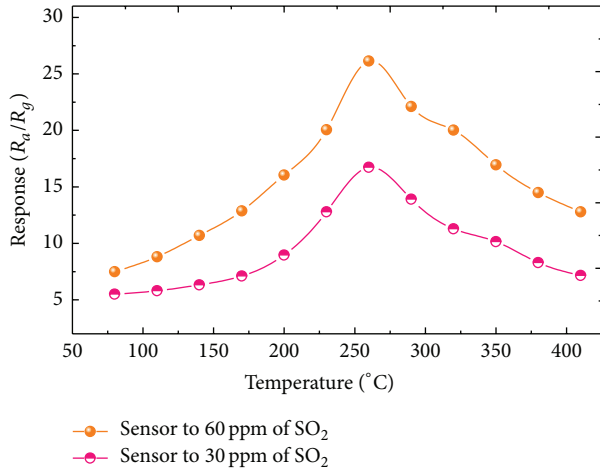


FIGURE 7: Gas response of the hierarchical ZnO nanoflowers sensor to 30 and 60 ppm of SO_2 at various working temperatures.

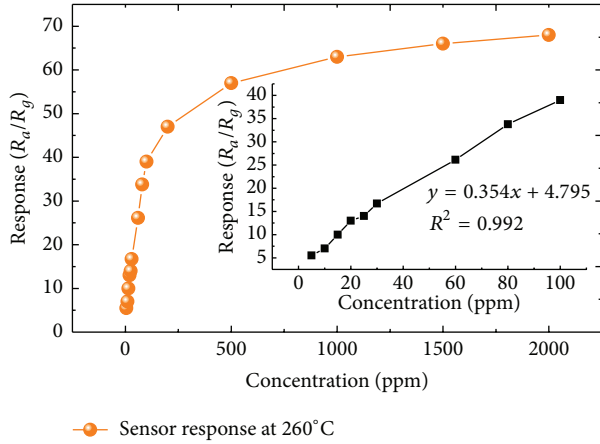


FIGURE 8: Gas response of the hierarchical ZnO nanoflowers sensor to various concentrations of SO_2 at 260°C .

Figure 8 shows the gas response of the sensor as a function of SO_2 gas concentration in the range of 5–2000 ppm, where the sensor worked at its own optimum operating temperature mentioned above. As represented, the sensing responses of the sensor versus SO_2 gas increase greatly with increasing gas concentration in the range of 5–100 ppm and achieve saturation when exposed to more than 2000 ppm. The saturated gas sensing response value of the sensor to SO_2 gas was measured to be about 67.41.

Figure 9 gives the dynamic response and recovery curve of the sensor versus 80 ppm SO_2 to investigate its response-recovery feature. As seen in Figure 9, when certain concentration of SO_2 gas was injected into the test chamber, gas response of the sensor increases rapidly and dramatically decreases when the sensor was exposed for recovering, which is an intrinsic characteristic for n-type semiconductor material. Meanwhile, the sensor response returns to its initial value after testing, implying a satisfying stability of the prepared sensor. According to the definition above, the response and

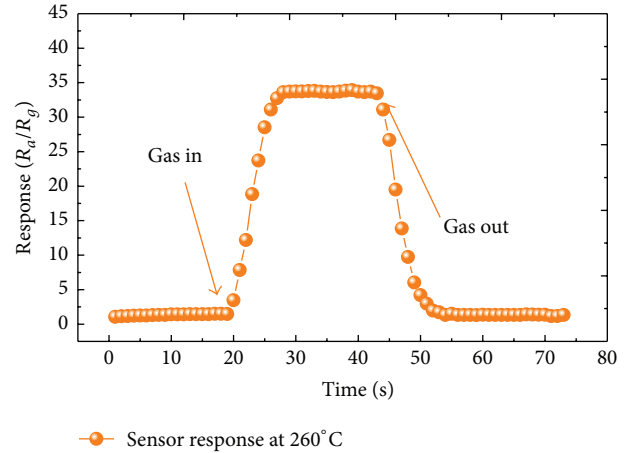


FIGURE 9: Dynamic sensing transient of the hierarchical ZnO nanoflowers sensor to 80 ppm of SO_2 at 260°C .

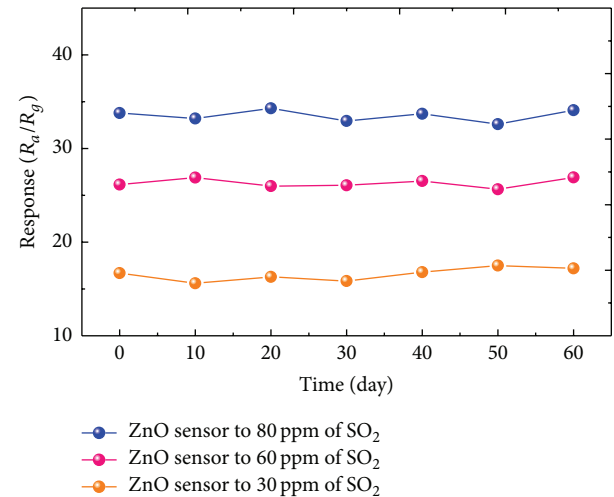


FIGURE 10: Stability of the hierarchical ZnO nanoflowers sensor to 30, 60, and 80 ppm of SO_2 at 260°C .

recovery times of the sensor are calculated to be about 7 s and 8 s, respectively.

Finally, the long-term stability of the fabricated hierarchical ZnO nanoflowers sensor to 30, 60, and 80 ppm of SO_2 at 260°C was measured and displayed in Figure 10. As seen from the stability plot, the gas response of sensor changes slightly and keeps at a nearly constant value during the long experimental cycles, confirming an excellent longtime stability and repeatability of the sensor for SO_2 detection.

4. Conclusions

In summary, hierarchical ZnO nanoflowers were synthesized via hydrothermal method and characterized by XRD, SEM, EDS, and XPS, respectively. Planar chemical gas sensors based on the as-prepared powders were fabricated with screen-printing technique, and their responsive characteristics towards SO_2 , a most important SF_6 decomposition

byproduct under partial discharge, were systematically investigated with the CGS-ITP intelligent gas sensing analysis system. Lower operating temperature, higher sensing response, good linearity, quick response-recovery characteristic, and good stability were measured with the fabricated planar chemical sensor. All results demonstrate that the sensor fabricated with hierarchical ZnO nanoflowers is a promising candidate for detecting SO_2 .

Competing Interests

The authors declare that there are no competing interests regarding the publication of this paper.

Acknowledgments

This work has been supported in part by the National Natural Science Foundation of China (no. 51507144), China Postdoctoral Science Foundation funded project (no. 2015M580771), Postdoctoral Science Funded Project of Chongqing (no. Xm2015016), and Fundamental Research Funds for the Central Universities (nos. XDJK2015B005 and SWU114051).

References

- [1] J. Tang, F. Liu, X. X. Zhang, Q. H. Meng, and J. B. Zhou, "Partial discharge recognition through an analysis of SF_6 decomposition products part I: decomposition characteristics of SF_6 under four different partial discharges," *IEEE Transactions on Dielectrics and Electrical Insulation*, vol. 19, no. 1, pp. 29–36, 2012.
- [2] J. Tang, F. Liu, Q. H. Meng, X. X. Zhang, and J. G. Tao, "Partial discharge recognition through an analysis of SF_6 decomposition products part 2: feature extraction and decision tree-based pattern recognition," *IEEE Transactions on Dielectrics and Electrical Insulation*, vol. 19, no. 1, pp. 37–44, 2012.
- [3] W.-T. Tsai, "The decomposition products of sulfur hexafluoride (SF_6): reviews of environmental and health risk analysis," *Journal of Fluorine Chemistry*, vol. 128, no. 11, pp. 1345–1352, 2007.
- [4] C. T. Dervos and P. Vassiliou, "Sulfur hexafluoride (SF_6): global environmental effects and toxic byproduct formation," *Journal of the Air and Waste Management Association*, vol. 50, no. 1, pp. 137–141, 2000.
- [5] J. I. Baumbach, P. Pilzecker, and E. Trindade, "Monitoring of circuit breakers using ion mobility spectrometry to detect SF_6 -decomposition," *International Journal for Ion Mobility Spectrometry*, vol. 2, no. 1, pp. 35–39, 1999.
- [6] R. Kurte, C. Beyer, H. M. Heise, and D. Klockow, "Application of infrared spectroscopy to monitoring gas insulated high-voltage equipment: electrode material-dependent SF_6 decomposition," *Analytical and Bioanalytical Chemistry*, vol. 373, no. 7, pp. 639–646, 2002.
- [7] D. Velasco-Arias, D. Díaz, P. Santiago-Jacinto, G. Rodríguez-Gattorno, A. Vázquez-Olmos, and S. E. Castillo-Blum, "Direct interaction of colloidal nanostructured ZnO and SnO_2 with NO and SO_2 ," *Journal of Nanoscience and Nanotechnology*, vol. 8, no. 12, pp. 6389–6397, 2008.
- [8] X. X. Zhang, J. B. Zhang, Y. C. Jia, P. Xiao, and J. Tang, "TiO₂ nanotube array sensor for detecting the SF_6 decomposition product SO_2 ," *Sensors*, vol. 12, no. 3, pp. 3302–3313, 2012.
- [9] S. D. Peng, G. L. Wu, and W. Song, "Synthesis, characteristics and enhanced sulfur dioxide sensing properties of Cu-doped SnO_2 microspheres," *Sensors & Transducers*, vol. 156, no. 9, pp. 310–316, 2013.
- [10] J. W. Gong and X. F. Wan, "Electrospun ZnO nanofibers for selectively detecting SF_6 decomposition byproduct SO_2 ," *Sensor Letters*, vol. 13, no. 10, pp. 857–861, 2015.
- [11] X. X. Zhang, J. B. Zhang, J. Tang, and B. Yang, "Gas-sensing simulation of single-walled carbon nanotubes applied to detect gas decomposition products of SF_6 ," *Journal of Computational and Theoretical Nanoscience*, vol. 9, no. 8, pp. 1096–1100, 2012.
- [12] Q. Zhou, W. Chen, S. Peng, and W. Zeng, "Hydrothermal synthesis and acetylene sensing properties of variety low dimensional zinc oxide nanostructures," *The Scientific World Journal*, vol. 2014, Article ID 489170, 8 pages, 2014.
- [13] Q. Qi, T. Zhang, Q. Yu et al., "Properties of humidity sensing ZnO nanorods-base sensor fabricated by screen-printing," *Sensors and Actuators B: Chemical*, vol. 133, no. 2, pp. 638–643, 2008.
- [14] Z. H. Jing and J. H. Zhan, "Fabrication and gas-sensing properties of porous ZnO nanoplates," *Advanced Materials*, vol. 20, no. 23, pp. 4547–4551, 2008.
- [15] Q. Zhou, M. Q. Cao, W. D. Li, C. Tang, and S. P. Zhu, "Research on acetylene sensing properties and mechanism of SnO_2 based chemical gas sensor decorated with Sm_2O_3 ," *Journal of Nanotechnology*, vol. 2015, Article ID 714072, 7 pages, 2015.
- [16] W. Zeng, T. M. Liu, D. J. Liu, and E. J. Han, "Hydrogen sensing and mechanism of M-doped SnO_2 ($M = \text{Cr}^{3+}$, Cu^{2+} and Pd^{2+}) nanocomposite," *Sensors and Actuators B: Chemical*, vol. 160, no. 1, pp. 455–462, 2011.
- [17] Q. Qi, T. Zhang, L. Liu, and X. Zheng, "Synthesis and toluene sensing properties of SnO_2 nanofibers," *Sensors and Actuators B: Chemical*, vol. 137, no. 2, pp. 471–475, 2009.
- [18] W. Zeng, T. M. Liu, and Z. C. Wang, "Enhanced gas sensing properties by SnO_2 nanosphere functionalized TiO₂ nanobelts," *Journal of Materials Chemistry*, vol. 22, no. 8, pp. 3544–3548, 2012.
- [19] J. Singh, A. Mukherjee, S. K. Sengupta, J. Im, G. W. Peterson, and J. E. Whitten, "Sulfur dioxide and nitrogen dioxide adsorption on zinc oxide and zirconium hydroxide nanoparticles and the effect on photoluminescence," *Applied Surface Science*, vol. 258, no. 15, pp. 5778–5785, 2012.
- [20] W. Zeng, T. Liu, Z. Wang, S. Tsukimoto, M. Saito, and Y. Ikuhara, "Selective detection of formaldehyde gas using a Cd-Doped TiO₂- SnO_2 sensor," *Sensors*, vol. 9, no. 11, pp. 9029–9038, 2009.
- [21] K. Zheng, L. Gu, D. Sun, X. Mo, and G. Chen, "The properties of ethanol gas sensor based on Ti doped ZnO nanotetrapods," *Materials Science and Engineering B: Solid-State Materials for Advanced Technology*, vol. 166, no. 1, pp. 104–107, 2010.
- [22] A. Wei, Z. Wang, L.-H. Pan et al., "Room-temperature NH_3 gas sensor based on hydrothermally grown ZnO nanorods," *Chinese Physics Letters*, vol. 28, no. 8, pp. 702–706, 2011.
- [23] Q. Zhou, W. G. Chen, L. N. Xu, and S. D. Peng, "Hydrothermal synthesis of various hierarchical ZnO nanostructures and their methane sensing properties," *Sensors*, vol. 13, no. 5, pp. 6171–6182, 2013.
- [24] M. Forouzani, H. R. Mardani, M. Ziari, A. Malekzadeh, and P. Biparva, "Comparative study of oxidation of benzyl alcohol: influence of Cu-doped metal cation on nano ZnO catalytic activity," *Chemical Engineering Journal*, vol. 275, no. 9, pp. 220–226, 2015.

- [25] M. Israr-Qadir, S. Jamil-Rana, O. Nur, M. Willander, L. A. Larsson, and P. O. Holtz, "Fabrication of ZnO nanodisks from structural transformation of ZnO nanorods through natural oxidation and their emission characteristics," *Ceramics International*, vol. 40, no. 1, pp. 2435–2439, 2014.
- [26] J. Guo, J. Zhang, M. Zhu, D. Ju, H. Xu, and B. Cao, "High-performance gas sensor based on ZnO nanowires functionalized by Au nanoparticles," *Sensors and Actuators B: Chemical*, vol. 199, pp. 339–345, 2014.
- [27] X. B. Li, S. Y. Ma, F. M. Li et al., "Porous spheres-like ZnO nanostructure as sensitive gas sensors for acetone detection," *Materials Letters*, vol. 100, no. 6, pp. 119–123, 2013.

Research Article

Structural and Electrical Studies on ZnO-Based Thin Films by Laser Irradiation

Shanyue Zhao,¹ Yinqun Hua,^{1,2} Ruifang Chen,² Jian Zhang,¹ and Ping Ji¹

¹School of Material and Science Engineering, Jiangsu University, Zhenjiang 212013, China

²School of Mechanics Engineering, Jiangsu University, Zhenjiang 212013, China

Correspondence should be addressed to Yinqun Hua; huayq@ujs.edu.cn and Ruifang Chen; crf0504@aliyun.com

Received 20 September 2015; Revised 11 January 2016; Accepted 7 February 2016

Academic Editor: Oded Millo

Copyright © 2016 Shanyue Zhao et al. This is an open access article distributed under the Creative Commons Attribution License, which permits unrestricted use, distribution, and reproduction in any medium, provided the original work is properly cited.

The effects of laser irradiation on the structural and electrical properties of ZnO-based thin films were investigated. The XRD pattern shows that the thin films were highly textured along the *c*-axis and perpendicular to the surface of the substrate. Raman spectra reveal that Bi₂O₃ segregates mainly at ZnO-ZnO grain boundaries. After laser irradiation processing, the grain size of the film was reduced significantly, and the intrinsic atomic defects of grain boundaries and Bi element segregated at the grain boundary were interacted frequently and formed the composite defects of acceptor state. The nonlinear coefficient increased to 24.31 and the breakdown voltage reduced to 5.34 V.

1. Introduction

ZnO varistors exhibit high nonlinear coefficient, low leakage current, and high surge absorbing ability. They have been extensively applied on high-voltage protection of electrical equipment since the 1970s, such as inhibiting lightning over-voltage of electrical power system [1–5]. However, modern-day electronic components, mainly based on silicon, are more susceptible not only to electrical overvoltage transients, but also to damage by electromagnetic pulses or electromagnetic interference (EMI) noise that is now strictly regulated by law throughout the world [6, 7]. Therefore, the industry has high demands for low-voltage varistors. For a low-voltage varistor, it is required to be of few microns in thickness to reduce nonlinear voltage. ZnO films with good quality were grown through different methods, such as hydrothermal method [8], sol-gel technique [9], electron-beam evaporation [10], pulse laser deposition [11], and magnetron sputtering [12]. Among all, magnetrons puttering shows several advantages such as good adhesion between film and substrate, low substrate temperature, scalability to large areas, great thickness uniformity with a deposition rate range, and high film density [12–15].

Recently, laser irradiation technique has been used on thin films as an efficient method to improve the crystalline

quality and increase the electron donors [16–19]. Laser irradiation has several advantages, including fast crystallization at room temperature, possibility of local crystallization, crystallization of thin films on low melting point substrates, and increasing charge carriers through a photoconductivity effect. Tsay and Wang [18] performed ZnO thin films on glass by sol-gel and used KrF excimer laser for annealing. They reported that the crystallinity levels and average crystallite size of thin films with excimer laser irradiation were greater than those of thermally annealed thin films. Tsang et al. [19] fabricated transparent conducting AZO thin films using KrF excimer laser irradiation. They reported that the electrical and optical characteristics of AZO thin films irradiated by excimer laser improved significantly.

To the best of our knowledge, no report on ZnO-based thin film varistors with laser irradiation for low-voltage application exists. In our previous work [20], we studied the effect of laser shock on electrical property of ZnO varistor ceramics. In the present work, ZnO-based thin films of high quality were prepared by RF magnetron sputtering technique on Si (111) substrates. After examinations, the films were subsequently treated by laser irradiation. The paper has studied the structural and electrical properties of the ZnO-based thin film varistors for low-voltage application.

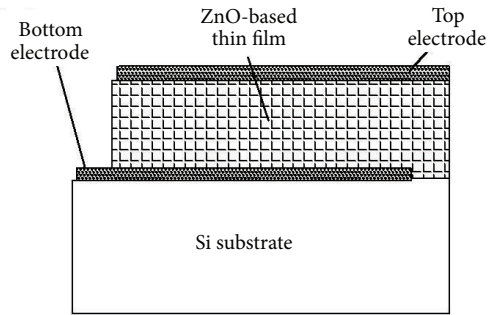


FIGURE 1: The structure of the ZnO-based thin film varistors.

2. Experiment

ZnO-based thin films were deposited on Si (111) substrates by RF magnetron sputtering technique and followed by annealing at 700°C for 4 h in the air. The target, ZnO-based ceramic with 60 mm in diameter and 5 mm in thickness, was formed by dry pressing and subsequently sintered in the air. The raw materials of the target were mixed powders and the matching composition was 96.5 mol% ZnO + 2 mol% Bi₂O₃ + 1.5 mol% (MnO₂, Co₂O₃, Cr₂O₃, and Sb₂O₃). It is the optimized composition investigated by the authors in our previous works. Si (111) which was used as the substrate for ZnO thin films deposition were cleaned in an ultrasonic bath with ethanol for 15 min than dried for use. The substrates were sprayed gold in the metal-spraying equipment for 5 min, to prepare a layer of bottom electrode on the Si substrate. Using the sky-0826138 RF magnetron sputtering instrument, the background vacuum degree of the chamber was less than 1×10^{-4} Pa. The sputtering pressure was 3.0 Pa, and the Argon flow was 30 sccm. The sputtering time was 60 min, and the sputtering power was 150 W. The substrate temperature was 300°C. The film thickness was controlled within 2 microns. After the laser irradiation processing, the laser irradiation area was covered with gold to prepare the top electrode. Figure 1 shows the structure of the ZnO-based thin film varistors.

The 0.2 mm aluminum foil adhered to the film surface as the absorption layer. The homemade liquids were coated on the aluminum foil surface as the constraint layer. The thickness was 0.5 mm. The laser irradiation parameters are as followings: light spot diameter of 6 mm, wavelength of 1064 nm, pulse width of 5 ns, pulse energy of 0.8 J. Finally, the samples were set in the mold to conduct the laser irradiation experiment. After the laser irradiation processing, the films' surfaces were fine, which showed that as long as the parameters of laser irradiation were appropriate, laser irradiation could be applied on the films completely.

The structural properties were characterized by X-ray diffractometer (XRD) with CuK α radiation. The surface morphology and root mean square (RMS) roughness level of the films were examined by tapping atomic force microscope (AFM). Plane-view micrographs of ZnO-based thin films were taken with a field-emission scanning electron

microscope (FE-SEM). Raman spectra were excited with the 532 nm line of a laser at an incident power of 10 mW and obtained in the range 0–3000 cm⁻¹. The J - V curves are measured by transistor characteristic meter. The breakdown voltage $U_{1\text{mA}}$ (V) and leakage current J_L ($\mu\text{A}/\text{mm}^2$) are measured by piezoresistor general measuring instrument.

3. Results and Discussions

The X-ray diffraction patterns of the ZnO-based thin films before and after irradiation are shown in Figure 2. Only the (002) peaks are observed in the XRD patterns, which shows that the films are highly textured along the c -axis and perpendicular to the surface of the substrate. This diffraction peak is indexed to those of hexagonal wurtzite zinc oxide and no diffraction peaks of any other phases or impurities are detected [8, 9, 11]. After irradiation, the intensity of (002) ZnO peak increases and there is a shift to larger angles. This trend with the shift of 2θ in XRD patterns suggests that the Bi³⁺ ions occupied the Zn²⁺ substitutional sites [15, 21]. This result also shows that laser irradiation can facilitate the substitution of Bi³⁺ ions to Zn²⁺ ions [18].

Figure 3 shows the AFM morphologies for the films, which illustrate the surface morphology of the thin films. (a) is the sample before irradiation and (b) is the sample after irradiation. After laser irradiation, the film surface morphology changes significantly. Corresponding to the above two samples, the RMS surface roughnesses are 31.4 and 2.8 nm. The film treated by laser irradiation has a relative smooth and dense surface morphology. At the initial state, the laser shock wave passes through the rigid aluminum foil adhering to the film surface and reaches the bottom of the aluminum foil. For the impedance mismatch of the aluminum foil and the film, strong contact pressure appears between the contact point of the aluminum foil and the film. The sharp protrusions are compressed at the strong contact pressure and this is characterized by the great reduction of surface roughness. Figure 4 shows the morphology and particle sizes of prepared film by SEM. The histograms reveal the distribution of average grain size, which are reasonably described by the Gaussian function, showing tight size distribution with average sizes of approximately 191 and 139 nm in diameter, respectively.

Figure 5 shows the Raman spectrum of ZnO-based thin film. A larger peak shift at 437 cm⁻¹ is observed, which is almost the same position as the standard ZnO. It indicates that the thin film is almost free of stress. Theoretically, it is difficult to substitute Zn²⁺ by Bi³⁺ in ZnO crystal, for the radius of Bi³⁺ is much larger than Zn²⁺. The former results indicate that Bi₂O₃ segregates mainly at ZnO-ZnO grain boundaries as Bi-rich phases during sintering in the ZnO-Bi₂O₃ system. The Bi elements distribute evenly throughout the thin film, and the distribution of Bi appears in certain regularity, which are almost distributed at the grain boundaries. After laser irradiation processing, grain boundaries increase with the grain refinement. In this condition, the intrinsic atomic defects of grain boundaries and Bi element segregated at the grain boundary interact frequently, forming the composite defects of acceptor state [22, 23]. So the interface state density

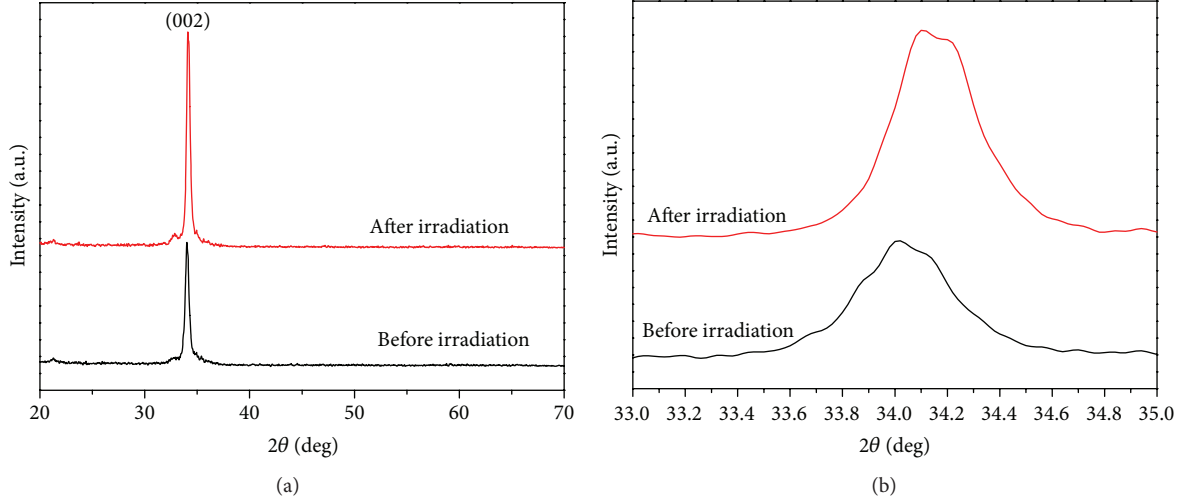


FIGURE 2: XRD patterns of ZnO-based thin films.

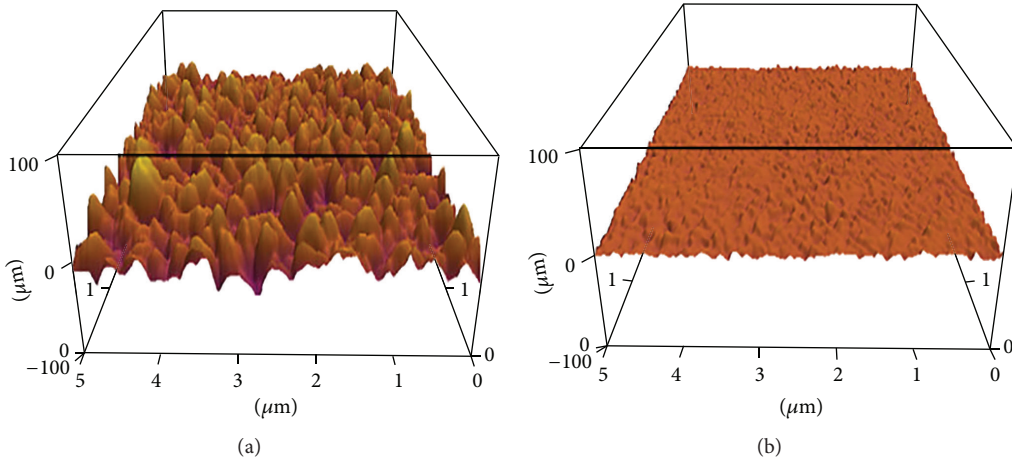


FIGURE 3: AFM micrographs of the ZnO-based thin films.

N_S of grain boundaries increase greatly, which promotes the increasing of barrier height Φ_B and the nonlinear coefficient. Therefore, the pressure-sensitive electrical properties of ZnO-based ceramic film of laser irradiation state are excellent.

Table 1 is the result of electrical properties. The nonlinear coefficient is α , breakdown voltage is $U_{1\text{mA}}$ (V), and leakage current is J_L ($\mu\text{A}/\text{mm}^2$). After laser irradiation processing, the nonlinear coefficient is 24.31, which increases by 40.8%, and breakdown voltage is 5.34 V, which decreases by 20.7%. Leakage current density is as low as $2.03 \mu\text{A}/\text{mm}^2$, which decreases by 12.1%. Similar investigations have been done by other researchers. Horio et al. [13] prepared the ZnO/ Pr_6O_{11} films on the glass substrates by the RF magnetron sputtering technique, and the film thickness was 600 nm/400 nm. The breakdown voltage was 20 V, and the nonlinear coefficient was 10. Mišta et al. [14] prepared the Bi-doped films on the ITO/Glass using Zn-Bi target by the RF magnetron sputtering technique. The results displayed that the breakdown voltage was from a few volts to dozens of volts, and the nonlinear

TABLE 1: Electrical properties of films before and after laser-irradiation processing.

Parameters	Before irradiation (I)	After irradiation (II)	Rate (%)
α	17.26	24.31	40.8
$U_{1\text{mA}}$ (V)	6.73	5.34	-20.7
J_L ($\mu\text{A}/\text{mm}^2$)	2.31	2.03	-12.1

coefficient was 15. Jeong [24] prepared low-voltage ZnO varistors and investigated the field failure; after polishing, the breakdown voltage was 9.71 V, and the nonlinear coefficient was 20.35. Therefore, the electrical properties improve significantly by the laser irradiation processing.

The grain boundary of ZnO-based ceramic film is a thin disorder area, where a large number of interface states and electron traps exist. They are able to capture the free electrons in the ZnO grains. The electrons of grain boundaries are

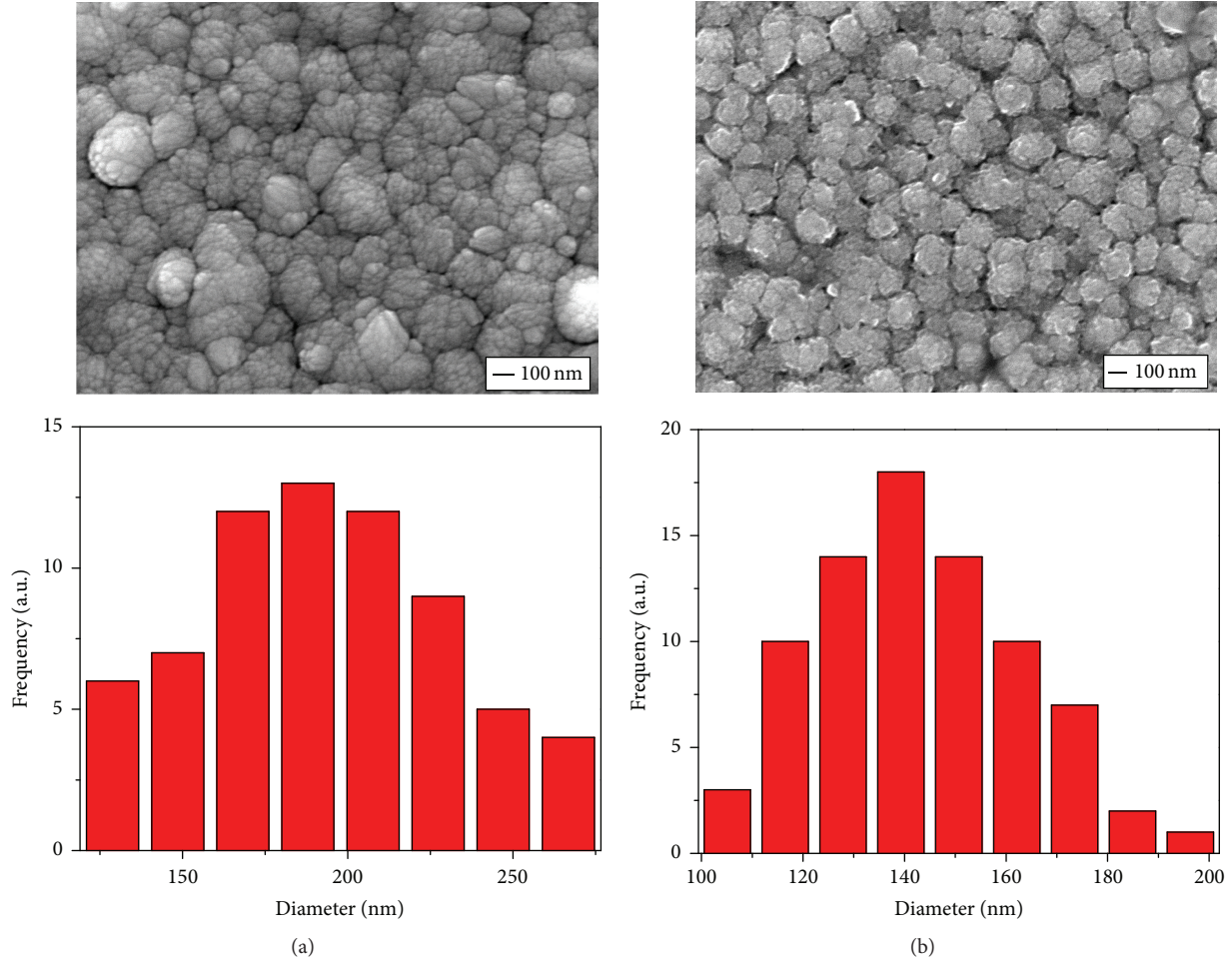


FIGURE 4: SEM micrographs of the ZnO-based thin films.

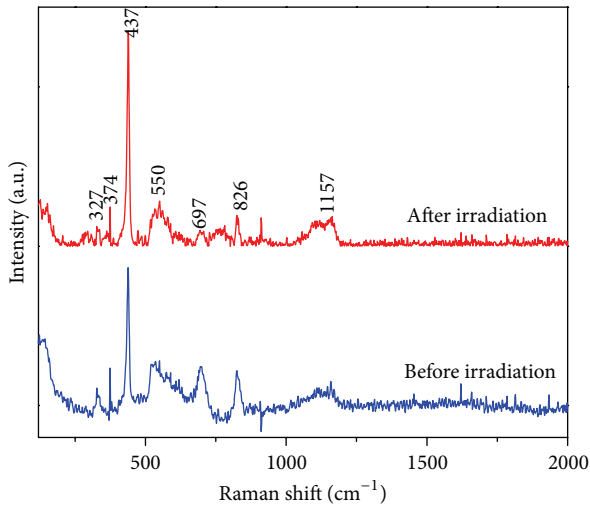


FIGURE 5: Raman spectroscopy of ZnO-based thin films.

depleted, and depletion layers are formed. Consequently, electronic barriers with certain depth have been formed from grain surfaces into body. The barrier height is Φ_B , which is

called Double Schottky barrier [25]. It is the source of voltage-sensitive electrical property.

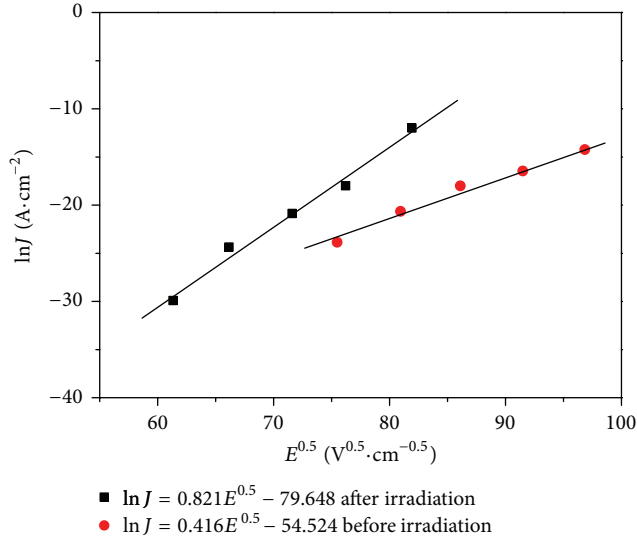
Nonlinear characteristics of ZnO-based film originate from the grain boundary barrier. To study the impact of laser irradiation processing on the electric properties of ZnO-based ceramic film, we adopted the double Schottky barrier model proposed by Gupta and Carlson [26] to explain the change of electrical property. At preswitch region, there is a relationship between the current density and the extra electric field obtained from the model, which is shown in [27]

$$J = AT^2 \exp \left[\frac{(\beta E^{0.5} - \Phi_B)}{(kT)} \right]. \quad (1)$$

J is current density, A is Richardson constant, T is absolute temperature, E is electric field intensity, Φ_B is barrier height, and K is Boltzmann constant. $\beta = \{1/(\gamma\omega)[2e^3/(4\pi\epsilon_0\epsilon_r)]\}^{1/2}$ [17], γ is grain number of unit length, ω is Barrier width, e is electron charge (1.602×10^{-19} C), ϵ_0 is vacuum dielectric constant (8.85×10^{-14} F/cm), and ϵ_r is relative dielectric constant (8.5). Setting T as 25°C, $\ln J-E^{0.5}$ fitting diagram of film and film of laser irradiation state are shown in Figure 5. The boundary characteristic

TABLE 2: The characteristic parameters of grain-boundary of ZnO-based ceramic films before and after laser-irradiation processing.

State	Barrier height Φ_B (eV)	Barrier width ω (Å)	Donor concentration N_D (10^{22} cm $^{-3}$)	Density of interface states N_S (10^{14} cm $^{-2}$)
Before irradiation (I)	1.86	1.13	13.5	15.3
After irradiation (II)	2.41	0.31	227	71.6

FIGURE 6: The relation patterns of $\ln J - E^{0.5}$ of the ZnO-based thin films before and after irradiation.

parameters were calculated by Figure 6, which were listed in Table 2, including the barrier height Φ_B , barrier width ω , interface-state density N_D , and donor concentration N_S .

Table 2 shows that after laser irradiation processing, barrier height Φ_B increased, barrier width decreased, donor concentration N_D and interface-state density N_S also increased greatly. According to [27]

$$\alpha \approx \left(\frac{\nu}{E}\right) \Phi_B^{3/2}. \quad (2)$$

Nonlinear coefficient α is proportional to potential barrier height Φ_B . Φ_B rose from 1.86 to 2.41, which prompted the increasing of α from 12.94 to 21.38. So the increasing of barrier height can effectively improve the nonlinear coefficient. According to formula $\Phi_B = e^2 N_S^2 / 2\epsilon_0 \epsilon_r N_D$ [18], barrier height Φ_B is closely related to the interface-state density N_S and donor concentration N_D . After laser irradiation processing, the thin film produced the lattice distortion, which increased the amount of intrinsic atomic defects of ZnO. There is no second phase diffraction peak in the X-ray diffraction patterns of samples, but which cannot exclude the doping elements as indeterminate type segregating at the grain boundaries.

4. Conclusions

After laser irradiation processing, electrical properties of the films have been improved in different degrees. The nonlinear coefficient was 24.31, which was increased by 40.8%. The

breakdown voltage was 5.34 V, which was reduced by 20.7%. Leakage current density was as low as $2.03 \mu\text{A}/\text{mm}^2$, which was reduced by 12.7%. The grain size was reduced and the clearance between the adjacent particles also decreased. The film produced the lattice distortion, prompting the increasing of ZnO intrinsic atomic defects. With the refinement of the grain, grain boundaries were increasing. In this condition, the intrinsic atomic defects of grain boundaries and Bi element segregated at the grain boundaries interact frequently, forming the composite defects of acceptor state. The interface-state density N_S of the grain boundaries increased greatly, increasing the barrier height Φ_B . Therefore, the pressure-sensitive electrical properties of ZnO-based ceramic film of laser irradiation state are excellent.

Conflict of Interests

The authors declare that there is no conflict of interests regarding the publication of this paper.

References

- [1] M. Matsuoka, "Nonohmic properties of zinc oxide ceramics," *Japanese Journal of Applied Physics*, vol. 10, no. 6, pp. 736–746, 1971.
- [2] T. K. Gupta, "Application of zinc oxide varistors," *Journal of the American Ceramic Society*, vol. 73, no. 7, pp. 1817–1840, 1990.
- [3] D. R. Clarke, "Varistor ceramics," *Journal of the American Ceramic Society*, vol. 82, no. 3, pp. 485–502, 1999.
- [4] S. Anas, R. V. Mangalaraja, M. Poothayal, S. K. Shukla, and S. Ananthakumar, "Direct synthesis of varistor-grade doped nanocrystalline ZnO and its densification through a step-sintering technique," *Acta Materialia*, vol. 55, no. 17, pp. 5792–5801, 2007.
- [5] P. R. Bueno, J. A. Varela, and E. Longo, "SnO $_2$, ZnO and related polycrystalline compound semiconductors: an overview and review on the voltage-dependent resistance (non-ohmic) feature," *Journal of the European Ceramic Society*, vol. 28, no. 3, pp. 505–529, 2008.
- [6] R. Puyan , "Applications and product development in varistor technology," *Journal of Materials Processing Technology*, vol. 55, no. 3–4, pp. 268–277, 1995.
- [7] A. Rafferty, Y. Gun'ko, and R. Raghavendra, "An investigation of co-fired varistor-ferrite materials," *Journal of the European Ceramic Society*, vol. 24, no. 7, pp. 2005–2013, 2004.
- [8] Z. N. Urgessa, O. S. Oluwafemi, and J. R. Botha, "Hydrothermal synthesis of ZnO thin films and its electrical characterization," *Materials Letters*, vol. 79, no. 15, pp. 266–269, 2012.
- [9] Y. M. Li, L. H. Xu, X. G. Li, X. G. Shen, and A. L. Wang, "Effect of aging time of ZnO sol on the structural and optical properties of ZnO thin films prepared by sol-gel method," *Applied Surface Science*, vol. 256, no. 14, pp. 4543–4547, 2010.

- [10] H. Z. Wu, K. M. He, D. J. Qiu, and D. M. Huang, "Low-temperature epitaxy of ZnO films on Si(001) and silica by reactive e-beam evaporation," *Journal of Crystal Growth*, vol. 217, no. 1, pp. 131–137, 2000.
- [11] X. Q. Wei, J. Z. Huang, M. Y. Zhang, Y. Du, and B. Y. Man, "Effects of substrate parameters on structure and optical properties of ZnO thin films fabricated by pulsed laser deposition," *Materials Science and Engineering B*, vol. 166, no. 2, pp. 141–146, 2010.
- [12] D. R. Hernández-Socorro, Z. Montiel-González, S. E. Rodil-Posada et al., "Effect of 8 MeV Si ions irradiation and thermal annealing in ZnO thin films," *Journal of Crystal Growth*, vol. 354, no. 1, pp. 169–173, 2012.
- [13] N. Horio, M. Hiramatsu, M. Nawata, K. Imaeda, and T. Torii, "Preparation of zinc oxide/metal oxide multilayered thin films for low-voltage varistors," *Vacuum*, vol. 51, no. 4, pp. 719–722, 1998.
- [14] W. Miśta, J. Ziąja, and A. Gubański, "Varistor performance of nanocrystalline Zn-Bi-O thin films prepared by reactive RF magnetron sputtering at room temperature," *Vacuum*, vol. 74, no. 2, pp. 293–296, 2004.
- [15] M. Jiang, X. Liu, and H. Wang, "Conductive and transparent Bi-doped ZnO thin films prepared by rf magnetron sputtering," *Surface and Coatings Technology*, vol. 203, no. 24, pp. 3750–3753, 2009.
- [16] Y. Zhao and Y. Jiang, "Effect of KrF excimer laser irradiation on the properties of ZnO thin films," *Journal of Applied Physics*, vol. 103, no. 11, Article ID 114903, 2008.
- [17] Y. Hou and A. H. Jayatissa, "Effect of laser irradiation on gas sensing properties of sol-gel derived nanocrystalline Al-doped ZnO thin films," *Thin Solid Films*, vol. 562, no. 26, pp. 585–591, 2014.
- [18] C.-Y. Tsay and M.-C. Wang, "Structural and optical studies on sol-gel derived ZnO thin films by excimer laser annealing," *Ceramics International*, vol. 39, no. 1, pp. 469–474, 2013.
- [19] W. M. Tsang, F. L. Wong, M. K. Fung, J. C. Chang, C. S. Lee, and S. T. Lee, "Transparent conducting aluminum-doped zinc oxide thin film prepared by sol-gel process followed by laser irradiation treatment," *Thin Solid Films*, vol. 517, no. 2, pp. 891–895, 2008.
- [20] Y. Q. Hua, G. Ji, and Z. Z. Sun, "Effect of laser shock wave on electrical property of ZnO varistor ceramics," *Laser Technology*, vol. 31, no. 1, pp. 133–136, 2011 (Chinese).
- [21] I. Lorite, J. Wasik, T. Michalsky, R. Schmidt-Grund, and P. Esquinazi, "Hydrogen influence on the electrical and optical properties of ZnO thin films grown under different atmospheres," *Thin Solid Films*, vol. 556, no. 1, pp. 18–22, 2014.
- [22] F. Oba and I. Tanaka, "Effect on oxidation of chemical bonding around 3d transition-metal impurities in ZnO," *Japanese Journal of Applied Physics*, vol. 38, no. 6, pp. 3570–3574, 1999.
- [23] F. Oba, H. Adachi, and I. Tanaka, "Energetics and electronic structure of point defects associated with oxygen excess at a tilt boundary of ZnO," *Journal of Materials Research*, vol. 15, no. 10, pp. 2167–2175, 2000.
- [24] J.-S. Jeong, "Field failure mechanism and reproduction due to moisture for low-voltage ZnO varistors," *Microelectronics Reliability*, vol. 53, no. 9–11, pp. 1632–1637, 2013.
- [25] L. J. Brillson, H. L. Mosbacker, M. J. Hetzer et al., "Dominant effect of near-interface native point defects on ZnO Schottky barriers," *Applied Physics Letters*, vol. 90, no. 10, Article ID 102116, 2007.
- [26] T. K. Gupta and W. G. Carlson, "A grain-boundary defect model for instability/stability of a ZnO varistor," *Journal of Materials Science*, vol. 20, no. 10, pp. 3487–3500, 1985.
- [27] S. A. Pianaro, P. R. Bueno, P. Olivi, E. Longo, and J. A. Vareia, "Effect of Bi₂O₃ addition on the microstructure and electrical properties of the SnO₂·CoO·Nb₂O₅ varistor system," *Journal of Materials Science Letters*, vol. 16, no. 8, pp. 634–638, 1997.

Research Article

Amorphous Silicon-Germanium Films with Embedded Nanocrystals for Thermal Detectors with Very High Sensitivity

Cesar Calleja, Alfonso Torres, Pedro Rosales-Quintero, and Mario Moreno

National Institute of Astrophysics, Optics and Electronics (INAOE), Electronics Department, Laboratory of Innovation in MEMS (LI-MEMS), 72840 Tonantzintla, PUE, Mexico

Correspondence should be addressed to Mario Moreno; mmoreno@inaoep.mx

Received 19 October 2015; Revised 6 January 2016; Accepted 11 January 2016

Academic Editor: Wen Zeng

Copyright © 2016 Cesar Calleja et al. This is an open access article distributed under the Creative Commons Attribution License, which permits unrestricted use, distribution, and reproduction in any medium, provided the original work is properly cited.

We have optimized the deposition conditions of amorphous silicon-germanium films with embedded nanocrystals in a plasma enhanced chemical vapor deposition (PECVD) reactor, working at a standard frequency of 13.56 MHz. The objective was to produce films with very large Temperature Coefficient of Resistance (TCR), which is a signature of the sensitivity in thermal detectors (microbolometers). Morphological, electrical, and optical characterization were performed in the films, and we found optimal conditions for obtaining films with very high values of thermal coefficient of resistance ($\text{TCR} = 7.9\% \text{K}^{-1}$). Our results show that amorphous silicon-germanium films with embedded nanocrystals can be used as thermosensitive films in high performance infrared focal plane arrays (IRFPAs) used in commercial thermal cameras.

1. Introduction

Detectors and infrared focal plane arrays (IRFPAs), also known as thermal detectors (or thermal FPAs), are used in a wide variety of applications as industrial, medical, security, surveillance, and military [1–4]. In a thermal detector, the incident infrared (IR) radiation is absorbed by a thermosensitive material, resulting in a change of one of its physical properties, which is used to get an electrical signal output. In thermal detectors, the thermosensing material must have a high sensitivity to temperature and must be compatible with the standard silicon (Si) CMOS fabrication process, for low cost manufacture and integration with a Si CMOS readout integrated circuit (ROIC).

The temperature sensitivity of a material is given by its Temperature Coefficient of Resistance (TCR), which is related to the activation energy (E_a) of the material by (1), where K is the Boltzmann constant and T is the temperature:

$$\text{TCR} = -\frac{E_a}{KT^2}. \quad (1)$$

Up to now, amorphous semiconductors have been widely used as thermosensitive materials in commercial microbolometers arrays (IRFPAs). These materials have advantages over other thermosensitive materials, since they are compatible with standard Si CMOS technology and have high E_a and high TCR values.

In this aspect, a-Si:H has a direct band gap (1.6–1.8 eV), high activation energy ($E_a = 0.8 \text{ eV}$), and very high thermal coefficient of resistance ($\text{TCR} = -10\% \text{K}^{-1}$) and also has a very high room temperature resistivity ($\sim 10^9 \Omega \text{ cm}$), which is noncompatible with the Si CMOS ROIC input impedance.

In order to reduce the high resistance of a-Si:H, boron doping has been used. The boron doped a-Si:H films have an improved room temperature conductivity (σ_{RT}) in several orders of magnitude and also showed a high reduction in E_a (0.22 eV) and TCR ($-2.8\% \text{K}^{-1}$) [5, 6]. Despite the above, a-Si:H,B has been adopted as IR sensing film for microbolometers contained in very large IRFPAs (1024×768) [4, 6, 7]. Recently, the control of the $\text{BCl}_3/\text{SiH}_4$ gas flow rate during the a-Si:H,B films deposition by PECVD has been demonstrated, in order to improve the TCR to values as large as $-3.9\% \text{K}^{-1}$ [7].

TABLE 1: Deposition conditions of two series of pm-Si_xGe_y:H thin films prepared by PECVD.

	Sample number	Temperature °C	Pressure mTorr	SiH ₄ sccm	GeH ₄ sccm	H ₂ sccm
Series #1	P11	200°C	500	50	50	110
	P12		1000			
	P13		1200			
Series #2	P21		500	90	10	110
	P22		1000			
	P23		1200			

Among the other materials that have been used in thermal detectors is Vanadium Oxide (VO_x) which was the first material used in high performance microbolometers, due to its relatively high TCR of $-2\% \text{ K}^{-1}$ [8]; however, this material is not compatible with the Si CMOS technology.

Amorphous germanium silicon oxide (a-Ge_xSi_{1-x}O_y) deposited by RF sputtering also has been reported with large TCR values of $-4.8\% \text{ K}^{-1}$ [9] and semiconducting yttrium barium copper oxide (YBCO) has been studied as IR sensing film, with large TCR values of $-3.4\% \text{ K}^{-1}$ [10].

Recently, nanostructured VO_x films have been reported in microbolometers with very large TCR values of $-5.6\% \text{ K}^{-1}$ [11]. However, this material is also incompatible with the Si CMOS process, which restricts its incorporation in very large IRFPAs based on the Si CMOS technology.

On the other hand, even though amorphous semiconductors as a-Si:H,B are the IR sensing materials of choice in the most developed IRFPAs, they have some drawbacks due to their inherent high density of states in band gap, high density of defects, poor transport properties, and poor stability against radiation [12].

Recently, the production of amorphous semiconductors with embedded nanocrystals has been demonstrated; those materials are referenced as polymorphous semiconductors, as polymorphous silicon (pm-Si:H) [12–15], which are mainly investigated for applications in thin film solar cells. The presence of the embedded nanocrystals in the amorphous matrix impacts on the material properties, reducing the density of states and defects and also improving the transport properties and stability against radiation. Moreover, polymorphous semiconductors preserve the characteristic of amorphous semiconductors as direct band gap, high E_a , and high TCR [12, 13].

Polymorphous semiconductors practically have not been used for thermal detection applications; however, they are excellent candidates to be used as thermosensing materials in high performance microbolometers in commercial IRFPAs. In our previous work, we have shown that it is possible to produce pm-Si_xGe_y:H thin films in a Low Frequency Plasma Enhanced Chemical Vapor Deposition (LF-PECVD) reactor working at 110 KHz, using SiH₄ and GeH₄ as precursor gases [16]. However, an LF-PECVD technique is not standard in the microelectronics industry, and moreover in this technique, due to its low frequency, the ions have a contribution in the plasma and the properties of the deposited films can be affected. The ions in the plasma can help to dissociate more effectively the reactive species and also can produce

damage in the film, due to ion bombardment. Therefore, the results obtained by LF-PECVD could not be reproducible in a standard PECVD reactor working a radio frequency (RF) of 13.56 MHz, which is used in the microelectronics industry.

In the present work, we studied the deposition of pm-Si_xGe_y:H thin films in a RF-PECVD reactor working at a frequency of 13.56 MHz. Moreover, we studied the effect of the most important deposition parameters (deposition pressure and SiH₄/GeH₄ flow rate ratio) on the electrical, morphological, and optical characteristics of the films, with the objective to produce films with very large E_a and TCR, maintaining a moderated resistivity.

2. Experimental

We studied the effect of the chamber pressure and the SiH₄/GeH₄ flow ratio on the thermal sensitivity (TCR) and σ_{RT} of the resulting films. Two series of silicon- (Si-) germanium (Ge) films were deposited in an industrially compatible capacitively coupled PECVD reactor (from MVSystem Inc.) working at standard radio frequency of 13.56 MHz, with a RF power density of 86 mW/cm^2 , substrate temperature (T_s) of 200°C, and three different chamber pressure values (500 mTorr, 1000 mTorr, and 1200 mTorr).

The films of Series #1 were deposited with the flow rates of the precursors gases H₂ = 110 sccm, SiH₄ = 50 sccm, and GeH₄ = 50 sccm (resulting in SiH₄/GeH₄ = 1), while the films of Series #2 were deposited with the flow rates of the precursors gases H₂ = 110 sccm, SiH₄ = 90 sccm, and GeH₄ = 10 sccm (resulting in SiH₄/GeH₄ = 9). Notice that SiH₄ and GeH₄ used are diluted at 10% in H₂, and therefore the H₂ dilution is high ($H_2/(SiH_4 + GeH_4) = 20$).

The conditions used for the deposition of both series are summarized in Table 1. Both film series were deposited in various types of substrates for electrical, structural, and compositional characterization. The films depositions were performed simultaneously on corning glass 2974, corning glass 1737, corning glass 2974 with titanium metal contacts, and high resistivity silicon substrates.

Atomic force microscopy (AFM Nanosurf Easy Scan 2.3) was used to analyze the surface roughness of the films and thereby determine the possible presence of nanoclusters presented in the surface of the film. A large surface roughness is an indication of the presence of nanocrystals and even microcrystals in the bulk of the film [17].

Besides AFM characterization, Ultra High Resolution Field Emission Scanning Electron Microscopy (FE-SEM)

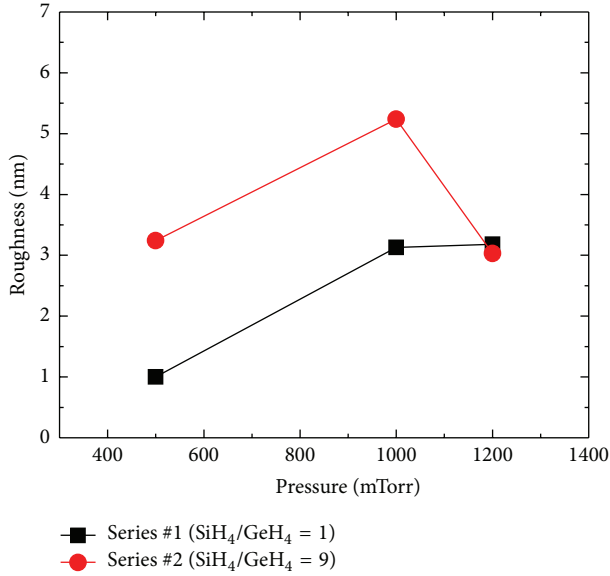


FIGURE 1: Average surface roughness ($\langle S_a \rangle$) versus chamber pressure in both series of pm-Si_xGe_y:H films.

and High Resolution Transmission Electron Microscopy (HRTEM) were used to analyze the films surface and the transversal structure of the films, in order to correlate the AFM results.

Ultraviolet-Visible (UV-Vis) transmittance measurements were performed in a Perkin-Elmer Lambda 3B spectrometer, in the range of 200–900 nm. Those measurements were performed in order to determine optical parameters of the deposited films, as the extinction coefficient (k) and the optical band gap (E_g).

The films also were analyzed on a Fourier Transform Infrared (FTIR) spectrophotometer (Bruker, Vector 22); the FTIR measurements were performed to analyze the molecular composition of the deposited films. For measurements of temperature dependence of the conductivity, the samples were placed in a thermostat with a pressure of 30 mTorr. A temperature controller (331 Temperature Controller, Lakeshore) was used to adjust the sample temperature. The temperature was varied from 300 K to 400 K, with steps of 10 K. At each temperature step, measurements were made to obtain the current-voltage characteristics ($I(U)$) of the films. With this characterization we obtained the values of E_a , TCR, and the electrical conductivity at room temperature (σ_{RT}).

3. Results and Discussion

Atomic Force Microscopy (AFM) measurements were performed in order to characterize the surface roughness ($\langle S_a \rangle$) of the two film series. Figure 1 shows the dependence of $\langle S_a \rangle$ with the deposition pressure in both films series and we can see that $\langle S_a \rangle$ is larger in the films deposited at pressures in the range of 1000 mTorr–1200 mTorr. The average surface roughness ($\langle S_a \rangle$) was obtained from a statistical analysis by scanning an area of $4 \mu\text{m} \times 4 \mu\text{m}$ on the surface of the films.

Figure 2 shows AFM 3D images of film surfaces corresponding to deposition pressures of 500 mTorr, 1000 mTorr, and 1200 mTorr, for both series. In the figure it is observed that the films deposited at pressure of 500 mTorr have a flatter surface (and lower roughness) than those films deposited at 1000 mTorr and 1200 mTorr. In this aspect, it is important to stress that the AFM technique is used for correlating the surface roughness to the presence of nanocrystals in the bulk. Large $\langle S_a \rangle$ is related to the presence of micro/nanocrystals embedded in the amorphous network. $\langle S_a \rangle$ of about 4 nm (and higher) is an indication of the presence of nanocrystals in the amorphous matrix [17]; however, this technique by itself is not enough for completely determining the structural composition of the bulk material.

Figure 3 shows an ultrahigh resolution FE-SEM image of the surface of a film (with $\langle S_a \rangle$ of about 5 nm); in the figure the presence of Si-Ge nanoclusters of sizes of about 50 nm is observed. In Figure 4, a HRTEM cross section view of the same film is shown, which was deposited on corning glass (a line was drawn for separating the film from the substrate). Several nanocrystals of size of about 2 nm–3 nm are marked and also an inset of the amplified image of 2 nanocrystals is included. The above analysis is in agreement with the AFM results and indicates the polymorphous nature of the film.

Figure 5 shows the deposition rate (V_d) as a function of the deposition pressure in both pm-Si_xGe_y:H film series. For Series #1, V_d was in the range 0.79 Å/s–2.72 Å/s, while, for Series #2, V_d was in the range 1 Å/s–1.5 Å/s. For Series #1, the largest V_d was obtained in the film deposited at chamber pressure of 1200 mTorr, while, for Series #2, the largest V_d was obtained in the film deposited at chamber pressure of 1000 mTorr. It has been observed that high deposition rates are associated with large crystalline fractions in microcrystalline films [18]. This is related to the fact that, at large V_d , the oxygen incorporation in the film is reduced, and the formation of nanocrystals in the plasma is promoted.

Ultraviolet-Visible (UV-Vis) transmittance measurements were performed for determining the band gap (E_g) of the pm-Si_xGe_y:H films. From the transmittance measurements, we obtained a data file that was processed using PUMA (*Pointwise Unconstrained Minimization Approach*). The software provides information of the characteristics of the films related to transmittance data measurements [19]. The important data obtained from PUMA is the extinction coefficient (k), which is converted to absorption coefficient (α) by

$$\alpha = \frac{4\pi k}{\lambda}. \quad (2)$$

Figure 6 shows the Tauc plots of both series of pm-Si_xGe_y:H films. We can determine E_g from the Tauc plot, where E_g is extracted by the extrapolation of the linear part of the plot towards the energy axis, and the interception indicates E_g of the film. In the films of Series #1, the E_g values are in the range 1.2 eV–1.28 eV, while, in the films of Series #2, the E_g values are in the range 1.37 eV–1.66 eV. The above is related to the Si and Ge content in the films; for Series #1, the Ge content is larger than in Series #2 (due to a

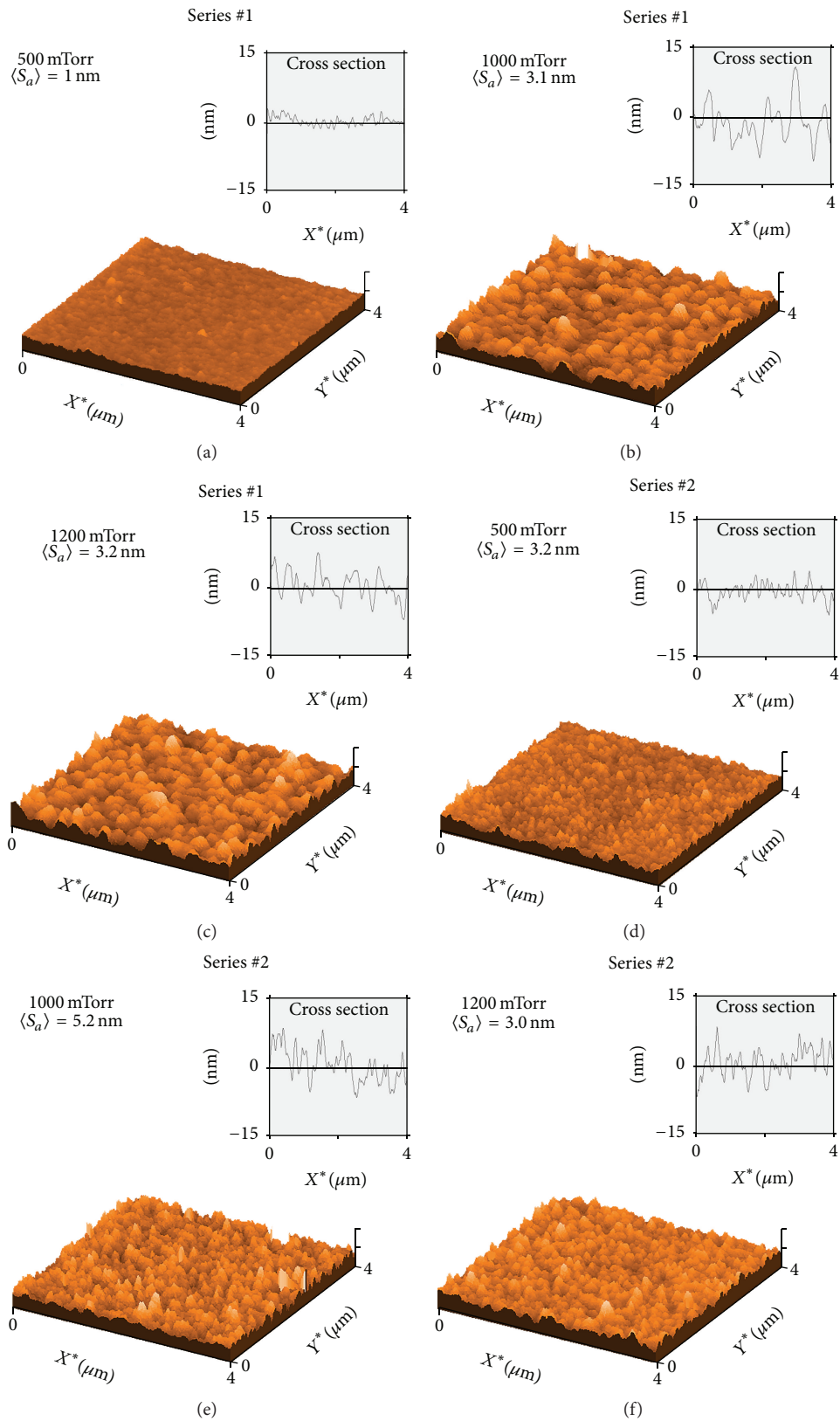


FIGURE 2: Surface analysis by AFM in pm-Si_xGe_y:H films, corresponding to (a) Series #1: 500 mTorr, (b) Series #1: 1000 mTorr, (c) Series #1: 1200 mTorr. (d) Series #2: 500 mTorr, (e) Series #2: 1000 mTorr, and (f) Series #2: 1200 mTorr.

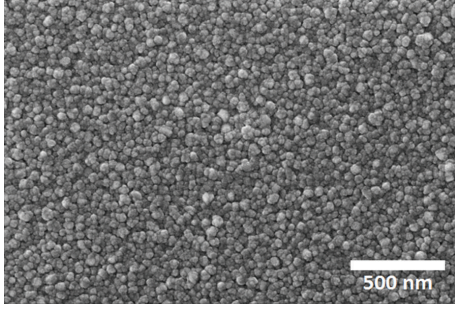


FIGURE 3: FE-SEM image of the surface of a pm-Si_xGe_y:H film, where the presence of nanoclusters of sizes of about 50 nm is observed.

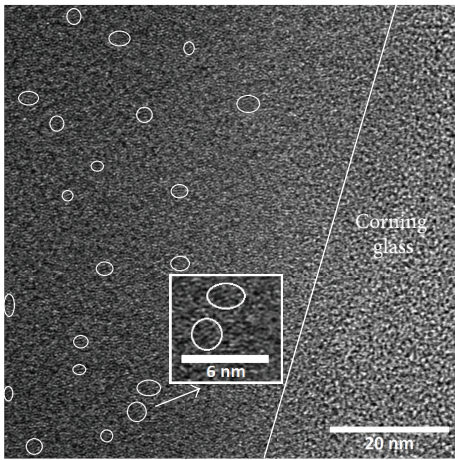


FIGURE 4: HRTEM cross section of a pm-Si_xGe_y:H film, where the presence of nanocrystals of sizes in the range of 2 nm-3 nm is observed. The inset shows an amplified image of 2 nanocrystals.

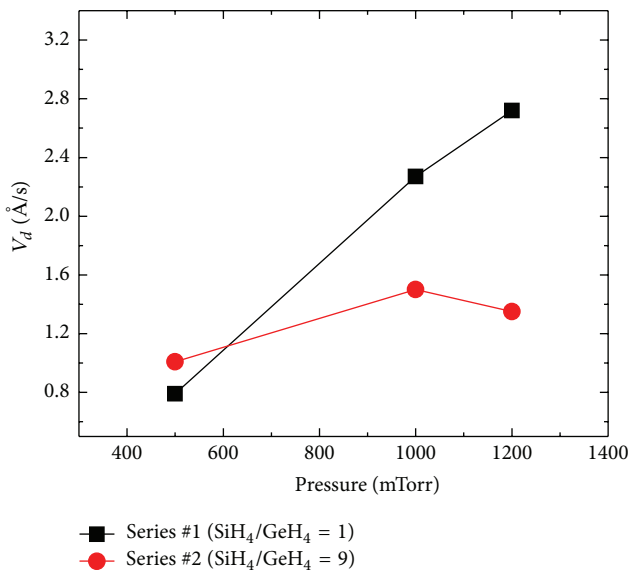


FIGURE 5: Deposition rate (V_d) in two series of deposited films. Series #1: SiH₄/GeH₄ = 1 and Series #2: SiH₄/GeH₄ = 9.

larger GeH₄ flow rate used for deposition). In this aspect, it has been reported for amorphous silicon-germanium films (a-SiGe:H) that a flow rate ratio of SiH₄/GeH₄ = 1 results in films with solid Ge content of about 85%, while a flow rate ratio of SiH₄/GeH₄ = 9 results in films with solid Ge content of about 45%; that analysis was performed using Secondary Ion Mass Spectroscopy (SIMS) [20].

The films were also analyzed with a FTIR spectrophotometer, which provides a spectrum of absorbance (or transmittance) in arbitrary units. In Figure 7, we observe the absorption spectra of both series of pm-Si_xGe_y:H films in the range from 400 cm⁻¹ to 2200 cm⁻¹. It is observed that both FTIR spectra are very similar; the most relevant peaks of both spectra are described below.

In the region between 500 cm⁻¹ and 700 cm⁻¹ there are two peaks centered at 560 cm⁻¹ and at 640 cm⁻¹, which are related to the Ge-H and Si-H bending vibration modes, respectively [21]. The peak near to 735 cm⁻¹ is related to Ge-O bonds, while the peak near to 885 cm⁻¹ is related to Si-H bonds. Near to 960 cm⁻¹ there is a peak related to Ge-O bonds and at 1100 cm⁻¹ there is a peak related to Si-O bonds. Finally near to 2000 cm⁻¹ there is a peak attributed to a Si-H stretching mode. All these peaks are present in both spectra.

The absorption peak near 1880 cm⁻¹ is attributed to the stretching vibration of Ge-H [20]; this peak is only present in the spectra of the films of Series #1, indicating a higher Ge content (than in the films of Series #2). The above is in agreement with the band gap analysis (Tauc plot) and the larger GeH₄ flow rate used for the deposition of Series #1.

In Figure 8, the dependence of σ_{RT} as a function of the deposition pressure in both series of pm-Si_xGe_y:H films is shown, and it is observed that σ_{RT} is larger in the films deposited at pressure in the range of 1000 mTorr–1200 mTorr. The above result is very interesting, since it indicates that deposition pressures, in that range, promote films with better structural order, due to the presence of nanocrystals, and those nanocrystals improve the electron mobility in the films (μ_e) and consequently σ_{RT} .

In Figure 8, it is also observed that the films of Series #1 (SiH₄/GeH₄ = 1) have larger σ_{RT} of nearly two orders of magnitude with respect to the films of Series #2 (SiH₄/GeH₄ = 9), which is related to the GeH₄ flow rate used for deposition (and higher Ge content).

We measured the temperature dependence of conductivity, $\sigma(T)$, in both series of pm-Si_xGe_y:H films, as is shown in Figure 9. We determined E_a from the Arrhenius curve $\ln(\text{conductivity})$ versus $1/KT^2$. E_a is related to the conductivity by (3), rewritten in (4), which express a line of the form $y = a + bx$. Then, E_a is obtained by fitting a straight line in the curve and calculating its slope as follows:

$$\sigma = \sigma_0 \exp\left(-\frac{E_a}{KT^2}\right), \quad (3)$$

$$\ln(\sigma) = \ln(\sigma_0) - \frac{E_a}{KT^2}. \quad (4)$$

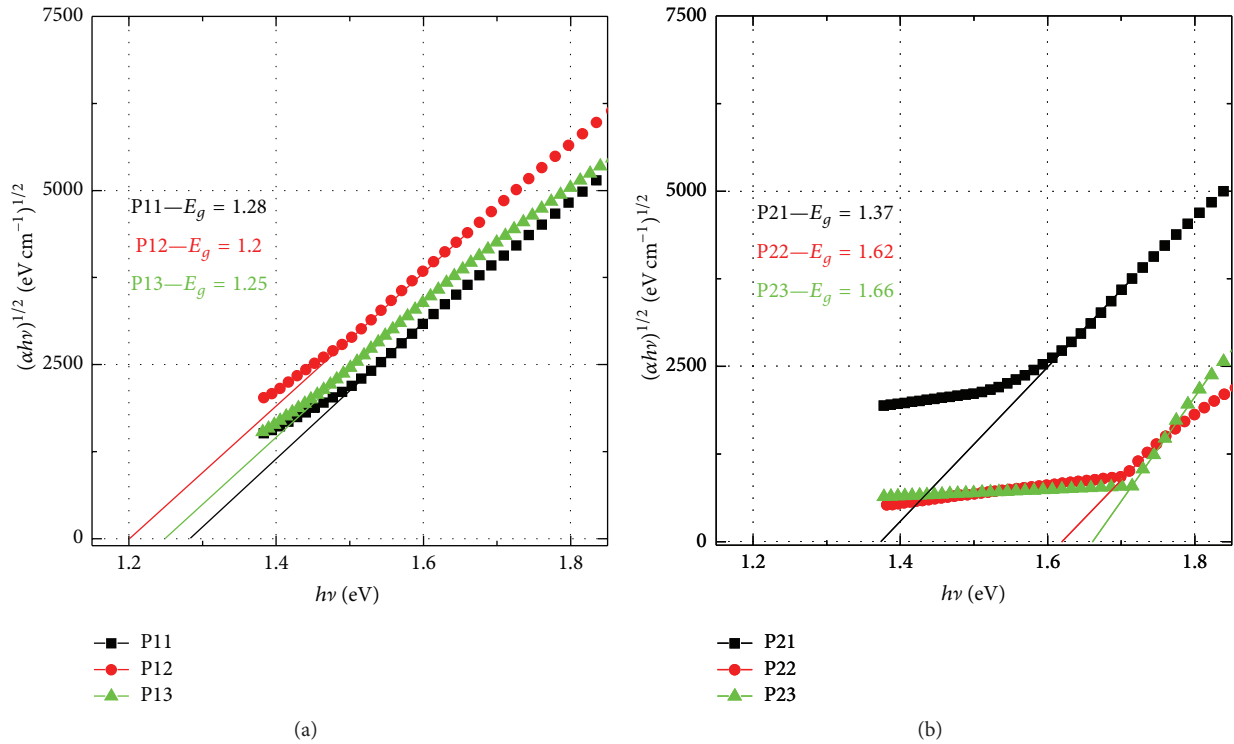


FIGURE 6: Tauc plot obtained from UV-Vis measurements for extracting the band gap (E_g) in two series of pm- $\text{Si}_x\text{Ge}_y\text{:H}$ films. (a) Series #1: $\text{SiH}_4/\text{GeH}_4 = 1$ and (b) Series #2: $\text{SiH}_4/\text{GeH}_4 = 9$.

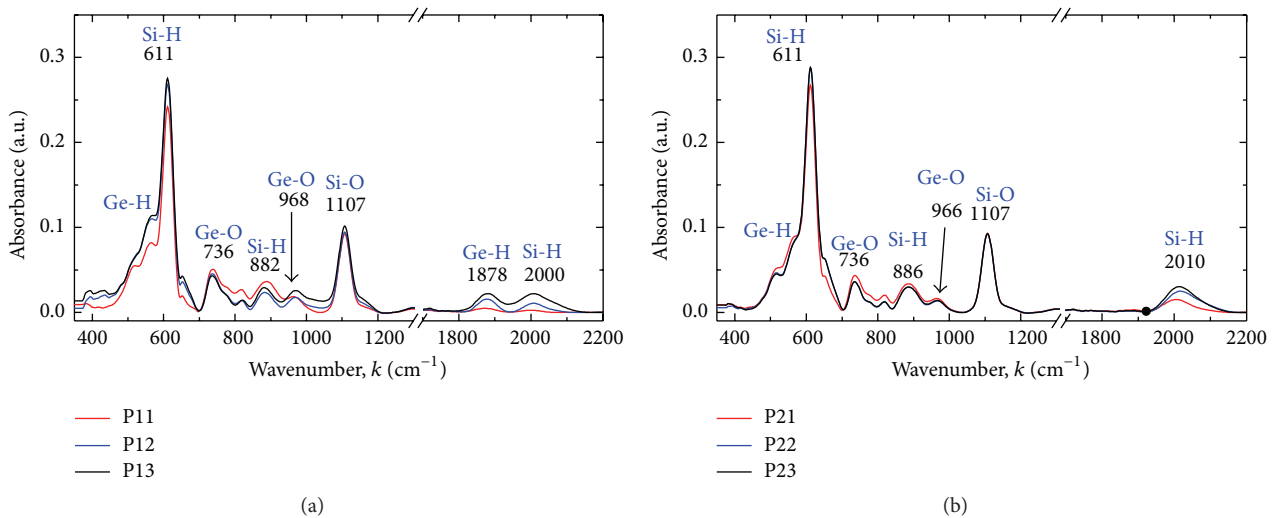


FIGURE 7: FTIR spectra of two series of pm- $\text{Si}_x\text{Ge}_y\text{:H}$ films. (a) Series #1: $\text{SiH}_4/\text{GeH}_4 = 1$ and (b) Series #2: $\text{SiH}_4/\text{GeH}_4 = 9$.

Figure 10 shows E_a and TCR as a function of the deposition pressure of both series of pm- $\text{Si}_x\text{Ge}_y\text{:H}$ films. For Series #1, the largest values obtained were $E_a = 0.45$ eV and $\text{TCR} = 5.9\%$ K^{-1} , while, for Series #2, the largest values obtained were $E_a = 0.62$ eV and $\text{TCR} = 7.9\%$ K^{-1} . The above is related to the fact that the films of Series #2 were deposited with larger SiH_4 flow rate (and consequently have larger Si content) than the films of series #1.

Finally, after studying the effect of the deposition pressure and the $\text{SiH}_4/\text{GeH}_4$ flow rate ratio on the characteristics of pm- $\text{Si}_x\text{Ge}_y\text{:H}$ films, we can conclude that large pressure values (1000 mTorr–1200 mTorr) are suitable for the formation of nanocrystals in the amorphous films, improving their stability and electrical characteristics. On the other hand, depending on the $\text{SiH}_4/\text{GeH}_4$ flow rate ratio used for the films deposition, it is possible to produce films with TCR values

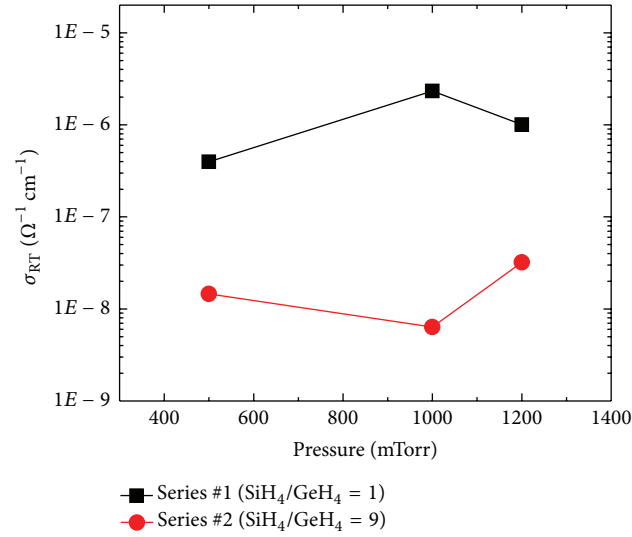


FIGURE 8: Room temperature conductivity (σ_{RT}) in two series of pm-Si_xGe_y:H deposited films. Series #1: SiH₄/GeH₄ = 1 and Series #2: SiH₄/GeH₄ = 9.

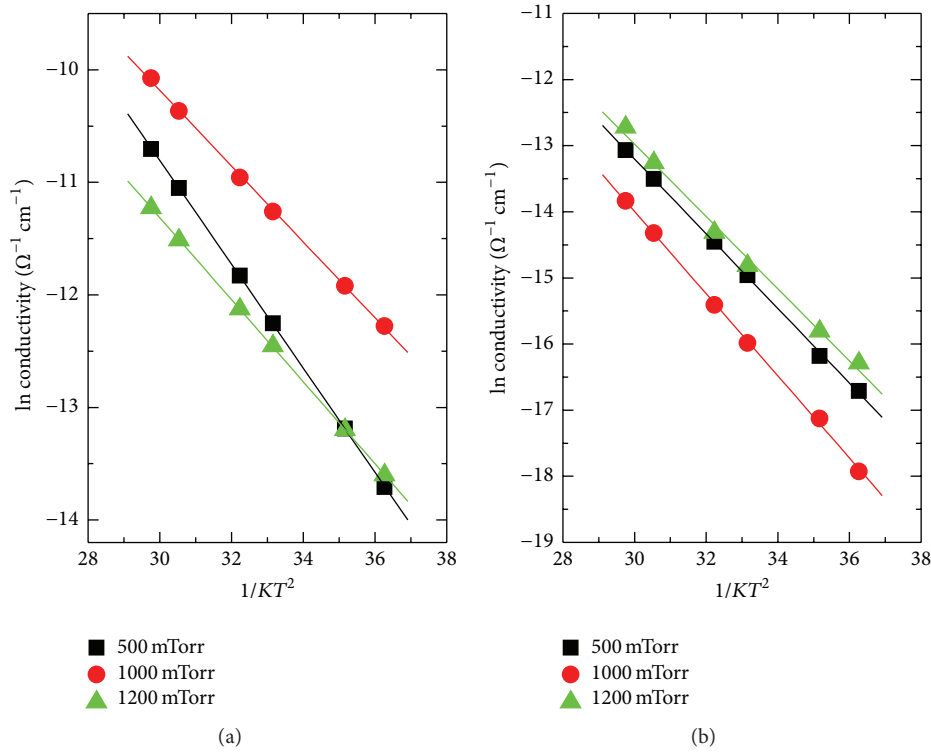


FIGURE 9: Temperature dependence of conductivity, $\sigma(T)$, in two series of pm-Si_xGe_y:H films. (a) Series #1: SiH₄/GeH₄ = 1 and (b) Series #2: SiH₄/GeH₄ = 9.

in the range of $4.3\% \text{K}^{-1}$ – $7.9\% \text{K}^{-1}$, with moderated σ_{RT} . The above characteristics are better than those of a-Si:H,B films used in commercial IRFPAs.

4. Conclusion

In this work, we have studied the deposition and characterization of amorphous silicon-germanium films with

embedded nanocrystals (pm-Si_xGe_y:H). We have studied the films characteristics under the influence of the deposition parameters as the chamber pressure and the precursor gases flow rate ratios (SiH₄/GeH₄). We have concluded that there is an optimum deposition pressure that promotes the formation of nanocrystals in the amorphous films (1000 mTorr–1200 mTorr) and impacts on the electrical characteristics and stability of the films. On the other hand, by varying the

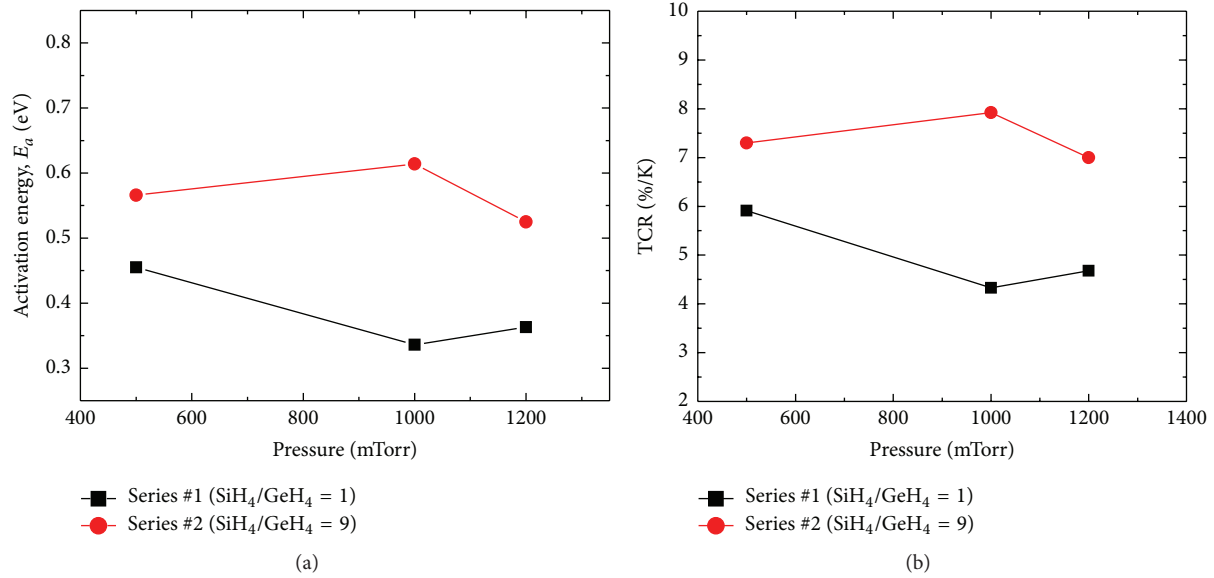


FIGURE 10: (a) Activation energy (E_a) as a function of the deposition pressure of two series of pm-Si_xGe_y:H films. (b) TCR as a function of the deposition pressure for two series of pm-Si_xGe_y films.

SiH₄/GeH₄ flow rate ratio, it is possible to vary σ_{RT} of the films (in about two orders of magnitude), as well the TCR in the range of 4.3% K⁻¹–7.9% K⁻¹.

Finally, we conclude that pm-Si_xGe_y:H films have advantages over amorphous thin films based on boron doped a-Si:H, due to their very large values of TCR with moderated values of σ_{RT} and, moreover, due to the possibility of tailoring those characteristics for specific requirements.

Conflict of Interests

The authors declare that there is no conflict of interests regarding the publication of this paper.

References

- [1] A. Rogalski, "Recent progress in infrared detector technologies," *Infrared Physics & Technology*, vol. 54, no. 3, pp. 136–154, 2011.
- [2] A. Rogalski, "History of infrared detectors," *Opto-electronics Review*, vol. 20, no. 3, pp. 279–308, 2012.
- [3] S. K. Ajmera, A. J. Syllaios, G. S. Tyber, M. F. Taylor, and R. E. Hollingsworth, "Amorphous silicon thin-films for uncooled infrared microbolometer sensors," in *Proceedings of the Infrared Technology and Applications XXXVI*, vol. 7660 of *Proceedings of SPIE*, p. 766012, Orlando, Fla, USA, May 2010.
- [4] B. Fièque, J. L. Tissot, C. Trouilleau, A. Crastes, and O. Legras, "Uncooled microbolometer detector: recent developments at Ulys," *Infrared Physics and Technology*, vol. 49, no. 3, pp. 187–191, 2007.
- [5] A. Heredia-J, A. Torres-J, A. Jaramillo-N, F. J. De la Hidalga-W, and M. Landa-V, "A boron doped amorphous silicon thin-film bolometer for long wavelength detection," in *Progress in Semiconductors II—Electronic and Optoelectronic Applications*, B. D. Weaver, M. O. Manares, C. C. Jagadish, and S. Zollner, Eds., vol. 744 of *MRS Proceedings*, Materials Research Society, 2002.
- [6] A. J. Syllaios, T. R. Schimert, R. W. Gooch, W. L. McCardel, B. A. Ritchey, and J. H. Tregilgas, "Amorphous silicon microbolometer technology," in *Proceedings of the Material Research Society Symposium*, R. W. Collins, H. M. Branz, S. Guha, H. Okamoto, and M. Stutzmann, Eds., vol. 609, San Francisco, Calif, USA, 2000, A14.4.1.
- [7] S. K. Ajmera, A. J. Syllaios, G. S. Tyber, M. F. Taylor, and R. E. Hollingsworth, "Amorphous silicon thin-films for uncooled infrared microbolometer sensors," in *Infrared Technology and Applications XXXVI*, vol. 7660 of *Proceedings of SPIE*, Orlando, Fla, USA, April 2010.
- [8] B. E. Cole, R. E. Higashi, and R. A. Wood, "Monolithic two-dimensional arrays of micromachined microstructures for infrared applications," *Proceedings of the IEEE*, vol. 86, no. 8, pp. 1679–1686, 1998.
- [9] A. H. Z. Ahmed and R. N. Tait, "Characterization of an amorphous Ge_xSi_{1-x}O_y microbolometer for thermal imaging applications," *IEEE Transactions on Electron Devices*, vol. 52, no. 8, pp. 1900–1906, 2005.
- [10] A. Jahanzeb, C. M. Travers, Z. Çelik-Butler, D. P. Butler, and S. G. Tan, "A semiconductor YBaCuO microbolometer for room temperature IR imaging," *IEEE Transactions on Electron Devices*, vol. 44, no. 10, pp. 1795–1801, 1997.
- [11] B. Wang, J. Lai, H. Li, H. Hu, and S. Chen, "Nanostructured vanadium oxide thin film with high TCR at room temperature for microbolometer," *Infrared Physics and Technology*, vol. 57, pp. 8–13, 2013.
- [12] W. Bronner, J. P. Kleider, R. Brüggemann, P. Roca i Cabarrocas, D. Mencaraglia, and M. Mehring, "Comparison of transport and defects properties in hydrogenated polymorphous and amorphous silicon," *Journal of Non-Crystalline Solids*, vol. 299–302, no. 1, pp. 551–555, 2002.
- [13] P. Roca i Cabarrocas, A. Fontcuberta i Morral, and Y. Poissant, "Growth and optoelectronic properties of polymorphous silicon thin films," *Thin Solid Films*, vol. 403–404, pp. 39–46, 2002.

- [14] M. Meaudre, R. Meaudre, R. Butté et al., “Midgap density of states in hydrogenated polymorphous silicon,” *Journal of Applied Physics*, vol. 86, no. 2, pp. 946–950, 1999.
- [15] L. Boufendi, M. Ch. Jouanny, E. Kovacevic, J. Berndt, and M. Mikikian, “Dusty plasma for nanotechnology,” *Journal of Physics D: Applied Physics*, vol. 44, no. 17, Article ID 174035, 2011.
- [16] M. Moreno, A. Torres, C. Calleja et al., “Exploring the infrared-sensing properties of polymorphous silicon-germanium (pm-SixGe_{1-x}:H) thin films,” *Canadian Journal of Physics*, vol. 92, no. 7-8, pp. 565–569, 2014.
- [17] A. Shaha, E. Vallat-Sauvain, P. Torres et al., “Intrinsic microcrystalline silicon ($\mu\text{c-Si:H}$) deposited by VHF-GD (very high frequency-glow discharge): a new material for photovoltaics and optoelectronics,” *Materials Science and Engineering B*, vol. 69-70, pp. 219–226, 2000.
- [18] M. Moreno, R. Boubekri, and P. Roca i Cabarrocas, “Study of the effects of different fractions of large grains of $\mu\text{c-Si:H:F}$ films on the infrared absorption on thin film solar cells,” *Solar Energy Materials & Solar Cells*, vol. 100, pp. 16–20, 2012.
- [19] E. G. Birgin, I. Chambouleyron, and J. M. Martínez, “Estimation of optical constants of thin films using unconstrained optimization,” *Journal of Computational Physics*, vol. 151, pp. 862–880, 1999.
- [20] A. Kosarev, A. Torres, Y. Hernandez et al., “Silicon-germanium films deposited by low-frequency plasma-enhanced chemical vapor deposition: effect of H₂ and Ar dilution,” *Journal of Materials Research*, vol. 21, no. 1, pp. 88–104, 2006.
- [21] X. Liao, H. Povolny, P. Agarwal, and X. Deng, “Raman and IR study of narrow bandgap a-SiGe and $\mu\text{c-SiGe}$ films deposited using different hydrogen dilution,” in *Proceedings of the Conference Record of the 29th IEEE Photovoltaic Specialists Conference*, pp. 1150–1153, May 2002.

Research Article

Nanosensing Backed by the Uncertainty Principle

I. Filikhin, A. Karoui, and B. Vlahovic

Department of Physics, North Carolina Central University, 1801 Fayetteville Street, Durham, NC 27707, USA

Correspondence should be addressed to I. Filikhin; ifilikhin@nccu.edu

Received 4 December 2015; Accepted 5 January 2016

Academic Editor: Wen Zeng

Copyright © 2016 I. Filikhin et al. This is an open access article distributed under the Creative Commons Attribution License, which permits unrestricted use, distribution, and reproduction in any medium, provided the original work is properly cited.

Possibility for a novel type of sensors for detecting nanosized substances (e.g., macromolecules or molecule clusters) through their effects on electron tunneling in a double nanoscale semiconductor heterostructure is discussed. We studied spectral distributions of localized/delocalized states of a single electron in a double quantum well (DQW) with relation to slight asymmetry perturbations. The asymmetry was modeled by modification of the dot shape and the confinement potential. Electron energy uncertainty is restricted by the differences between energy levels within the spectra of separated QWs. Hence, we established a direct relationship between the uncertainty of electron localization and the energy uncertainty. We have shown in various instances that a small violation of symmetry drastically affects the electron localization. These phenomena can be utilized to devise new sensing functionalities. The charge transport in such sensors is highly sensitive to minuscule symmetry violation caused by the detected substance. The detection of the electron localization constitutes the sensor signal.

1. Introduction

A new generation of nanosensors is underway and is expected to revolutionize modern engineering fields, including bio-engineering and drug delivery systems in nanomedicine, to name a few. Semiconductor heterostructures, such as quantum dots and rings, are of high interest for the development of these nanosensors, as well as many other predicted nanodevices. Of particular importance is the electron tunneling that occurs between the nanosized elements of such devices. Double quantum systems facilitate the study of tunneling related to barrier penetration effects in double well potentials [1]. When the elements of a quantum system get coupled, the energy barrier splitting of degenerate levels occurs, due to their common wave function. As a result, two nearly degenerate eigenstates are formed, which are a linear combination of the wave functions of the electron in isolated dots. Likewise, electron spectrum of double quantum dots formed by a set of quasidoublets is well described within the one-dimensional formalism given in [1] for double quantum wells. An example of theoretical analysis for double quantum dots has been presented in [2, 3]. These are supported by experimental studies of different aspects (spin effects, coupling distance, electron-phonon coupling,

hybrid nanostructures, etc.) which are tightly connected to, and controlled by, charge tunneling in the DQDs. These aspects are extensively developing; see, for instance, [4–6]. Recently, we have reported in [7] that single electron localized/delocalized states and the tunneling in DQWs and DQDs are highly sensitive to the violation of reflection symmetry of the dots. It should be noted that this aspect is relevant to quantum dot reality, as fabrication technologies produce dot arrays with imperfect shape and distributions. These imperfections inherently induce a chaotic behavior in the QDs. It has been demonstrated that chaos strongly influences charge transport and other properties of QDs [8, 9]. The relevance of electron tunneling and chaos in real QD arrays is obvious for next generation nanodevices, for instance, future single molecule nanosensors, quantum computing devices, and advanced solar cells, to name a few.

In the present work we study the spectral distribution of electron localized/delocalized states and tunneling in DQWs. The average coordinate is used to characterize the localization of a single electron. We discuss the case of identical QWs constituting a DQW, as an example, when the uncertainty principle is manifested. Uncertainty of electron localization occurs when the difference of electron energies in the left and right QW is very small; that is the case of almost identical

QWs. The symmetry violation caused by differences in the geometry and/or the confinement potentials in left and right QWs is thoroughly discussed.

2. Effective Model for InAs/GaAs Quantum Dots

We consider quantum dots composed of InGaAs on a GaAs substrate. The fabrication of such kind of quantum dots is reported in [10, 11], for example. In practice, QDs have average lateral size and height of 41 and 1.6 nm, respectively, with variations within 23% and 28%, respectively. Hence, in our model the heterostructured QD dimensions were varied within these limits. The QDs were laterally distributed (two-dimensional array) for minimizing the computational recourses. The underlying quantum problem is modeled utilizing the \mathbf{kp} -perturbation single subband approach, which is mathematically formulated by the Schrödinger equation as follows [12]:

$$\left(\widehat{H}_{\mathbf{kp}} + V_c(r) + V_s(r)\right)\Psi(r) = E\Psi(r). \quad (1)$$

Here $\widehat{H}_{\mathbf{kp}}$ is the single band \mathbf{kp} -Hamiltonian operator $\widehat{H}_{\mathbf{kp}} = -\nabla(\hbar^2/2m^*)\nabla$, $m^* = m^*(\mathbf{r})$ is the electron effective mass, which depends on the position of the electron, and $V_c(\mathbf{r})$ is the band gap potential, which is null inside the QW, $V_c(\mathbf{r}) = 0$, and constant, equal to V_c , outside the QW. The value of V_c is defined by the conduction band offset for the bulk. The band gap potential for the conduction band is chosen as $V_c = 0.594$ eV [13]. The magnitude of V_c is calculated as $V_c = k(E_{g,2} - E_{g,1})$, where $E_{g,1}$ and $E_{g,2}$ are the band gaps of QD and the substrate, respectively. The coefficient k can be different for the conduction and valence bands. Here, the dimensionless constant k values are taken from [14]. For the conduction band $k(\text{CB}) = 0.54$, and for the valence band $k(\text{VB}) = 0.46$. Using experimental values $E_{g,1} = 0.42$ eV and $E_{g,2} = 1.52$ eV, $V_c = 0.594$ eV was obtained for the conduction band. The bulk effective masses of InAs and GaAs are $m_1^* = 0.024 m_0$ and $m_2^* = 0.067 m_0$, respectively [15], where m_0 is the free electron mass. $V_s(\mathbf{r})$ is the effective potential simulating the strain effect; it is attractive and acts inside the QW. The magnitude of the potential can be chosen [12] to reproduce experimental data. In presented work, the magnitude of V_s for the conduction band is 0.21 eV. With this value, the results of the 8th band \mathbf{kp} -calculations of [16] are well reproduced [17].

3. Wave Function of Two Level System

Single electron spectrum of a two-level system is defined as a set of quasidoublets [1]. The one-dimensional wave functions of each quasidoublet can be expressed as follows [1]:

$$\begin{aligned} \Psi_+ &= \cos\left(\frac{\Theta}{2}\right)\psi_1 + \sin\left(\frac{\Theta}{2}\right)\psi_2, \\ \Psi_- &= -\sin\left(\frac{\Theta}{2}\right)\psi_1 + \cos\left(\frac{\Theta}{2}\right)\psi_2, \end{aligned} \quad (2)$$

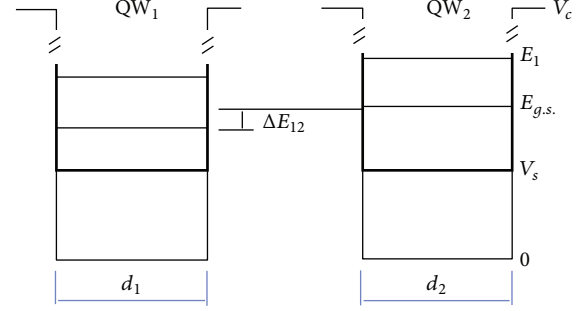


FIGURE 1: Band gap model for one-dimensional DQW. d_1 and d_2 are widths of the QWs, $d_1 \neq d_2$. ΔE_{12} is the difference between homolog energy levels pertaining to left and right QWs, considered separated. The notations are corresponding to the theoretical model described above. $E_{g,s}$ is ground state energy of an electron.

where

$$\tan(\Theta) = \frac{2W}{\Delta E_{12}} \quad \text{with } 0 \leq \Theta \leq \pi. \quad (3)$$

Relation (2) shows that the wave function decomposed onto the basis set (ψ_1, ψ_2) . The parameter W is a coupling coefficient of the quantum system elements. It depends on the wave function overlap for the “unperturbed states” ψ_1 and ψ_2 of the left and right quantum dots considered to be separated. $\Delta E_{12} = E_1 - E_2$ is energy difference of separated QWs. It is defined for each energy level in the spectrum. An illustration of the band gap model with the effective potential is presented in Figure 1.

In (2), we neglected the phase shift as it does not play a role in the present case. The energy difference ΔE_{12} coincides with the quasidoublet splitting $\Delta E = E_+ - E_-$ for separated QWs.

To evaluate the electron localization, we analyze the single electron average coordinate $\langle x \rangle$, calculated as $\langle x \rangle_i = \langle i|x|i \rangle$ for $i = 1, 2$, which are associated, respectively, with QW $_i$, $i = 1, 2$, considered to be separated. The x -coordinate origin is the midpoint of the two QWs. The average coordinate $\langle x \rangle_+$ ($\langle x \rangle_-$) of the electron in Ψ_+ state (Ψ_-) can be written as

$$\begin{aligned} \langle x \rangle_+ &= -\cos^2\left(\frac{\Theta}{2}\right)\langle x \rangle_1 + \sin^2\left(\frac{\Theta}{2}\right)\langle x \rangle_2 \\ &\quad + 2\sin\left(\frac{\Theta}{2}\right)\cos\left(\frac{\Theta}{2}\right)\langle x \rangle_{12}, \\ \langle x \rangle_- &= -\sin^2\left(\frac{\Theta}{2}\right)\langle x \rangle_1 + \cos^2\left(\frac{\Theta}{2}\right)\langle x \rangle_2 \\ &\quad - 2\sin\left(\frac{\Theta}{2}\right)\cos\left(\frac{\Theta}{2}\right)\langle x \rangle_{12} \end{aligned} \quad (4)$$

for corresponding levels of a quasidoublet spectrum (i.e., the DQW spectrum). Due to the dependence on Θ , single electron spectrum is constituted of three parts: delocalized states ($\Theta \approx \pi/2$), localized states ($\Theta \approx 0$), and states with different probability for localizations in left and right QWs. The equation $\Theta = \arctg(W/\Delta E_{12})$, derived from

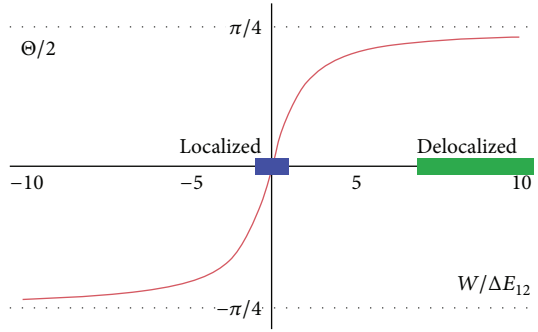


FIGURE 2: Relation between the parameter Θ and the QW coupling coefficient in a DQW. The ranges for localized and delocalized states of the electron in DQW are shown.

(3), provides the relationship between Θ parameter and localization/delocalization likelihood of electron in DQW. Figure 2 illustrates that relationship and shows the domain ranges where location and delocalization occur.

According to relation (3), the electron localization in DQW is extremely sensitive to small violations of DQW symmetry, when $\Delta E_{12} \approx 0$. By differentiation of relation (3), one can obtain an estimate of the sensitivity of the terms in (2) to small variations of the energy difference ΔE_{12} :

$$\delta\left(\frac{\Theta}{2}\right) \sim \frac{W}{(\Delta E_{12})^2} \delta(\Delta E_{12}). \quad (5)$$

Due to the square in the denominator, small variations of ΔE_{12} cause large variations of the prefactors in relations (2) and (4). Hence, for weakly coupled QWs the uncertainty of single electron energy is minimal, while the uncertainty for electron localization is large. This fact is in line with the uncertainty principle.

4. Numerical Results

4.1. Identical QWs. The experimentally demonstrated circular disc shaped InAs/GaAs quantum dots constitute double quantum wells. We consider in this section identical quantum wells, with equal radii $R_1 = R_2 = 33$ nm. An example of experimental realization of this system is reported in [10, 11], where the grown QDs are highly symmetric and free from any lateral elongation.

The electron average coordinate $\langle x \rangle$ in this DQW system has been calculated for each level of the single electron spectrum, according to the above described model. The results are presented in Figure 3. In the DQW quasidoublet spectrum, the spectral distribution appears symmetric relative to the $\langle x \rangle = 0$ axis, due to relation (4). Furthermore, the energy spectrum of single electron can be sorted according to electron localization probability, as a set of localized states (in the left QW or right QW, for which $\langle x \rangle = \pm|\langle x \rangle|$), delocalized states (i.e., $\langle x \rangle \sim 0$), and states with different probabilities in left and right QWs. Competition between values of ΔE_{12} and the coupling coefficient W in (2)-(3) defines the type of electron localization in the system. For

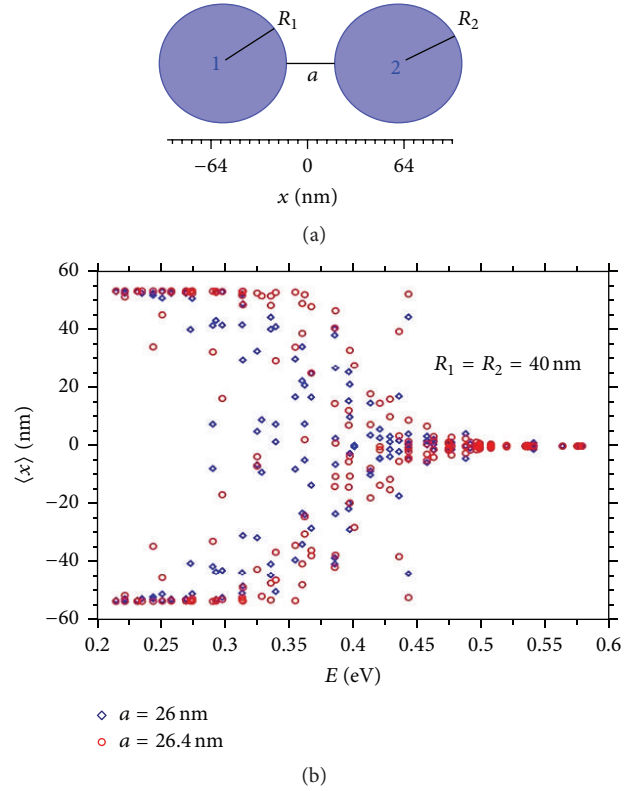


FIGURE 3: Effects of the interdot distance, a , on the spectrum of a DQW made of symmetric circular InAs/GaAs dots ($R_1 = R_2 = 40$ nm). (a) Schematic representation of geometry parameters of DQW. (b) The average coordinate $\langle x \rangle$ calculated for each level of single electron DQW spectrum.

the ideal case of identical QWs, that is, when $\Delta E_{12} = 0$, the wave functions of delocalized states are expressed as $\Psi_+ = (\psi_1 + \psi_2)/\sqrt{2}$, and $\Psi_- = (-\psi_1 + \psi_2)/\sqrt{2}$. It should be noted that numerical discretization of the Schrodinger equation on a finite mesh leads to significant computational errors. Thus the ideally symmetric system cannot be solved numerically, and computer modeling rather leads to solutions pertaining to dissymmetric QWs. As can be seen in Figure 3, there are strong deviations of the spectral distribution for the average coordinate $\langle x \rangle$, calculated for two interdot distances which differ for small values of a . This instability is stronger for the intermediate region of the spectrum, where the levels with different probability for localization in left and right QWs are found.

To evaluate the accuracy of the calculations we applied different meshes. Figure 4 shows the sensitivity of spectral distribution of $\langle x \rangle$ to tuning the discretization meshes. The results are unstable relative to mesh variations. In particular, the calculation for states with different localization probability (in left and right QWs) is unstable due to the uncertainty of ΔE_{12} (artificially due to computational errors) and relation (3). One can use the quasidoublet splitting energy $\Delta E = E_+ - E_-$ at the ground state, as a reference, to evaluate the effect of discretization. Figure 4 shows $\langle x \rangle$ for three meshes and the inset gives the resulting ΔE , energy splitting of the

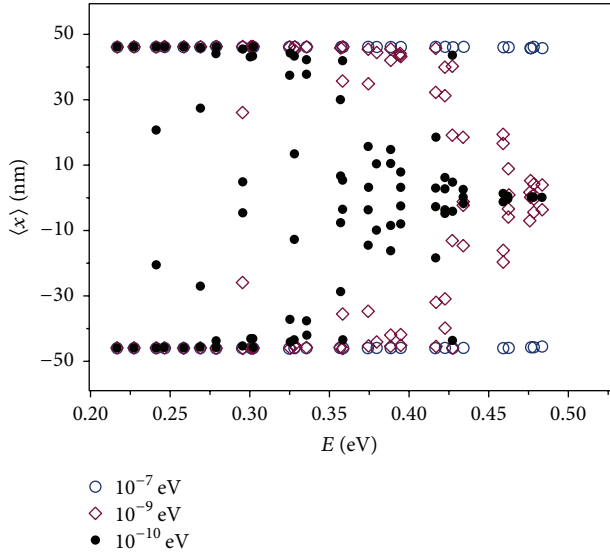


FIGURE 4: Spectral distributions for the average coordinate $\langle x \rangle$ for a circular DQW. The symbols correspond to discretization of the Schrödinger equation on various numerical meshes. The meshes differ by the elements minimum size. The energy splitting (ΔE) of the quasidoublet of the ground state for each discretization of a mesh is given in the inset. The finer mesh corresponds to smaller ΔE . Interdot distance a is kept the same and equal to 26 nm.

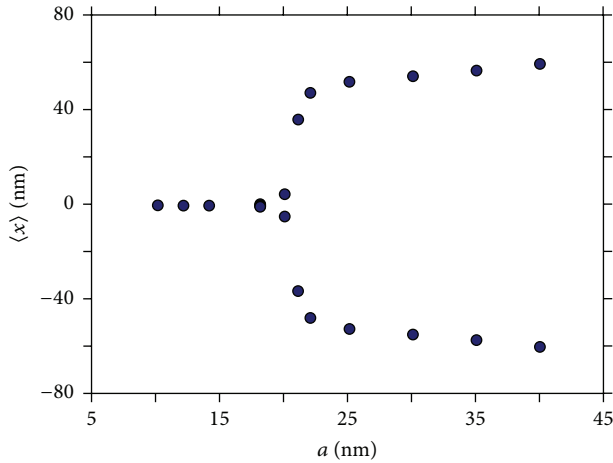


FIGURE 5: Average coordinate $\langle x \rangle$ of the electron in ground state of symmetric circle shaped DQW ($R_1 = R_2 = 40$ nm) as a function of the interdot distance. The numerical discretization for the used mesh leads to an energy difference $\Delta E \sim 10^{-7}$ eV of the quasidoublet ground state.

quasidoublet for the ground state. It appears that the finer mesh gives the smaller ΔE . Hence, we assume that the results of calculations presented below for identical QW have a numerical error of about 10^{-7} eV.

Visualization of the localized-delocalized states dynamics in the InAs/GaAs DQW is given in Figure 5, where the average coordinate $\langle x \rangle$ is presented as a function of the interdot distance a (see also [7]). When the distance between QWs is large, the electron is localized in one of the QWs; in

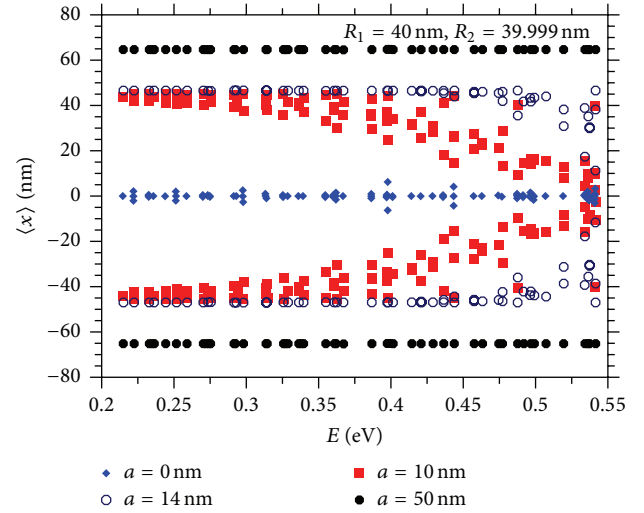


FIGURE 6: Average coordinate, $\langle x \rangle$, for single electron spectrum in the case of asymmetric DQW versus interdot distance a . The asymmetry parameter is maintained constant and equal to $\xi = 0.99975$ ($\xi = R_2/R_1 = 39.999/40$).

that case the parameter $\Theta \approx 0$. When the interdot distance decreases, the electron tunneling increases and the wave function spreads over the whole double system, $0 \leq \Theta \leq \pi$. All states become delocalized for interdot distances less than 17 nm. The localized states occur for interdot distances larger than 25 nm.

Additionally, as can be seen in (5), the electron localization demonstrates extreme sensitivity to small variations of QW shapes, which also violate the DQW left-right symmetry. Dissymmetry of dot shape will be discussed in the following section.

4.2. Asymmetric DQW. Let us consider two circular QWs that are nonidentical. The asymmetry parameter for the DQW is defined as $\xi = R_2/R_1$. We chose very small asymmetry (e.g., $\xi \sim 0.99975 = 39.999/40$), as nearly identical QWs lead to relevant quantum effects and mimic the reality of QW arrays. In this study, we vary the interdot distance. The calculation results are presented in Figure 6, where the average coordinate $\langle x \rangle$ along the single electron spectrum is shown for four interdot distances. The interdot distance is gradually decreased from large distances, when the QWs are separated, to contacting QWs.

Comparing with the previously discussed identical DQWs, for asymmetric DQW, the interdot distance that causes the quantum states to become delocalized, over the entire spectrum, is smaller. For example, when $\xi = 0.99975$, such interdot distance is less than 7 nm, whereas it is equal to 17 nm for identical QWs.

It has been previously found [7] that extremely small difference in QW radii in a DQW (ratio $\xi = R_2/R_1$ slightly smaller than 1) drastically affects the spectral distribution of localized/delocalized states. Such violation of DQW shape symmetry defines small variation of ΔE_{12} , according to (3). Also, according to (4), small change of ΔE_{12} can induce

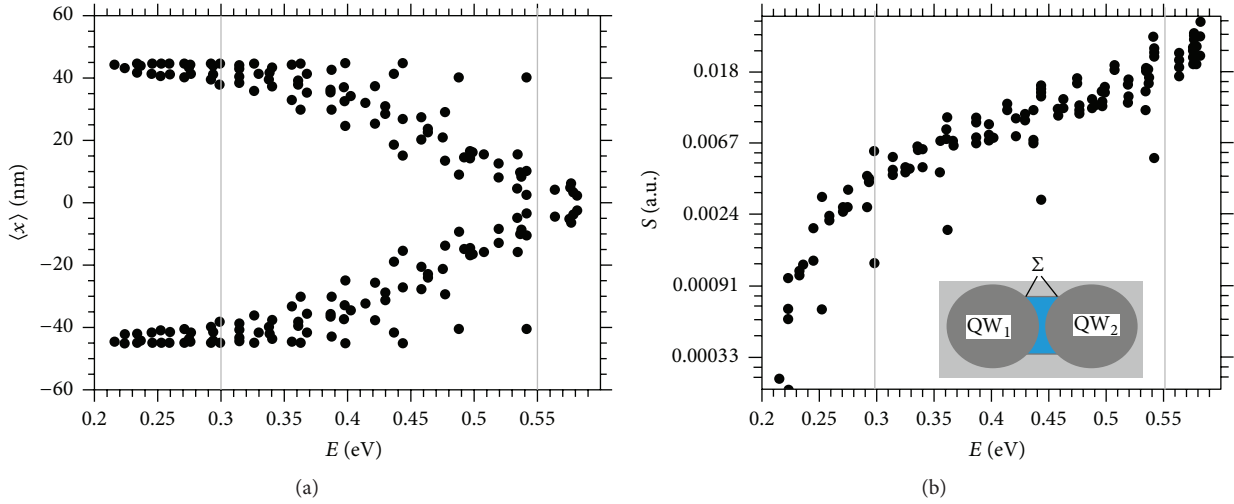


FIGURE 7: (a) Spectral distribution of $\langle x \rangle$ for asymmetric DQW with $a = 10$ nm. The asymmetry parameter $\xi = R_2/R_1 = 39.999/40$ ($\xi = 0.999975$). The vertical lines divide the spectrum in three predominant parts: delocalized, transitional, and localized states. (b) Overlap integral S plotted along electron spectrum; the integration area Σ is shown in the inset.

significant changes of the coefficients of linear combination (2), thereby drastically changing the wave functions.

Typical picture for the spectral distribution of average coordinate $\langle x \rangle$ is shown in Figure 7(a), which was obtained for interdot distance $a = 10$ nm. The spectrum readily divided in localized states (upper spectral levels), states with different localization probability in left and right QW (transitional states), and delocalized states (low-lying states). The relations in (4) explain the spectral distribution of the average coordinate shown in Figure 7(a).

The matrix element W (which is also proportional to the quasidoublet energy splitting ΔE [18]) can be described using the following relation: $W \sim S$, where S is the overlap integral, approximated by $S = \int_{\Sigma} \psi^2(x, y) dx dy$, with the integration domain Σ being the area between the QWs; see inset in Figure 7(b). In the overlap integral, the wave functions $\psi(x, y)$ are normalized. The distribution of S along the spectrum is shown in Figure 7(b). The magnitude of the wave function overlap depends on both the distance between quantum objects and the spreading of the wave function over the QWs. Generally, the matrix elements W are larger for upper levels in comparison with those for low-lying levels. This is due to the fact that the upper levels of the spectrum have broader wave functions. The large values of W are associated with the large Θ values (i.e., $\Theta \leq \pi$) for such levels; in such cases, the electron takes a localized state, as can be seen in Figure 7(a).

The symmetry breaking in DQW can be also made by variations of the confinement strength in one of the QWs. In Figure 8, the results of such variations are presented for QWs with identical shape. The magnitude of the DQW asymmetry is increased by increasing the potential from $V_s = 0.21$ eV to 0.21005 eV, to 0.2101 eV, and to 0.211 eV. With the last value of V_s all states in the spectrum become localized. Note that initially the states were delocalized, due to the chosen short interdot distance ($a = 4$ nm). Again we see

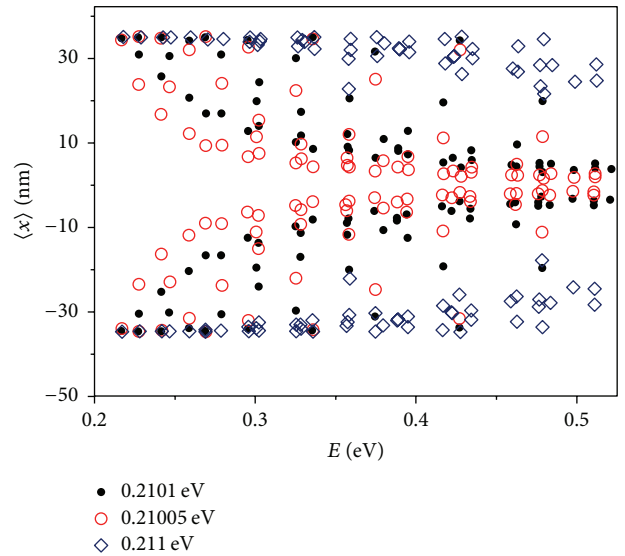


FIGURE 8: Single electron average coordinate $\langle x \rangle$ along the energy spectrum for asymmetric DQW under different confinement potentials V_s in left QW (shown in the inset). The potential in right QW is not changed ($V_s = 0.21$ eV). The interdot distance is kept constant and equal to 4 nm.

that such quick transformation of electron localization (due to symmetry breaking) is possible under the condition of minimal uncertainty of electron energy. The pace and the sensitivity of the transformation are high for almost identical QWs.

One more illustration of symmetry breaking effect is given in Figure 9, where the DQW asymmetry is made by a small cut of the right quantum well (QW_2). The average coordinate $\langle x \rangle$ plotted along electron spectrum for different depths of the cut ($d_0 = 0.5$ nm and 1 nm) is given in

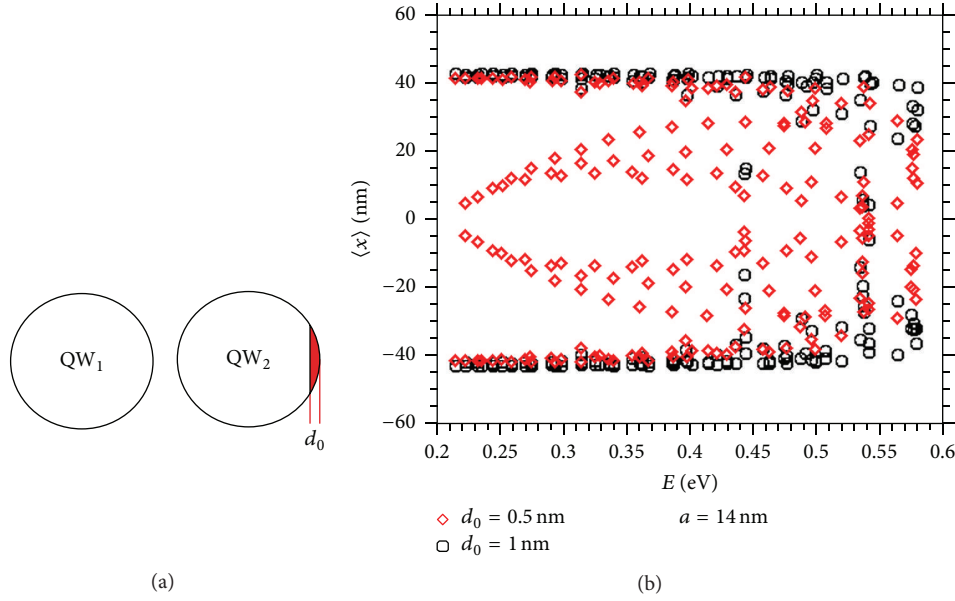


FIGURE 9: (a) Circle shaped DQW exhibiting an asymmetry generated by truncating the right quantum well (QW₂). (b) Electron average position $\langle x \rangle$ plotted along electron spectrum of the asymmetric DQWs ($R_1 = R_2 = 40$ nm and $a = 14$ nm) for two different cut depths d_0 , inducing well contrasted symmetry violation within the DQW.

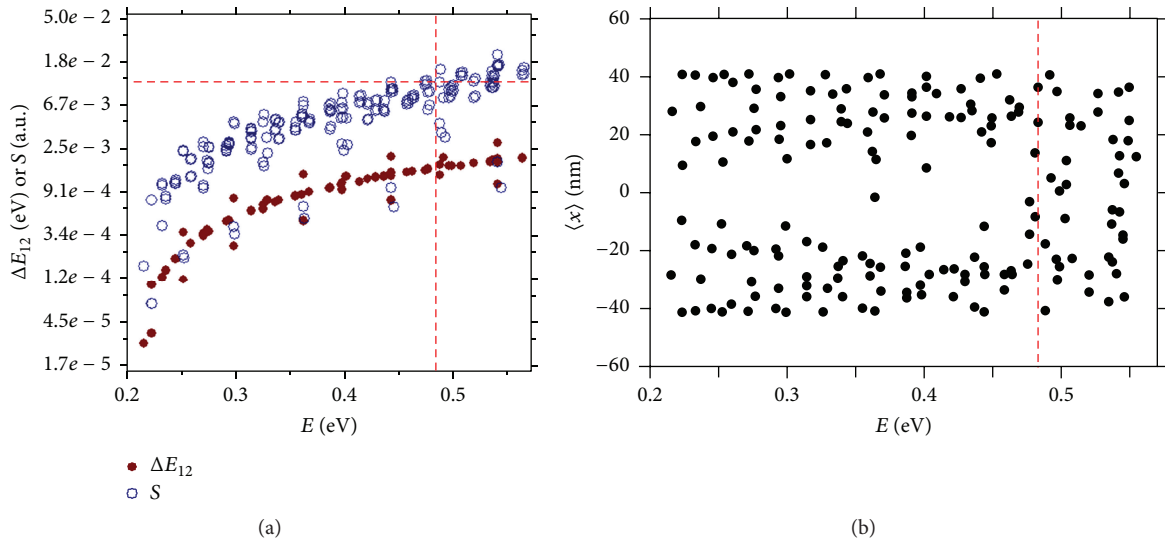


FIGURE 10: (a) Energy differences ΔE_{12} (solid circles) and overlap integrals S (open circles). (b) Average coordinate $\langle x \rangle$ along single electron spectrum for the asymmetric DQW for asymmetry parameter $\xi = R_{2y}/R_{2x}$, $\xi = 39.75/40 = 0.99375$. The dashed lines divide ΔE_{12} and S ranges in regions of mainly localized and mainly delocalized states.

Figure 9(b). The interpretation of this data can be done by noticing that the decrease of the asymmetry (through shape variation or through decrease of energy uncertainty limits) leads to increasing uncertainty of electron position in the system. For larger depth of the cut, the states of the DQW are mainly localized states.

An additional illustration of the symmetry breaking effect is presented in Figures 10 and 11, where we compare the tunneling for two cases: small ($\xi = 0.99375$) and relatively large ($\xi = 0.875$) asymmetry of the DQW with fixed interdot distance. This is composed of a QW circular in shape with a

radius $R_1 = 40$ nm and an elliptical QW with the major axis along the x -axis ($R_{2y} \leq R_{2x}$). The values ΔE_{12} and S are shown in Figure 10(a). Again, the number of the delocalized levels appears larger for the case of small asymmetry. The “random” distribution of delocalized states in the spectrum relates to the distribution of the matrix element W is reflected here in the distribution of the S integral. The S parameter varies up to two degrees for different spectral levels. The levels with minimal S directly relate to delocalized states of the spectrum, as visible in Figure 10(b). One can note that if the value of S is relatively large and ΔE_{12} is relatively small, the corresponding state

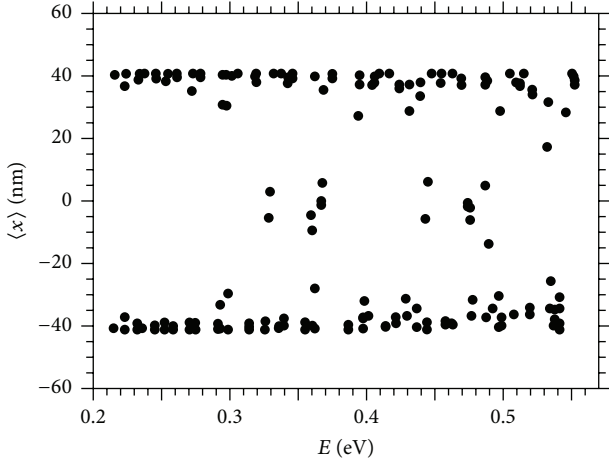


FIGURE 11: Average coordinate $\langle x \rangle$ along single electron spectrum for the asymmetric circular/elliptic DQW for asymmetry parameter $\xi = R_{2y}/R_{2x}$, $\xi = 39.8/40 = 0.995$.

can be delocalized. Hence, we can divide the ranges of ΔE_{12} and S in mainly localized states and mainly delocalized states regions (see vertical and horizontal lines). The number of delocalized states decreases when the asymmetry increases; these can be evaluated by comparing Figures 10(b) and 11. It is clear that when the asymmetry becomes increasingly larger, the states with $\langle x \rangle \sim 0$ disappear.

The violation of DQW shape symmetry largely effects the spectral distribution of localized/delocalized states by varying the energy level splitting, manifested by a large energy difference ΔE_{12} . This effect can favorably be applied to make a nanosensing functionality. We present in Figure 12 results of modeling an asymmetric DQW with a protuberance at the central edge of QW_2 , as is shown in Figure 12(a). The protuberance plays the role of either a defect grown with the quantum dot or a foreign material adsorbed on the surface of a dot that was initially identical to its peer.

It appears from data in Figure 12 that the degree of delocalization is a direct function of the size of the protuberance, which as indicated above could be a defect or an adsorbed substance. This offers the possibility to sense the protuberance size. Calibration of this sensing functionality can be done through our modeling and by varying the size of the defect, respectively, the adsorbed substance.

5. Conclusion

We studied the spectral distribution of localized/delocalized states in DQW. The electron localization in DQW appeared extremely sensitive to small violations of symmetry in DQWs due to relation (5) for ΔE_{12} nearing zero. The extreme sensitivity to symmetry violations, found through our modeling, can be technologically important.

The observed electron behavior in double quantum structures can be interpreted in terms of the uncertainty principle. We have shown that the spectral distribution of the electron average coordinate $\langle x \rangle$ is distinctly different for various types

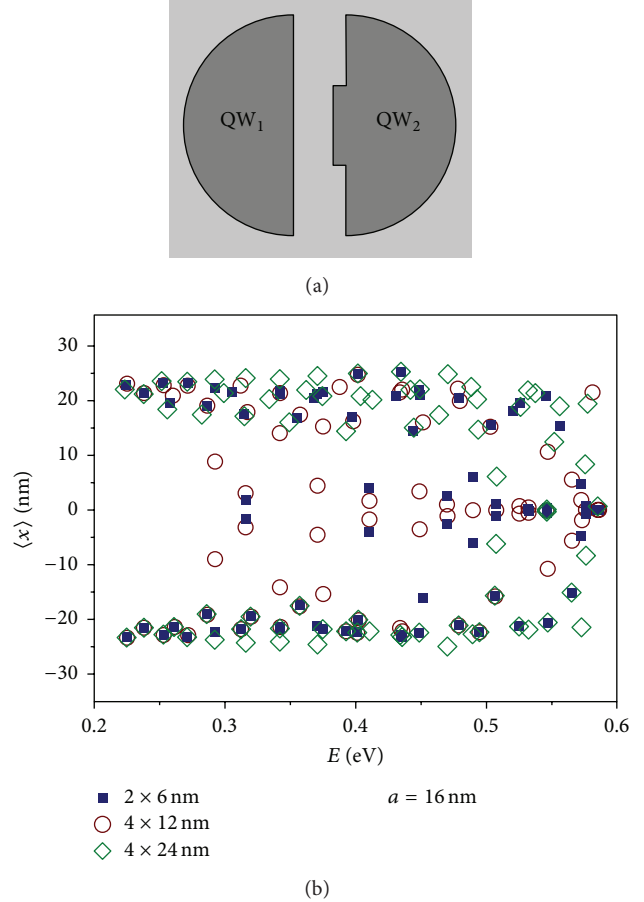


FIGURE 12: (a) Semicircle shaped DQW, where the asymmetry is generated by a rectangular defect in the right QW. The defect height, H , and width, D , were varied, as indicated in the inset, while the radii and the dot interdistance are maintained constant ($R_1 = R_2 = 40$ nm and $a = 16$ nm). (b) Electron average position $\langle x \rangle$ plotted against the electron spectrum of the asymmetric DQWs.

of DQW symmetry violations. It appeared that the ideal case of identical QWs cannot be reliably modeled numerically, since the closer the DQW to perfectly symmetric shape, the higher the effect of numerical discretization on tunneling properties.

We demonstrated that the DQW is a quantum system suitable for sensing tiny substances adsorbed on one of the quantum dots constituting the DQW or by a defect in one of the dots. The protuberance volume capable of breaking the symmetry, changing the quantum states of the DQW, and provoking tunneling was estimated to contain one to several thousand atoms, which is in the range of the size of polymer macromolecules and biomolecules.

Conflict of Interests

The authors declare that there is no conflict of interests regarding the publication of this paper.

Acknowledgments

This work is supported by NSF (HRD-1345219) and MSRDC consortium (Award 001 W911SR-14-2-0001-0002).

References

- [1] C. Cohen-Tannoudji, B. Diu, and F. Laloe, *Quantum Mechanics*, vol. 1, Wiley-VCH, Weinheim, Germany, 1977.
- [2] L. R. C. Fonseca, J. L. Jimenez, and J. P. Leburton, "Anomalous peak effect in CeRu_2 and 2H-NbSe_2 : fracturing of a flux line lattice," *Physical Review B*, vol. 58, no. 2, pp. 995–999, 1998.
- [3] R. S. Whitney, H. Schomerus, and M. Kopp, "Semiclassical transport in nearly symmetric quantum dots. I. Symmetry breaking in the dot," *Physical Review E*, vol. 80, no. 5, Article ID 056209, 2009.
- [4] Ł. Kłopotowski, M. Nawrocki, S. Maćkowski, and E. Janik, "Spin conserving tunneling in asymmetric double quantum well structures," *Physica Status Solidi (B)*, vol. 229, no. 2, pp. 769–774, 2002.
- [5] W. G. van der Wiel, S. De Franceschi, J. M. Elzerman, T. Fujisawa, S. Tarucha, and L. P. Kouwenhoven, "Electron transport through double quantum dots," *Reviews of Modern Physics*, vol. 75, no. 1, pp. 1–22, 2003.
- [6] Y. I. Mazur, V. G. Dorogan, E. Marega Jr. et al., "Tunneling-barrier controlled excitation transfer in hybrid quantum dot-quantum well nanostructures," *Journal of Applied Physics*, vol. 108, no. 7, Article ID 074316, 2010.
- [7] I. Filikhin, S. G. Matinyan, and B. Vlahovic, "Electron spectrum, localization and tunneling in double nanoscale structures," *Mathematical Modelling and Geometry*, vol. 2, no. 2, pp. 1–18, 2014.
- [8] L. A. Ponomarenko, F. Schedin, M. I. Katsnelson et al., "Chaotic dirac billiard in graphene quantum dots," *Science*, vol. 320, no. 5874, pp. 356–358, 2008.
- [9] R. S. Whitney, P. Marconcini, and M. Macucci, "Huge conductance peak caused by symmetry in double quantum dots," *Physical Review Letters*, vol. 102, no. 18, Article ID 186802, 2009.
- [10] N. Ha, T. Mano, T. Kuroda et al., "Droplet epitaxy growth of telecom InAs quantum dots on metamorphic InAlAs/GaAs(111)A," *Japanese Journal of Applied Physics*, vol. 54, no. 4, supplement, Article ID 04DH07, 2015.
- [11] N. Ha, X. Liu, T. Mano et al., "Droplet epitaxial growth of highly symmetric quantum dots emitting at telecommunication wavelengths on InP(111)A," *Applied Physics Letters*, vol. 104, no. 14, Article ID 143106, 2014.
- [12] I. Filikhin, V. M. Suslov, and B. Vlahovic, "Modeling of In As/Ga As quantum ring capacitance spectroscopy in the nonparabolic approximation," *Physical Review B*, vol. 73, no. 20, Article ID 205332, 2006.
- [13] I. Filikhin, V. M. Suslov, M. H. Wu, and B. Vlahovic, "Effective approach for strained InAs/GaAs quantum structures," *Physica E: Low-Dimensional Systems and Nanostructures*, vol. 40, no. 4, pp. 715–723, 2008.
- [14] C. A. Duque, N. Porrás-Montenegro, Z. Barticevic, M. Pacheco, and L. E. Oliveira, "Electron-hole transitions in self-assembled InAs/GaAs quantum dots: effects of applied magnetic fields and hydrostatic pressure," *Microelectronics Journal*, vol. 36, no. 3–6, pp. 231–233, 2005.
- [15] M. Levinshtein, S. Rumyantsev, and M. Shur, *Handbook Series on Semiconductor Parameters*, World Scientific, Singapore, 1999.
- [16] A. Schliwa, M. Winkelkemper, and D. Bimberg, "Impact of size, shape, and composition on piezoelectric effects and electronic properties of In(Ga)As/GaAs quantum dots," *Physical Review B*, vol. 76, no. 20, Article ID 205324, 2007.
- [17] I. Filikhin, V. M. Suslov, M. Wu, and B. Vlahovic, "InGaAs/GaAs quantum dots within an effective approach," *Physica E: Low-Dimensional Systems and Nanostructures*, vol. 41, no. 7, pp. 1358–1363, 2009.
- [18] I. Filikhin, G. S. Matinyan, and B. Vlahovic, "Tunneling rate in double quantum wells," *Sensors & Transducers*, vol. 183, no. 12, pp. 116–122, 2014.

Research Article

Research on Acetylene Sensing Properties and Mechanism of SnO₂ Based Chemical Gas Sensor Decorated with Sm₂O₃

Qu Zhou,¹ Meiqing Cao,² Wude Li,² Chao Tang,¹ and Shiping Zhu¹

¹College of Engineering and Technology, Southwest University, Chongqing 400715, China

²State Grid Chongqing Hechuan District Power Supply Company, Chongqing 401520, China

Correspondence should be addressed to Qu Zhou; zhouqu@swu.edu.cn

Received 1 July 2015; Revised 25 September 2015; Accepted 29 September 2015

Academic Editor: Zhenyu Li

Copyright © 2015 Qu Zhou et al. This is an open access article distributed under the Creative Commons Attribution License, which permits unrestricted use, distribution, and reproduction in any medium, provided the original work is properly cited.

Acetylene C₂H₂ gas is one of the most important fault characteristic hydrocarbon gases dissolved in oil immersed power transformer oil. This paper reports the successful preparation and characterization of samarium oxide Sm₂O₃ decorated tin oxide SnO₂ based sensors with hierarchical rod structure for C₂H₂ gas detection. Pure and Sm₂O₃ decorated SnO₂ sensing structures were synthesized by a facile hydrothermal method and characterized by XRD, FESEM, TEM, EDS, and XPS measurements, respectively. Planar chemical gas sensors with the synthesis samples were fabricated, and their sensing performances to C₂H₂ gas were systematically performed and automatically recorded by a CGS-1 TP intelligent gas sensing analysis system. The optimum operating temperature of the Sm₂O₃ decorated SnO₂ based sensor towards 50 μL/L of C₂H₂ is 260°C, and its corresponding response value is 38.12, which is 6 times larger than the pure one. Its response time is about 8–10 s and 10–13 s for recovery time. Meanwhile good stability and reproducibility of the decorated sensor to C₂H₂ gas are also obtained. Furthermore, the proposed sensor exhibits excellent C₂H₂ selectivity among some potential interface gases, like H₂ and CO gas. All sensing results indicate the sensor fabricated with oxide Sm₂O₃ decorated SnO₂ nanorods might be a promising candidate for C₂H₂ detection in practice.

1. Introduction

Large-scale power transformers are expensive and significant electric apparatus in electric grid system [1, 2]. At present, a large number of power transformers are still in oil-paper insulation structure, and some insulating defects unavoidably exist during transformer design, manufacturer, installation and operation [3]. Once potential insulating faults happened on power transformers, some fault characteristic gases, like hydrogen, carbon monoxide, carbon dioxide, methane, ethane, ethylene, acetylene, and so forth, would appear and then dissolve into transformer oil [4, 5]. Among them, acetylene gas C₂H₂ is the most effective one to identify thermal and electrical faults. Thus, how to rapidly and accurately detect C₂H₂ gas is currently the subject of intensive research and great attention has been focused on this issue for the past few years [1–6].

In recent years, various types of gas sensing technologies have been proposed to detect transformer fault characteristic gases, such as metal oxide semiconductors [7, 8], gas

chromatograph, carbon nanotubes [9], and photoacoustic spectroscopy and Raman spectroscopy [10, 11]. Gas chromatography is mainly used as offline experiment, and spectroscopy is only in the stage of laboratory study and has a long way for practical application. With the advantages of simple manufacture technique, low cost, long life, rapid response, and recovery time, semiconductor SnO₂ may be the most promising sensing technology for detecting and recognizing dissolved fault characteristic gases in transformer oil [12–15]. However, some limitations, like high operating temperature, unsatisfactory selectivity, and poor long-term stability, are still needed to be further improved [16–21]. Doping modification with noble, rare-earth, and transition metals has been proved to be an effective method to improve the sensing properties of metal oxide semiconductors [22–29].

Hence, in this work we proposed the research of semiconductor SnO₂ based chemical gas sensor decorated with rare-earth oxide Sm₂O₃ for C₂H₂ detection. Firstly Sm₂O₃ decorated SnO₂ nanorods were successfully synthesized with a facile and environment friendly hydrothermal method

and characterized by X-ray diffraction (XRD), field emission scanning electron microscopy (FESEM), transmission electron microscopy (TEM), energy dispersive X-ray spectroscopy (EDS), and X-ray photoelectron spectroscopy (XPS) measurements, respectively. And then planar chemical gas sensors with the synthesis samples were fabricated with screen-printing technology, and their sensing performances towards C_2H_2 gas were systematically performed and automatically recorded by a CGS-1 TP intelligent gas sensing analysis system. Finally a possible sensing mechanism was discussed and proposed.

2. Experimental

All the raw chemical reagents were of analytical grade purchased from Chongqing Chuandong Chemical Reagent Co., Ltd. (Chongqing, China), and used as received without any further purification. Sm_2O_3 decorated SnO_2 nanostructures were prepared by a facile and environment friendly hydrothermal method using $Na_2SnO_3 \cdot 3H_2O$, $Sm(NO_3)_3 \cdot 6H_2O$, $C_6H_8O_7 \cdot H_2O$, NaOH, absolute ethanol, and distilled water as precursors.

In a typical procedure, 0.81 g of $Na_2SnO_3 \cdot 3H_2O$, 0.68 g of NaOH, 30 mL of absolute ethanol, and 30 mL of distilled water were firstly mixed together. Then, 0.05 g of compound metal salt $Sm(NO_3)_3 \cdot 6H_2O$ and 0.24 g of $C_6H_8O_7 \cdot H_2O$ were added to the mixed solution with intense magnetic stirring. It was magnetically stirred for about 45 min and then transferred into a 100 mL Teflon-lined stainless steel autoclave, sealed and maintained at $180^\circ C$ for 24 h. After the reaction was completed, the autoclave was cooled to room temperature naturally. The white precipitates were collected and washed with distilled water and absolute ethanol several times to eliminate the unwanted residues. Finally, the products were further air-dried and heated for further use. Pure SnO_2 nanostructures were also prepared for comparison with a similar synthesis route mentioned above.

The crystalline structures of the prepared pure and Sm_2O_3 decorated SnO_2 nanostructures were investigated by X-ray powder diffraction (XRD, Rigaku D/Max-1200X) with Cu $K\alpha$ radiation (40 kV, 200 mA and $\lambda = 1.5418 \text{ \AA}$). The microstructures and morphologies of prepared samples were characterized by means of field emission scanning electron microscope (FESEM, Hillsboro equipped with energy dispersive X-ray (EDS) spectroscopy) and transmission electron micrographs (TEM, Hitachi S-570). Analysis of the X-ray photoelectron spectra (XPS) was performed on an ESCLAB MKII using Al as the exciting source.

Planar chemical gas sensors were fabricated with screen-printing technique, and the ceramic substrates were purchased from Beijing Elite Tech Co., Ltd., China [18]. Figure 1 shows the structure chart of the planar chemical gas sensor. As demonstrated in Figure 1 the planar chemical sensor is composed of three significant components, ceramic substrate, Ag-Pd interdigital electrodes, and sensing materials. The length, width, and height of the planar ceramic substrate are about 13.4, 7, and 1 mm, respectively. The synthesized sensing nanostructures were dispersed with distilled water and absolute ethanol in a weight ratio of 100:20:10 to

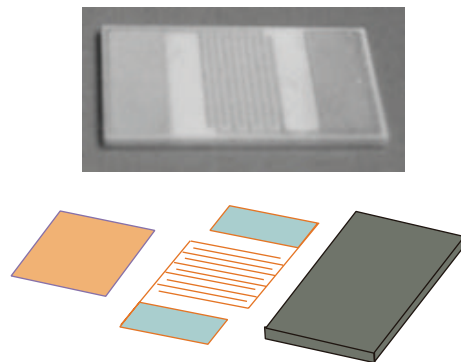


FIGURE 1: Structure chart of the fabricated planar sensor.



FIGURE 2: The CGS-1TP gas sensing analysis system.

form a homogeneous paste. Then the paste was subsequently screen-printed onto the planar ceramic substrate to generate a uniform gas-sensing film. Finally, the fabricated sensor was dried in air at $80^\circ C$ to volatilize the organic solvent and further aged at $300^\circ C$ for 2 days to improve its stability before testing.

Gas-sensing properties were measured using the Chemical Gas Sensor-1 Temperature Pressure (CGS-1TP) intelligent gas sensing analysis system [18], which was purchased from Beijing Elite Tech Co., Ltd., China. Figure 2 illustrates the schematic diagram of the CGS-1TP gas sensing analysis system, which could offer an external temperature control ranging from room temperature to $500^\circ C$ with an adjustment precision of $1^\circ C$. The first step in testing process was to put the fabricated gas sensor into the test chamber and fix its electrodes by adjusting the two probes on each side to collect electrical signals. When the sensor resistance reached a constant value, certain amount of C_2H_2 was injected into the chamber by a microinjector through a rubber plug. Open the upper cover of the test chamber to recover the sensor until the resistance attained a new stable value. The sensor resistance and sensitivity were automatically collected and analyzed by the system. And the environmental temperature, relative humidity, and working temperature were also recorded by the analysis system.

The sensor sensitivity (S) in this paper was defined as $S = R_a/R_g$, where R_a represented the resistance of the sensor in air and R_g in certain concentration of C_2H_2 mixed with air,

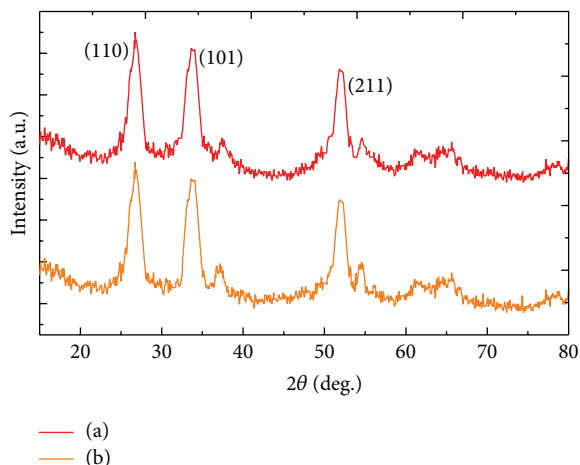


FIGURE 3: Typical XRD patterns of (a) pure and (b) Sm_2O_3 decorated SnO_2 nanostructures.

respectively [30]. The time taken by the sensor to achieve 90% of the total resistance change was designated as the response time in the case of gas adsorption and the recovery time in the case of gas desorption [31]. All gas sensing measurements were repeated several times to ensure the repeatability of the sensor against C_2H_2 gas [31, 32].

3. Results and Discussion

XRD measurement was firstly performed to determine the crystalline structures of the as-synthesized samples. Figure 3 presents the typical XRD patterns of the prepared pure and Sm_2O_3 decorated SnO_2 nanostructures. One can clearly see in Figure 3 that these nanostructures are polycrystalline in nature. The prominent peaks of (110), (101), and (211) and other smaller peaks are well in accordance with the standard spectrum of the tetragonal rutile SnO_2 given in the standard data file (JCPDS file no. 41-1445). No peaks from samarium atom and its oxide are observed, which might be attributed to the high dispersion and the low amount of Sm in the synthesized SnO_2 samples.

To check whether Sm element has been successfully doped into the synthesized SnO_2 nanostructures, energy dispersive X-ray spectroscopy measurement was performed. Figure 4 is the EDS spectrum of the synthesized Sm_2O_3 decorated SnO_2 nanostructures. Peaks from Sn, Sm, and O are observed and the atomic ratio of Sm to Sn is calculated to be about 3.13 at %, which confirms the availability of Sm dopant in the synthesized SnO_2 nanostructures.

To further verify the existence of Sm atom and its valence in the synthesized SnO_2 samples, XPS analyses (Figure 5) were performed and XPS data was collected. Adventitious hydrocarbon C 1s binding energy at 285 eV was used as a reference to correct the energy shift of O 1s. Figure 6 shows the wide survey spectrum of the samples, confirming the existence of Sn, O, and Sm. The binding energies from Sn 3d, 3p, and 3s correspond to Sn^{4+} . And the peak at 1084.3 eV is identified as $\text{Sm} 2d_{5/2}$, which could be attributed to Sm^{3+} ions.

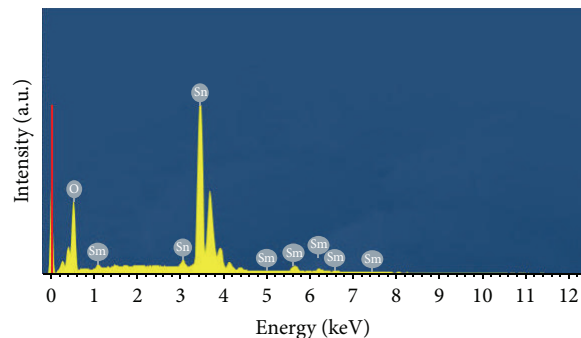


FIGURE 4: EDS spectrum of Sm_2O_3 decorated SnO_2 nanostructures.

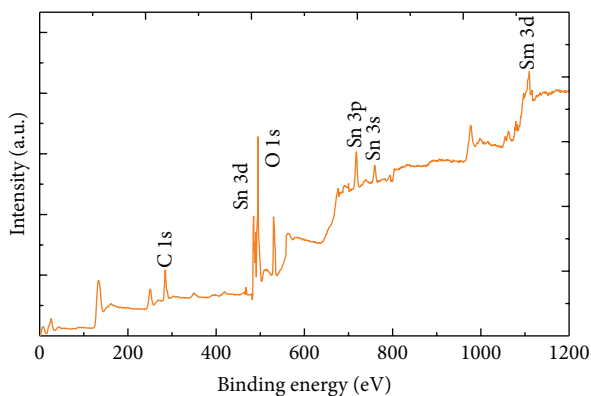


FIGURE 5: XPS survey spectra of Sm_2O_3 decorated SnO_2 nanostructures.

The overall surface morphologies and structural features of the synthesized pure and Sm_2O_3 decorated SnO_2 samples were performed by FESEM, TEM, and SAED measurements and represented in Figure 6. As shown in Figures 6(a)–6(c) numerous rod-like nanostructures with uniform shape and size can be clearly seen, and no other morphologies were observed, revealing a high yield of the products. The TEM image in Figure 6(c) illustrates that both the shape and size of the Sm_2O_3 decorated SnO_2 are exactly consistent with the demonstrated FESEM images. The corresponding SAED pattern as shown in Figure 6(d) verifies the polycrystalline structures of the synthesized Sm_2O_3 decorated SnO_2 nanorods, which coincides well with the XRD results shown in Figure 3.

It is known to all that operating temperature is an important and fundamental characteristic for a semiconductor gas sensor, which has a significant influence on its sensing response. Figure 7 demonstrates the response curves of the prepared pure and Sm_2O_3 decorated SnO_2 nanorods sensors to $50 \mu\text{L/L}$ of C_2H_2 as a function of working temperature ranging from 140°C to 410°C with an interval of 30°C . Apparently, for each sensor the gas response increases quickly and obtains its maximum and then decreases rapidly with further increase of working temperature. Compared with pure SnO_2 sensor, Sm_2O_3 decorated SnO_2 nanorods sensor exhibits a higher resistance value at the same working temperature. The optimum operating temperature of the decorated one to

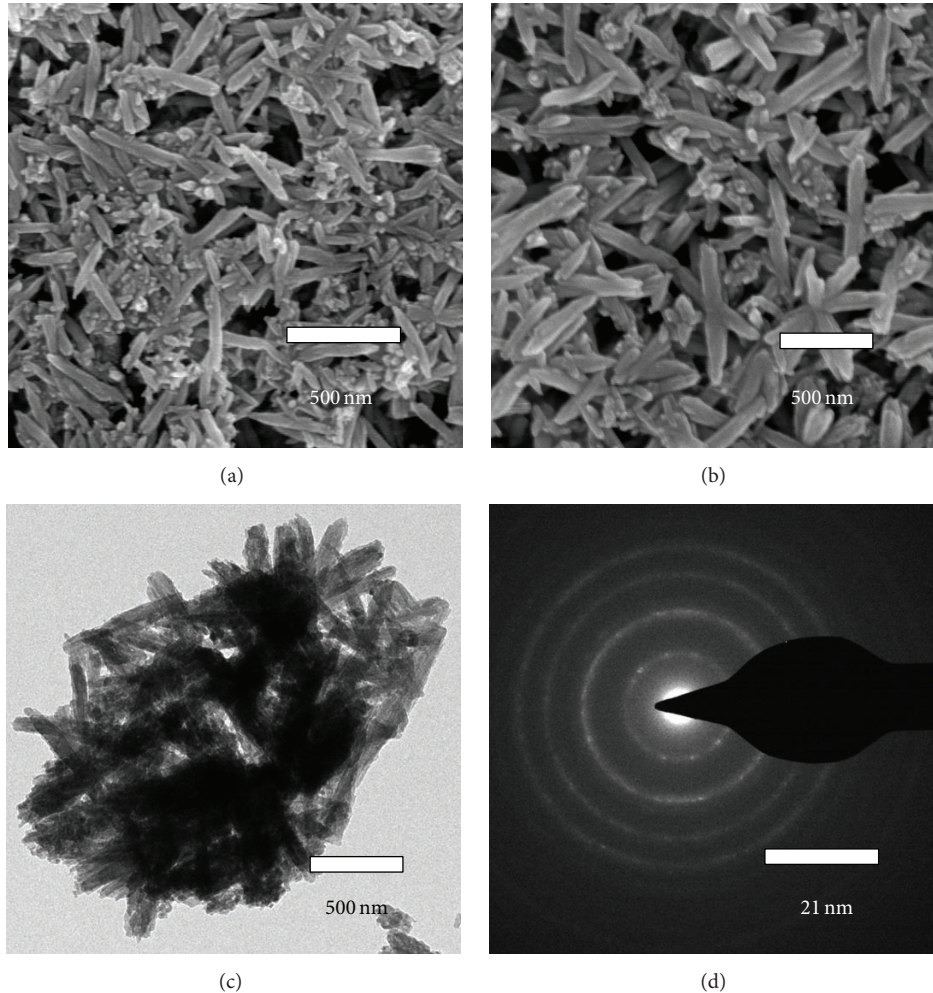


FIGURE 6: FESEM images of (a) pure SnO_2 and (b) Sm_2O_3 decorated SnO_2 and TEM image (c) and SAED image (d) of Sm_2O_3 decorated SnO_2 .

$50 \mu\text{L/L}$ of C_2H_2 is 260°C with the corresponding maximum response value 38.12. And it is 7.53 for the pure one at 320°C , where the sensor exhibits the maximum gas response.

Figure 8 demonstrates the gas responses of the prepared sensors as a function of C_2H_2 concentration with sensor working at its optimum operating temperature measured above. As represented, the sensing responses of the sensors versus C_2H_2 increase greatly with increasing gas concentration in the range of $1\text{--}100 \mu\text{L/L}$, change much more slowly from $100 \mu\text{L/L}$ to $400 \mu\text{L/L}$, and obtain saturation when exposed to more than $400 \mu\text{L/L}$. The saturated sensing responses were measured to be about 68.87 and 18.61 for the Sm_2O_3 decorated SnO_2 nanorods sensor and the pure one.

To investigate the response-recovery characteristic, stability, and repeatability of the Sm_2O_3 decorated SnO_2 nanorods sensor, it was sequentially exposed to various concentrations of C_2H_2 gas as shown in Figure 9 (5, 10, 20, 50, and $100 \mu\text{L/L}$) and equal concentration as shown in Figure 10 ($20 \mu\text{L/L}$). As shown in Figures 9 and 10, the sensor response increases rapidly when exposed to certain concentration of C_2H_2 and decreases dramatically when exposed to air

for recovering. The time spent for gas sensing is measured about 8–10 s and 10–13 s for sensor recovering. Meanwhile, the gas response of the sensor always returns to its initial value during the continuous test period, implying a very satisfying reproducibility of the prepared Sm_2O_3 decorated SnO_2 nanorods sensor.

Figure 11 depicts the histogram of the gas responses of the pure and Sm_2O_3 decorated SnO_2 nanorods sensors to $20 \mu\text{L/L}$ of various gases at 260°C , including C_2H_2 , CO, and H_2 . It can be clearly seen in Figure 11 that the decorated sensor shows excellent C_2H_2 sensing response among these two potential interface gases.

SnO_2 is a typical n-type oxide semiconducting sensing material, and its gas sensing properties are predominantly controlled by its surface resistance [32–35]. As it is known, when the sensor is exposed to air, oxygen would be absorbed on SnO_2 surface firstly. Due to strong electronegativity, the absorbed oxygen acts as a trap capturing electrons from the condition band of SnO_2 to form chemisorbed oxygen species like O^{2-} , O^- , or O_2^- [36]. Consequently, a depletion region on the surface appears, resulting in a decline of

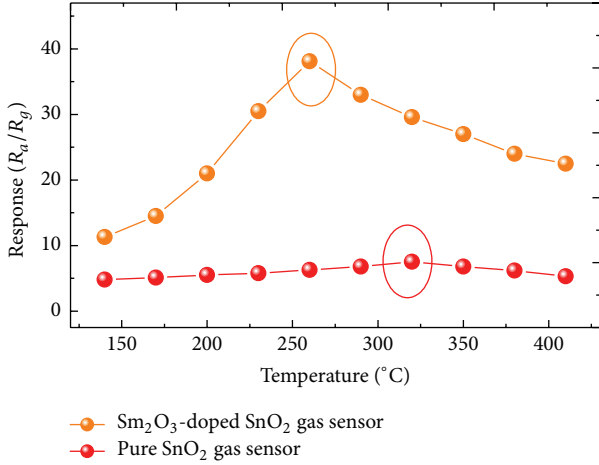


FIGURE 7: Gas responses of the sensors to 50 $\mu\text{L/L}$ of C_2H_2 at various working temperature.

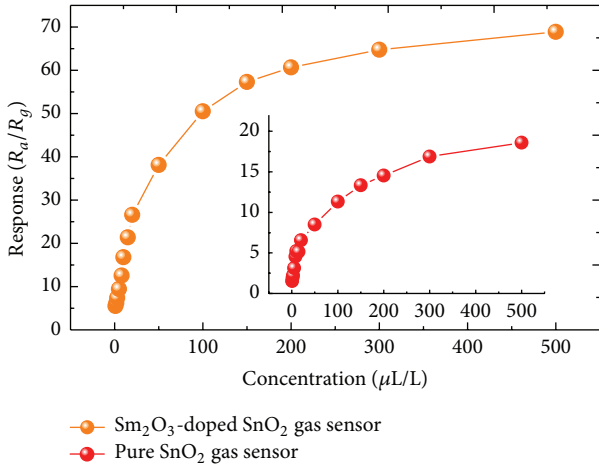


FIGURE 8: Gas responses of the sensors versus different concentration of C_2H_2 from 1 to 500 $\mu\text{L/L}$.

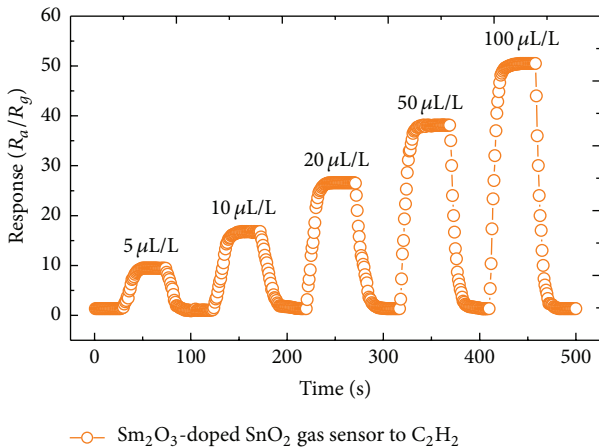


FIGURE 9: Dynamic C_2H_2 sensing transients of the Sm_2O_3 decorated SnO_2 nanorods sensor at 260°C .

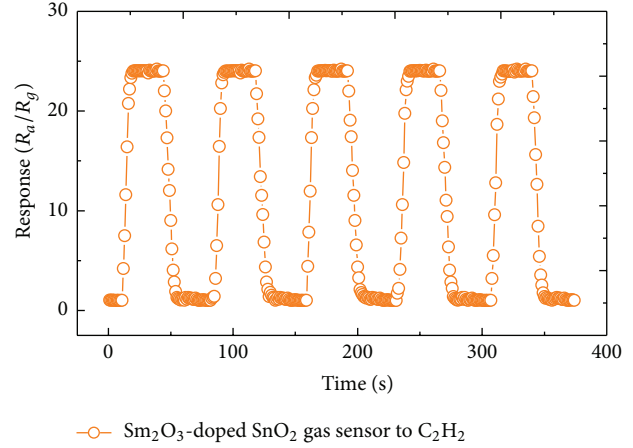


FIGURE 10: Reproducibility of the Sm_2O_3 decorated SnO_2 nanorods sensor to 20 $\mu\text{L/L}$ of C_2H_2 at 260°C .

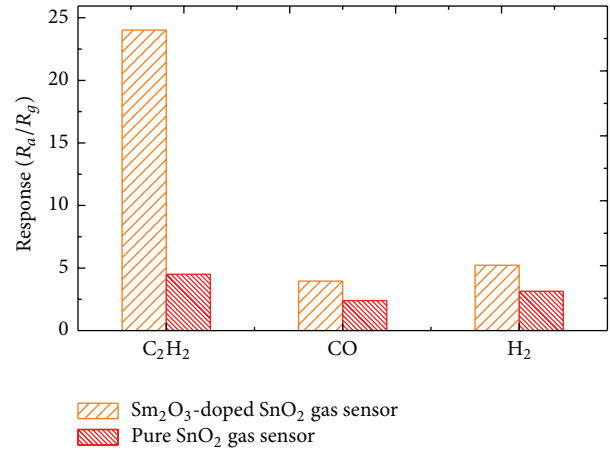


FIGURE 11: Selectivity of the pure and Sm_2O_3 decorated SnO_2 nanorods sensors to 20 $\mu\text{L/L}$ of C_2H_2 , CO , and H_2 at 260°C .

the carrier concentration and an increased sensor resistance. As C_2H_2 gas is introduced, the relevant chemical reactions take place between C_2H_2 gas and the ionized oxygen. The trapped electrons are released back to the conduction band of SnO_2 surface, increasing the conductivity of the sensor; thus a decreased resistance is measured.

Based on the sensing experiments demonstrated above, oxide Sm_2O_3 has a significant impact on improving the sensing properties of SnO_2 based gas sensor to C_2H_2 . A possible sensing mechanism of the Sm_2O_3 decorated SnO_2 based sensor to C_2H_2 may be explained as follows [37, 38]. Firstly, oxide Sm_2O_3 might work as an effective catalyst, which benefits the effect of active center for C_2H_2 adsorption. Secondly, the incorporation of Sm^{3+} ions might change the electronic movement and the overlap of electron cloud of SnO_2 sensing material, which further strengthens the electronegativity of carbon-hydrogen triple bond of C_2H_2 and makes it easier for hydrogen dissociation to combine with O^{2-} . Therefore, much more electrons have been released in this process so that SnO_2 resistance declines dramatically. Thirdly, the addition

of Sm_2O_3 could restrict the crystallite growth of SnO_2 . That is to say, after decorating both the diameter and the length of the synthesized SnO_2 nanorods diminish, which would provide more active sites for oxygen adsorption and channels for gas sensing. Therefore, the Sm_2O_3 decorated SnO_2 based sensor exhibits a higher gas response at a relatively lower operating temperature to C_2H_2 gas with rapid response-recovery, excellent stability, reproducibility, and selectivity.

4. Conclusions

In this work, pure and oxide Sm_2O_3 decorated SnO_2 nanorods were successfully synthesized with a facile and simple hydrothermal method and carefully characterized by XRD, FESEM, TEM, EDS, and XPS measurements, respectively. Planar chemical gas sensors with the synthesis samples were fabricated, and their sensing performances to C_2H_2 gas were systematically performed and automatically recorded by a CGS-1 TP intelligent gas sensing analysis system. Compared with the pure one, the Sm_2O_3 decorated SnO_2 nanorods based sensor exhibits lower optimum operating temperature, higher sensing response, quick response and response time, good stability and reproducibility, and excellent selectivity among potential interface gases. All results indicate the sensor fabricated with oxide Sm_2O_3 decorated SnO_2 nanorods might be a promising candidate for C_2H_2 detection in practice.

Conflict of Interests

The authors declare that there is no conflict of interests regarding the publication of this paper.

Acknowledgments

This work has been supported in part by the National Natural Science Foundation of China (nos. 51507144 and 51277185), Fundamental Research Funds for the Central Universities (nos. XDJK2015B005 and SWU114051), National Special Fund for Major Research Instrumentation Development (no. 2012YQ160007), and the Funds for Innovative Research Groups of China (no. 51021005).

References

- [1] Q. Zhou, W. G. Chen, S. D. Peng, and W. Zeng, "Hydrothermal synthesis and acetylene sensing properties of variety low dimensional zinc oxide nanostructures," *The Scientific World Journal*, vol. 2014, Article ID 489170, 8 pages, 2014.
- [2] T. Somekawa, M. Kasaoka, F. Kawachi, Y. Nagano, M. Fujita, and Y. Izawa, "Analysis of dissolved C_2H_2 in transformer oils using laser Raman spectroscopy," *Optics Letters*, vol. 38, no. 7, pp. 1086–1088, 2013.
- [3] D. R. Morais and J. G. Rolim, "A hybrid tool for detection of incipient faults in transformers based on the dissolved gas analysis of insulating oil," *IEEE Transactions on Power Delivery*, vol. 21, no. 2, pp. 673–680, 2006.
- [4] C. M. Quintella, M. Meira, W. L. Silva et al., "Development of a spectrofluorimetry-based device for determining the acetylene content in the oils of power transformers," *Talanta*, vol. 117, no. 15, pp. 263–267, 2013.
- [5] A. Akbari, A. Setayeshmehr, H. Borsi, E. Gockenbach, and I. Fofana, "Intelligent agent-based system using dissolved gas analysis to detect incipient faults in power transformers," *IEEE Electrical Insulation Magazine*, vol. 26, no. 6, pp. 27–40, 2010.
- [6] S. Singh and M. Bandyopadhyay, "Dissolved gas analysis technique for incipient fault diagnosis in power transformers: a bibliographic survey," *IEEE Electrical Insulation Magazine*, vol. 26, no. 6, pp. 41–46, 2010.
- [7] X. C. Wang, M. G. Zhao, F. Liu, J. F. Jia, X. J. Li, and L. L. Cao, " C_2H_2 gas sensor based on Ni-doped ZnO electrospun nanofibers," *Ceramics International*, vol. 39, no. 3, pp. 2883–2887, 2013.
- [8] W. G. Chen, Q. Zhou, T. Y. Gao, X. P. Su, and F. Wan, "Pd-doped SnO_2 -based sensor detecting characteristic fault hydrocarbon gases in transformer oil," *Journal of Nanomaterials*, vol. 2013, Article ID 127345, 9 pages, 2013.
- [9] X. X. Zhang, J. B. Zhang, R. H. Li, and Y. F. Liao, "Application of hydroxylated single-walled carbon nanotubes for the detection of C_2H_2 gases in transformer oil," *Journal of Computational and Theoretical Nanoscience*, vol. 10, no. 2, pp. 399–404, 2013.
- [10] Z. Y. Wu, Y. H. Gong, and Q. X. Yu, "Photoacoustic spectroscopy detection and extraction of discharge feature gases in transformer oil based on 1.5 μ tunable fiber laser," *Infrared Physics & Technology*, vol. 58, no. 5, pp. 86–90, 2013.
- [11] W. G. Chen, C. Pan, Y. X. Yun, and Y. Liu, "Wavelet networks in power transformers diagnosis using dissolved gas analysis," *IEEE Transactions on Power Delivery*, vol. 24, no. 1, pp. 187–194, 2009.
- [12] J. Zhang, S. Wang, M. Xu et al., "Hierarchically porous ZnO architectures for gas sensor application," *Crystal Growth and Design*, vol. 9, no. 8, pp. 3532–3537, 2009.
- [13] J. Gong, Y. Li, Z. Hu, Z. Zhou, and Y. Deng, "Ultrasensitive NH_3 gas sensor from polyaniline nanograin enclashed TiO_2 fibers," *Journal of Physical Chemistry C*, vol. 114, no. 21, pp. 9970–9974, 2010.
- [14] D. Liu, T. Liu, H. Zhang, C. Lv, W. Zeng, and J. Zhang, "Gas sensing mechanism and properties of Ce-doped SnO_2 sensors for volatile organic compounds," *Materials Science in Semiconductor Processing*, vol. 15, no. 4, pp. 438–444, 2012.
- [15] K. J. Choi and H. W. Jang, "One-dimensional oxide nanostructures as gas-sensing materials: review and issues," *Sensors*, vol. 10, no. 4, pp. 4083–4099, 2010.
- [16] Y. J. Chen, X. Y. Xue, Y. G. Wang, and T. H. Wang, "Synthesis and ethanol sensing characteristics of single crystalline SnO_2 nanorods," *Applied Physics Letters*, vol. 87, no. 23, Article ID 233503, 3 pages, 2005.
- [17] C. Wang, L. Yin, L. Zhang, D. Xiang, and R. Gao, "Metal oxide gas sensors: sensitivity and influencing factors," *Sensors*, vol. 10, no. 3, pp. 2088–2106, 2010.
- [18] W. Chen, Q. Zhou, L. Xu, F. Wan, S. Peng, and W. Zeng, "Improved methane sensing properties of Co-doped SnO_2 electrospun nanofibers," *Journal of Nanomaterials*, vol. 2013, Article ID 173232, 9 pages, 2013.
- [19] W. Zeng, B. Miao, Q. Zhou, and L. Y. Lin, "Hydrothermal synthesis and gas sensing properties of variety low dimensional nanostructures of SnO_2 ," *Physica E*, vol. 47, no. 3, pp. 116–121, 2013.
- [20] Y.-X. Yin, L.-Y. Jiang, L.-J. Wan, C.-J. Li, and Y.-G. Guo, "Polyethylene glycol-directed SnO_2 nanowires for enhanced

- gas-sensing properties,” *Nanoscale*, vol. 3, no. 4, pp. 1802–1806, 2011.
- [21] B. Wang, L. F. Zhu, Y. H. Yang, N. S. Xu, and G. W. Yang, “Fabrication of a SnO₂ nanowire gas sensor and sensor performance for hydrogen,” *Journal of Physical Chemistry C*, vol. 112, no. 17, pp. 6643–6647, 2008.
- [22] W. Zeng, T. M. Liu, Z. C. Wang, S. Tsukimoto, M. Saito, and Y. Ikuhara, “Selective detection of formaldehyde gas using a Cd-doped TiO₂-SnO₂ sensor,” *Sensors*, vol. 9, no. 11, pp. 9029–9038, 2009.
- [23] X. Liu, J. Zhang, X. Guo, S. Wu, and S. Wang, “Enhanced sensor response of Ni-doped SnO₂ hollow spheres,” *Sensors and Actuators B: Chemical*, vol. 152, no. 2, pp. 162–167, 2011.
- [24] Z. Li and Y. Dzenis, “Highly efficient rapid ethanol sensing based on Co-doped In₂O₃ nanowires,” *Talanta*, vol. 85, no. 1, pp. 82–85, 2011.
- [25] W. Zeng, T. M. Liu, and Z. C. Wang, “Enhanced gas sensing properties by SnO₂ nanosphere functionalized TiO₂ nanobelts,” *Journal of Materials Chemistry*, vol. 22, no. 8, pp. 3544–3548, 2012.
- [26] X. Song, Z. Wang, Y. Liu, C. Wang, and L. Li, “A highly sensitive ethanol sensor based on mesoporous ZnO-SnO₂ nanofibers,” *Nanotechnology*, vol. 20, no. 7, Article ID 075501, 2009.
- [27] X. Zhu, H. Shi, J. Yin et al., “Facile preparation of CuO@SnO₂ nanobelts as a high-capacity and long-life anode for lithium-ion batteries,” *RSC Advances*, vol. 4, no. 65, pp. 34417–34420, 2014.
- [28] G. Neri, A. Bonavita, G. Micali et al., “Effect of the chemical composition on the sensing properties of In₂O₃-SnO₂ nanoparticles synthesized by a non-aqueous method,” *Sensors and Actuators B: Chemical*, vol. 130, no. 1, pp. 222–230, 2008.
- [29] F. Pourfayaz, A. Khodadadi, Y. Mortazavi, and S. S. Mohajerzadeh, “CeO₂ doped SnO₂ sensor selective to ethanol in presence of CO, LPG and CH₄,” *Sensors and Actuators, B: Chemical*, vol. 108, no. 1-2, pp. 172–176, 2005.
- [30] W. G. Chen, Q. Zhou, X. P. Su, L. N. Xu, and S. D. Peng, “Morphology control of tin oxide nanostructures and sensing performances for acetylene detection,” *Sensors & Transducers*, vol. 154, no. 7, pp. 195–200, 2013.
- [31] Z. H. Jing and J. H. Zhan, “Fabrication and gas-sensing properties of porous ZnO nanoplates,” *Advanced Materials*, vol. 20, no. 23, pp. 4547–4551, 2008.
- [32] W. Zeng, T. M. Liu, D. J. Liu, and E. J. Han, “Hydrogen sensing and mechanism of M-doped SnO₂ (M=Cr³⁺, Cu²⁺ and Pd²⁺) nanocomposite,” *Sensors and Actuators B: Chemical*, vol. 160, no. 1, pp. 455–462, 2011.
- [33] H. Huang, C. K. Lim, M. S. Tse, J. Guo, and O. K. Tan, “SnO₂ nanorod arrays: low temperature growth, surface modification and field emission properties,” *Nanoscale*, vol. 4, no. 5, pp. 1491–1496, 2012.
- [34] X. F. Liu, J. Iqbal, S. L. Yang, B. He, and R. H. Yu, “Nitrogen doping-mediated room-temperature ferromagnetism in insulating Co-doped SnO₂ films,” *Applied Surface Science*, vol. 256, no. 14, pp. 4488–4492, 2010.
- [35] Q. Qi, T. Zhang, L. Liu, and X. Zheng, “Synthesis and toluene sensing properties of SnO₂ nanofibers,” *Sensors and Actuators, B: Chemical*, vol. 137, no. 2, pp. 471–475, 2009.
- [36] J. Yu, D. Zhao, X. Xu, X. Wang, and N. Zhang, “Study on RuO₂/SnO₂: novel and active catalysts for CO and CH₄ oxidation,” *ChemCatChem*, vol. 4, no. 8, pp. 1122–1132, 2012.
- [37] Q. Qi, T. Zhang, X. J. Zheng et al., “Electrical response of Sm₂O₃-doped SnO₂ to C₂H₂ and effect of humidity interference,” *Sensors and Actuators B: Chemical*, vol. 134, no. 1, pp. 36–42, 2008.
- [38] S. Ahmadnia-Feyzabad, Y. Mortazavi, A. A. Khodadadi, and S. Hemmati, “Sm₂O₃ doped-SnO₂ nanoparticles, very selective and sensitive to volatile organic compounds,” *Sensors and Actuators B: Chemical*, vol. 181, no. 5, pp. 910–918, 2013.

Research Article

Optical and Sensing Properties of Cu Doped ZnO Nanocrystalline Thin Films

R. K. Shukla,¹ Anchal Srivastava,¹ Nishant Kumar,¹ Akhilesh Pandey,² and Mamta Pandey¹

¹Department of Physics, University of Lucknow, Lucknow 226007, India

²Solid State Physics Laboratory (SSPL), DRDO, New Delhi 110054, India

Correspondence should be addressed to Anchal Srivastava; asrivastava.lu@gmail.com

Received 22 July 2015; Accepted 29 September 2015

Academic Editor: Wen Zeng

Copyright © 2015 R. K. Shukla et al. This is an open access article distributed under the Creative Commons Attribution License, which permits unrestricted use, distribution, and reproduction in any medium, provided the original work is properly cited.

Undoped and Cu doped ZnO films of two different molarities deposited by spray pyrolysis using zinc nitrate and cupric chloride as precursors show polycrystalline nature and hexagonal wurtzite structure of ZnO. The crystallite size varies between 10 and 21 nm. Doping increases the transmittance of the films whereas the optical band gap of ZnO is reduced from 3.28 to 3.18 eV. With increment in doping the surface morphology changes from irregular shaped grains to netted structure with holes and then to net making needle-like structures which lends gas sensing characteristics to the films. Undoped ZnO shows maximum sensitivity at 400°C for higher concentration of CO₂. The sensitivity of Cu doped sample is maximum at 200°C for all CO₂ concentrations from 500 to 4000 ppm.

1. Introduction

Zinc oxide, an environmentally safe and economic material, with wide direct band gap (3.37 eV) and large exciton binding energy (60 meV) at room temperature [1–3] finds application in fabrication of various devices including ultraviolet (UV) light-emitters, varistors, transparent high power electronics, piezoelectric transducers, gas sensors, smart windows, and solar cells [4–6]. It is one of the most important II-VI compound semiconductors and its application in optoelectronics can be expanded by altering its band gap energy. Doping of any metal can alter the band gap and/or can introduce energy levels in the band gap of semiconductor materials [7, 8]. Some metals can assume a valency depending on their chemical surrounding, for example, any copper salt when doped in ZnO using organometallic solution can lead to varied oxidation states of Cu [9]. The film based gas sensors depending on the detection of variation in some electrical parameter, resistance or capacitance, of the film utilize n-type semiconducting metal oxides such as ZnO. Also, metal oxides are stable at elevated temperatures in air [10].

There are several methods for producing ZnO based films, for example, chemical vapor deposition, thermal

evaporation, magnetron sputtering, pulsed laser deposition (PLD), laser chemical vapor deposition, and nonvacuum methods, namely, successive ionic layer absorption and reaction (SILAR), sol-gel spin coating, spray pyrolysis, screen printing, and so forth [1, 7, 11–18]. Wet chemical techniques offer easy way for homogeneous doping of virtually any element in any proportion by merely adding it in some form of cationic solution. Moreover, these techniques do not require high quality targets and/or substrates which are unavoidable in sputtering and PLD. SILAR does not involve high temperatures allowing employment of polymers as substrates. Besides, sol-gel spin coating is a time saving process; however, it is difficult to precisely control the thickness of the films. In spray pyrolysis, oxides can be readily obtained by thermal decomposition of organometallic precursor solution during its spraying on adequately heated substrate responsible for good quality films. Thickness of the film as well as the deposition rate can be controlled over a wide range by changing the spray parameters. Also large area deposition can be done using this method. Local overheating leading to degradation of film does not occur here which is generally a matter of concern in radio frequency magnetron sputtering due to involvement of high power sources [19].

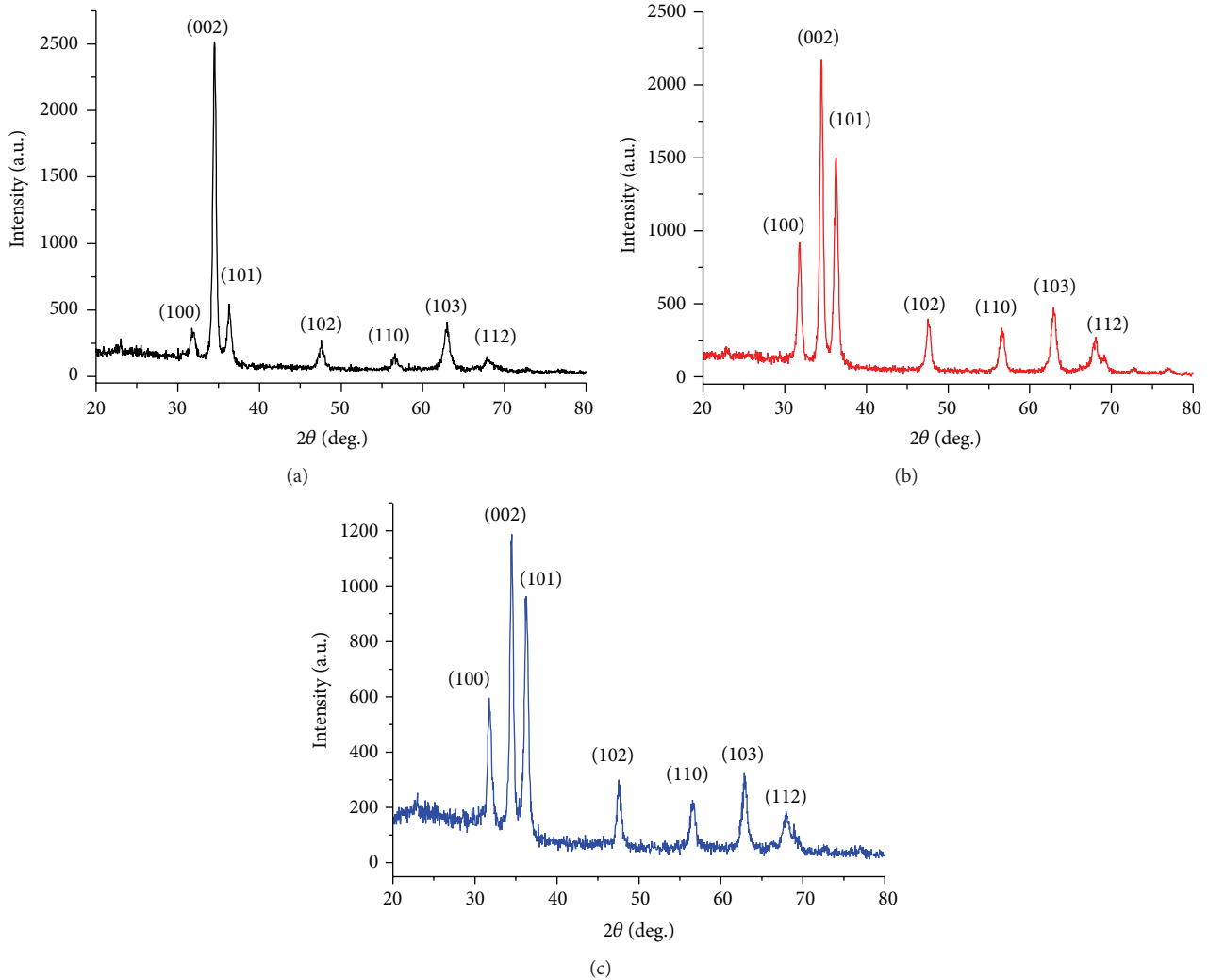


FIGURE 1: XRD pattern of undoped and Cu doped ZnO thin films sample. Here (a), (b), and (c) correspond to samples Z1, Z1C1, and Z1C2, respectively, prepared using precursor solution of molarity of 0.1 M.

In this paper, structural, optical, and morphological property of undoped and Cu doped ZnO thin films prepared by spray pyrolysis along with CO₂ sensing [20] has been presented.

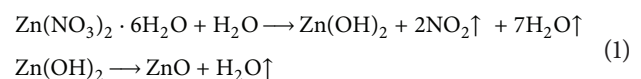
2. Experimental

The precursor for undoped films is prepared by obtaining 0.1 and 0.15 M solutions of zinc nitrate (99.9% pure, S D Fine Chem. Ltd.) in deionized water. The mixture is magnetically stirred at 60°C for 30 min to get homogeneous solution. To this solution, appropriate volumes of 0.1 and 0.15 M solutions of cupric chloride in deionized water are added to obtain 1 and 2 at.% doping of Cu. These solutions are again stirred for 30 min. Both the undoped and doped solutions are aged for 15 days for obtaining stability.

The experimental set-up contains glass atomizer for spraying the precursor solution. The substrates are kept on

hot iron plate which is attached with thermocouple and temperature controller to maintain the required temperature. The precursor solution is introduced in the container connected to the liquid inlet of the atomizer by a tube having solution flow controller and the compressed air used as carrier gas is let into the gas inlet of the atomizer [17].

For deposition of thin film, 10 mL of the precursor solution of each sample, one at a time, is transferred to the container. The distance between nozzle and the substrate is set at 25 cm and the flow rate is set at 10 mL/min. The substrate temperature was maintained at 400°C to obtain good quality films in addition to thermal decomposition of zinc nitrate. Reactions occurring during deposition are as follows:



Postdeposition annealing of the films is done at 400°C for 30 minutes. These six samples, undoped ZnO, ZnO: 1 at.%

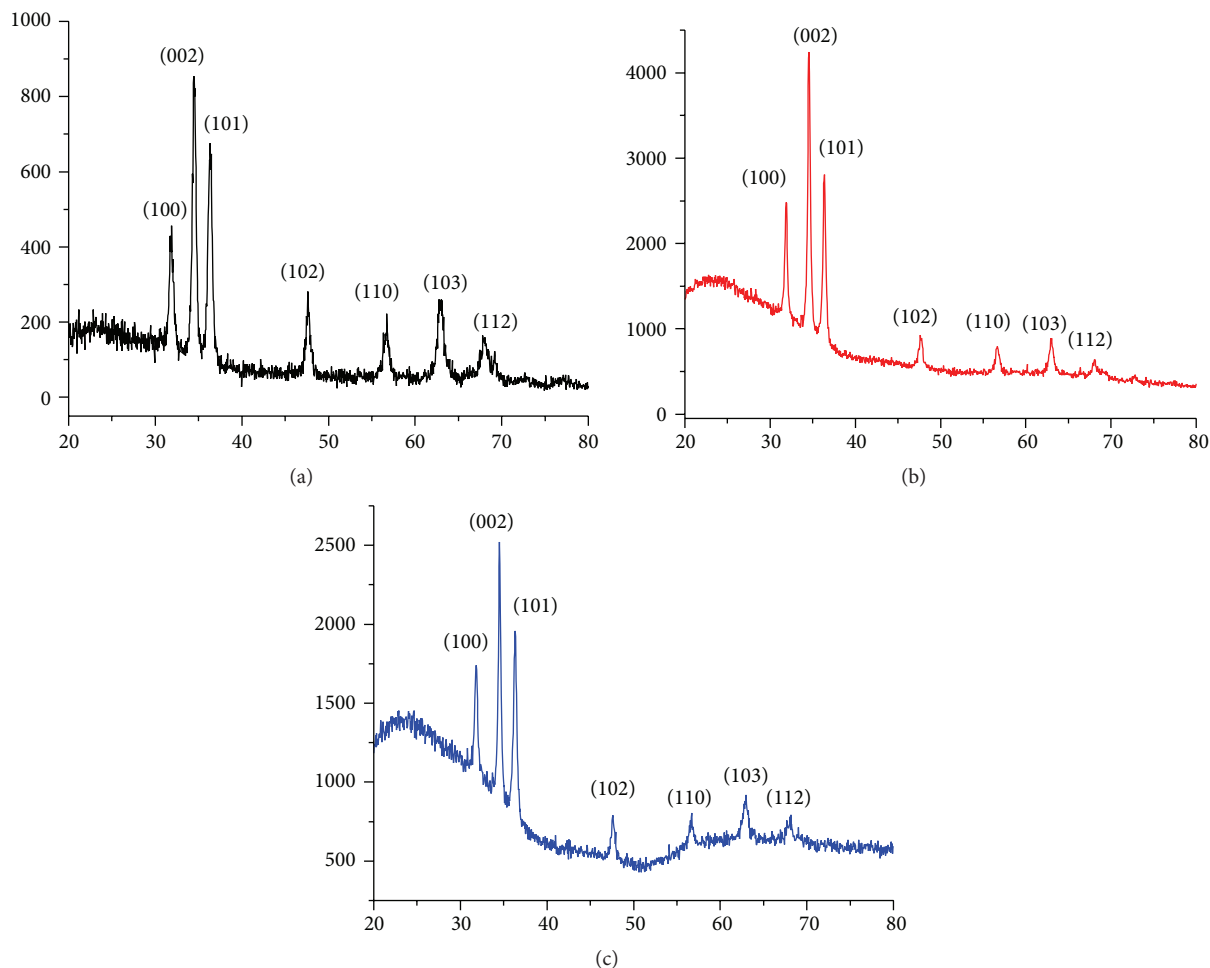


FIGURE 2: XRD pattern of undoped and Cu doped ZnO thin films sample. Here (a), (b), and (c) correspond to samples Z2, Z2C1, and Z2C2, respectively, prepared using precursor solution of molarity of 0.15 M.

Cu and ZnO:2 at.% Cu using 0.1 M and 0.15 M precursor solutions, are named as Z1, Z1C1, and Z1C2 and Z2, Z2C1, and Z2C2, respectively. Deposition parameters have been strictly kept the same to obtain films of approximately similar thickness.

The crystal phase and crystallinity of the samples have been investigated using X-ray diffractometer (Bruker D8 Advance X-ray diffractometer) for 2θ values ranging from 20 to 80° using $\text{CuK}\alpha$ radiation ($\lambda = 0.154 \text{ nm}$). Transmittance spectra have been recorded using UV-Vis spectrophotometer (model number 108 Make-Systronics). Surface morphology is obtained using FESEM (ZEISS) and film thickness is determined by XP-1 stylus profiler (Ambios Technology).

3. Characterization

3.1. X-Ray Diffraction. The X-ray diffraction patterns for samples Z1, Z1C1, and Z1C2 are shown in Figure 1 and for samples Z2, Z2C1, and Z2C2 are shown in Figure 2. All the samples exhibit hexagonal wurtzite structure of ZnO showing preferred orientations along (100), (002), and (101)

[1, 15, 21–23]. The peak along c -axis, that is, (002) plane, occurs at $2\theta = 34.50, 34.54^\circ$, and 34.47° for samples Z1, Z1C1, and Z1C2, respectively. The diffraction peak shifts to higher value for Z1C1 and back to lower value of 2θ for sample Z1C2. This indicates that initially Cu substitutes Zn and with increasing concentration of Cu it goes into interstitial position. For samples Z2, Z2C1, and Z2C2, $2\theta = 34.46^\circ, 34.50^\circ$, and 34.50° , respectively. The diffraction peak shifts to higher value as dopant is introduced and remains unaffected thereafter. Diffraction peak except those for ZnO is not found for any of the samples, indicating absence of any impurity phase. Crystallite size along (002) crystallographic plane for these samples, as calculated by Debye Scherer formula, lies between 10 and 21 nm, Table 1. The orientation parameter $\gamma_{(hkl)} = (I_{(hkl)} / \sum I_{(hkl)})$ [1], Table 1, varies from 0.127 to 0.772 indicating dominant orientation along (002) plane.

3.2. UV-Visible Spectra and Optical Band Gap. The transmittance spectra of samples prepared using precursor solutions of molarities 0.1 M and 0.15 M are shown in Figures 3 and 4, respectively. The transmittance of samples Z1, Z1C1, and

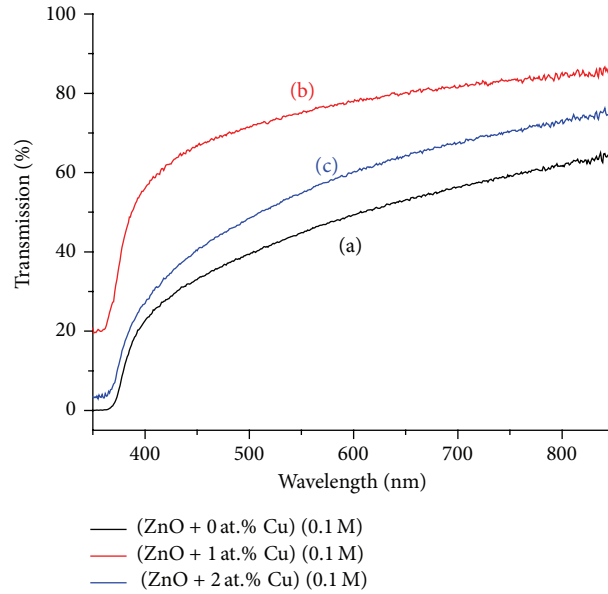


FIGURE 3: Transmission spectra of undoped and Cu doped ZnO thin films sample. Here (a), (b), and (c) correspond to samples Z1, Z1C1, and Z1C2, respectively, prepared using precursor solution of molarity of 0.1 M.

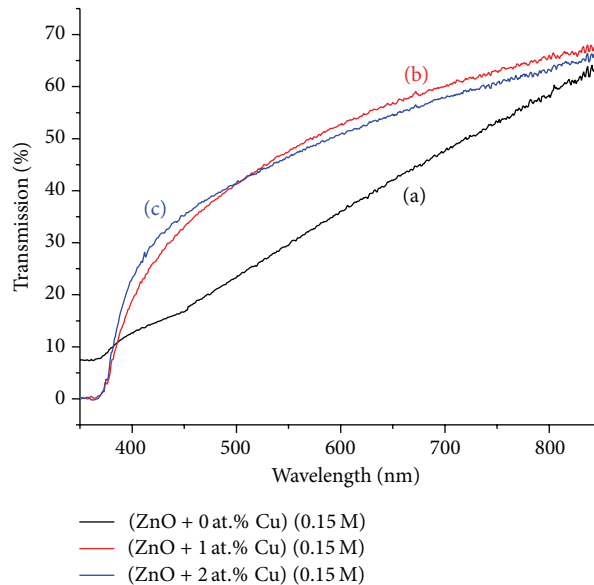


FIGURE 4: Transmission spectra of undoped and Cu doped ZnO thin films sample. Here (a), (b), and (c) correspond to samples Z2, Z2C1, and Z2C2, respectively, prepared using precursor solution of molarity of 0.15 M.

Z1C2 increases gradually up to 87% over the range of 350 to 850 nm, Figure 3. The maximum transmittance for samples Z2, Z2C1, and Z2C2 is nearly 69% at 847 nm. Undoped film of lower molarity is more transparent at optical wavelengths, whereas around 800 nm both of the undoped films have similar transmittance. High transmittance indicates that the obtained films are of low impurities and have only few lattice defects [24]. Doped films are comparatively more transparent. In general, the transmittance is found to decrease

with an increase in molarity of the precursor solution as expected. The decrease in transmittance may be due to free carrier absorption of photons [25].

The thickness of 0.1 M samples Z1, Z1C1, and Z1C2 is 1080, 1100, and 1050 nm, respectively. For 0.15 M samples Z2, Z2C1, and Z2C2, the thickness is 1120, 1090, and 1100 nm, respectively. The optical band gap of the films determined by Tauc's plot is found to vary over a range of 3.18 to 3.28 eV, Table 2. The variation in

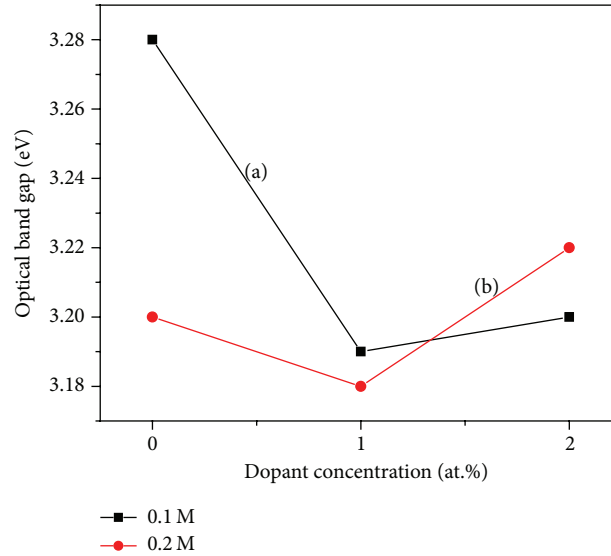


FIGURE 5: The variation in band gap (a) and (b) corresponds to the sample prepared using precursor solution of molarity of 0.1 and 0.15 M, respectively.

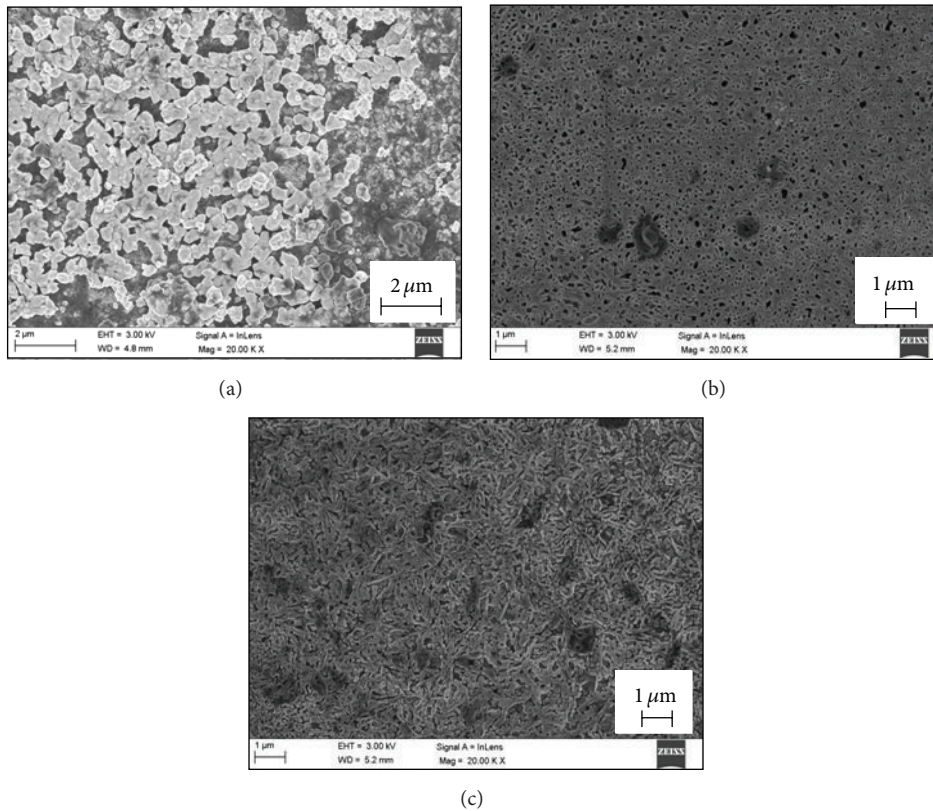


FIGURE 6: SEM of undoped and Cu doped ZnO thin films prepared using precursor solution of molarity of 0.1 M. Here (a), (b), and (c) correspond to samples Z1, Z1C1, and Z1C2, respectively.

band gap due to doping and molar concentration is shown in Figure 5. For undoped ZnO, the band gap decreases with increase in molarity of the precursor solution.

3.3. Surface Morphology. The scanning electron micrographs (SEM) for the three samples corresponding to 0.1 M molarity are shown in Figure 6. Sample Z1, that is, undoped ZnO of molarity 0.1 M, has flakes-like structures connected to each

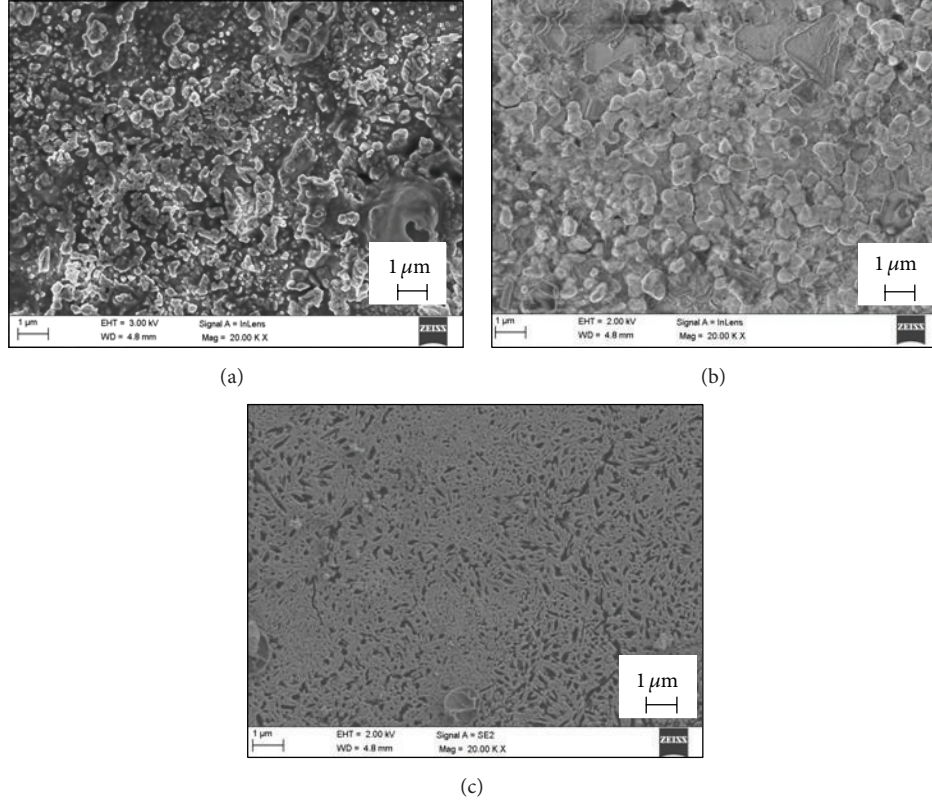


FIGURE 7: SEM of undoped and Cu doped ZnO thin films prepared using precursor solution of molarity of 0.15 M. Here (a), (b), and (c) correspond to samples Z2, Z2C1, and Z2C2, respectively.

TABLE 1: Crystallite size (t_{DS}) and orientation parameter (γ) of all the samples.

Samples	t_{DS} (nm) (002)	Orientation parameter ($\gamma_{(hkl)}$)		
		(100)	(002)	(101)
Z1	21	0.141	0.772	0.156
Z1C1	12	0.170	0.433	0.271
Z1C2	20	0.352	0.350	0.530
Z2	10	0.127	0.340	0.258
Z2C1	15	0.147	0.374	0.253
Z2C2	15	0.145	0.375	0.253

TABLE 2: Optical band gap of Cu doped ZnO thin films.

Sample	Composition	Optical band gap (eV)
Z1	0.1 M ZnO	3.28
Z1C1	0.1 M ZnO + 1% CuCl ₂	3.19
Z1C2	0.1 M ZnO + 2% CuCl ₂	3.20
Z2	0.15 M ZnO	3.20
Z2C1	0.15 M ZnO + 1% CuCl ₂	3.18
Z2C2	0.15 M ZnO + 2% CuCl ₂	3.22

other to form bigger ones (Figure 6(a)). As the dopant Cu is introduced in 1at.% in ZnO (sample Z1C1) film surface becomes netted with clear appearances of holes (Figure 6(b))

and for further increased doping of 2 at.% the net making needle-like structures become dominant over the holes (Figure 6(c)).

Surface morphology of samples of molarity 0.15 M are shown in Figure 7. Sample Z2 has random structures spread throughout the surface. For sample Z2C1, these random structures convert in irregular shaped grains. A network of small needle-like structures is seen for Z2C2.

3.4. Gas Sensing. For a semiconductor gas sensor, where resistance varies with gas concentration, the sensitivity S is defined as percent ratio of the resistance of the sensing film in air (R_{air}) to the resistance in the presence of the gas (R_{gas}) [26] at a particular temperature; that is,

$$S(\%) = \left(\frac{R_{air}}{R_{gas}} \right) \times 100. \quad (2)$$

For each concentration of analyte gas, which in the present case is CO₂, the temperature of the films is varied from 200 to 450°C in steps of 50°C and observations are taken. Before introducing the gas, sensing film is allowed to stabilize to ensure fixed initial reading for gas sensing application [27].

Figures 8 and 9 show the effect of temperature on the sensitivity of undoped and copper doped ZnO thin films for four different carbon dioxide concentrations.

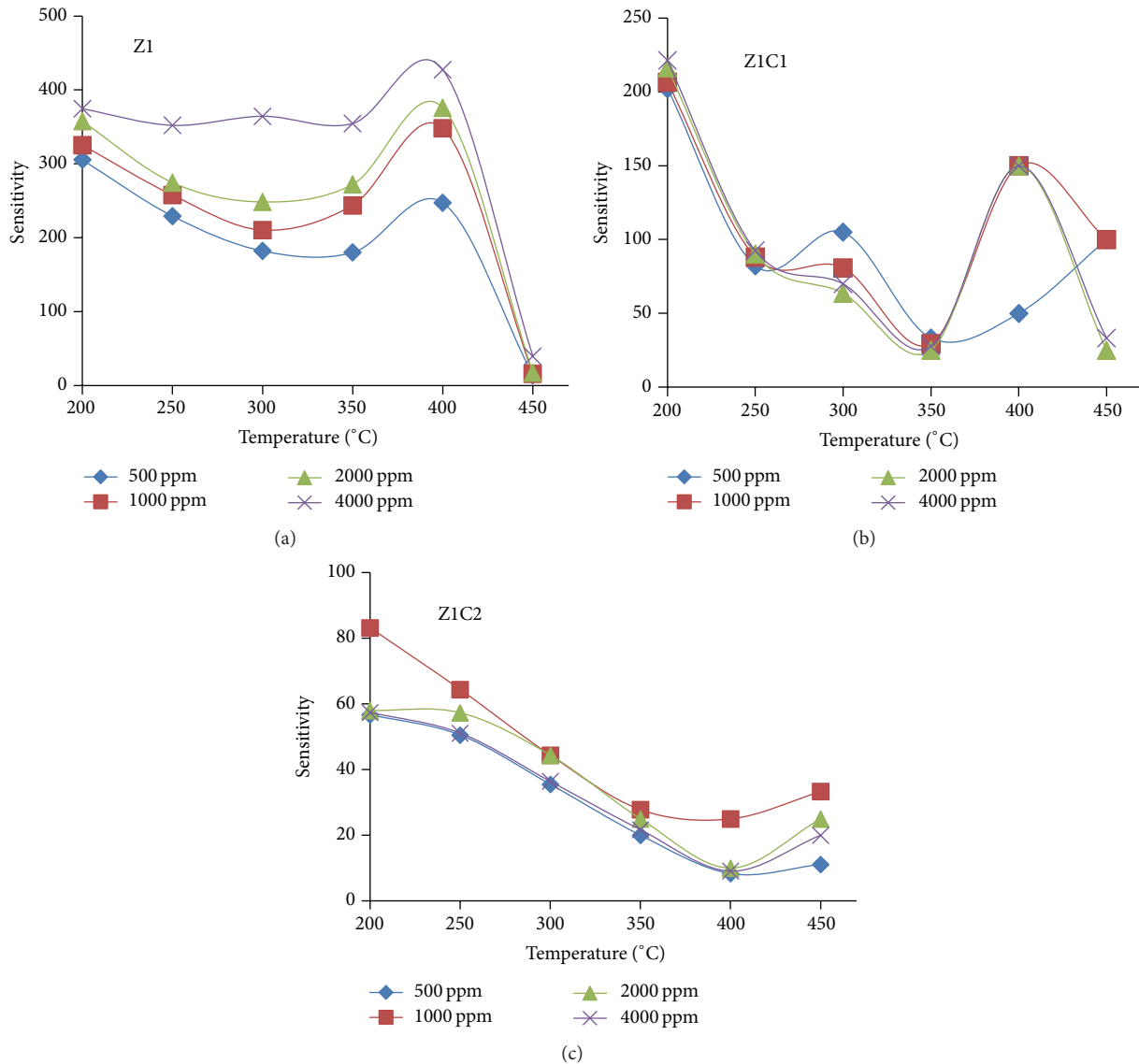


FIGURE 8: Variation of sensitivity of undoped and Cu doped ZnO thin film samples at various CO₂ concentrations with temperature. Here (a), (b), and (c) correspond to samples Z1, Z1C1, and Z1C2, respectively, prepared using precursor solution of molarity of 0.1 M.

For sample Z1, sensitivity is maximum at 400°C for all concentrations of CO₂ and the sensitivity increases with increase in concentration of CO₂. For sample Z1C1, the sensitivity is again maximum at 400°C except for 500 ppm concentration whereas for sample Z1C2 the sensitivity is minimum at 400°C and maximum at 200°C. Such behavior can be attributed to the changing surface morphology of samples (Figure 8).

For sample Z2, maximum sensitivity occurs below 300°C whereas for sample Z2C1 maxima occur at 300°C. For sample Z2C2, again the sensitivity is maximum at lower temperature. It is seen that presence of more and more dopant decreases the sensitivity of the films towards carbon dioxide.

The variation in sensitivity with temperature for 500, 1000, 2000, and 4000 ppm of CO₂ concentration is shown in Figures 10(a), 10(b), 10(c) and 10(d) respectively.

The sensitivity has high value at 200°C for samples Z1C1 and Z1C2 at all gas concentrations. However, sample Z1C2 has maximum sensitivity for 1000 ppm at 200°C. An increase in temperature decreases the sensitivity in both these samples whereas for samples Z2C1 and Z2C2 the sensitivity has low value at low operating temperature. Sample Z2C1 has maximum sensitivity at 300°C for 500 ppm. Sample Z2C2 has maximum sensitivity at 250°C for 2000 ppm.

Band theory as applied to gas sensors has been the subject of intense study for a number of years [28, 29]. The analyte carbon dioxide gas interacts with the surface of the metal oxide film (generally through surface adsorbed oxygen ions), which results in a change in charge carrier concentration [30] altering the conductivity (or resistivity) of the material. An n-type semiconductor is one where the majority charge carriers are electrons, and upon interaction with a reducing gas an

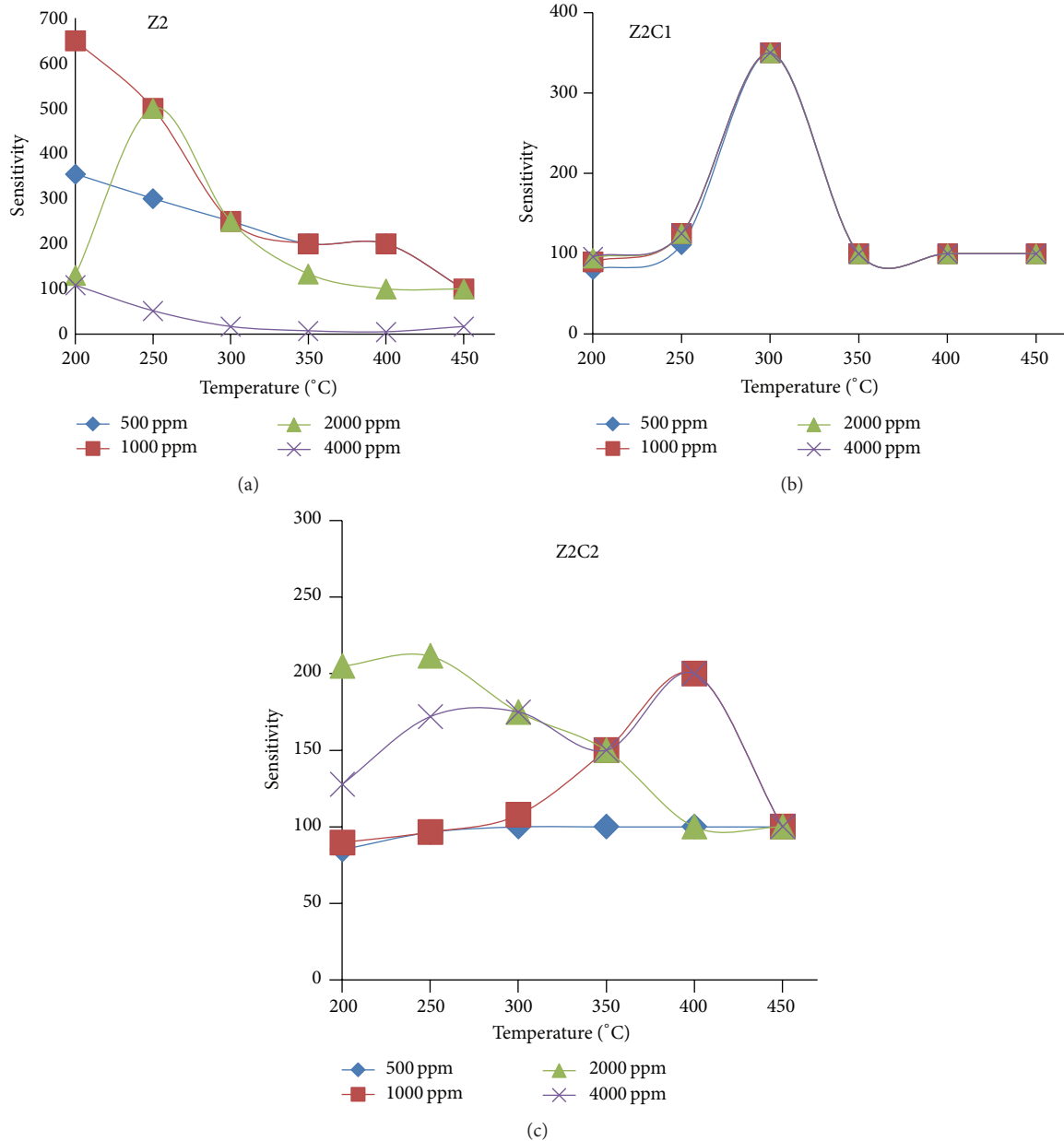


FIGURE 9: Variation of sensitivity of undoped and Cu doped ZnO thin film samples at various CO₂ concentrations with temperature. Here (a), (b), and (c) correspond to samples Z2, Z2C1, and Z2C2, respectively, prepared using precursor solution of molarity 0.15 M.

increase in conductivity occurs. However, change in charge carrier concentration in the sample also depends upon the amount of the adsorbed gas which in turn depends on the surface morphology. Thus, the nature of the analyte gas and the surface morphology of the films both should be taken into account while comparing the resistance, R_{gas} , of a sample in presence of varying concentration of the gas.

4. Conclusions

Nanocrystalline Cu doped ZnO films have been successfully deposited on glass substrates by spray pyrolysis and their structural and optical properties have been investigated.

The crystallite size decreases with increase in molarity of precursor solution whereas with doping the crystallite size increases in general. Doping increases the transmittance of the films whereas optical band gap first decreases and then increases as the dopant concentration is gradually increased for both molarities in reference. As the doping increases, the SEM shows formation of irregular shaped grains and then netted structure with holes followed by net making needle-like structures becoming dominant over the holes for both molarities. Response of these films for carbon dioxide has been studied. Undoped ZnO shows maximum sensitivity at 400°C for higher concentration of CO₂. The sensitivity of Cu doped sample is

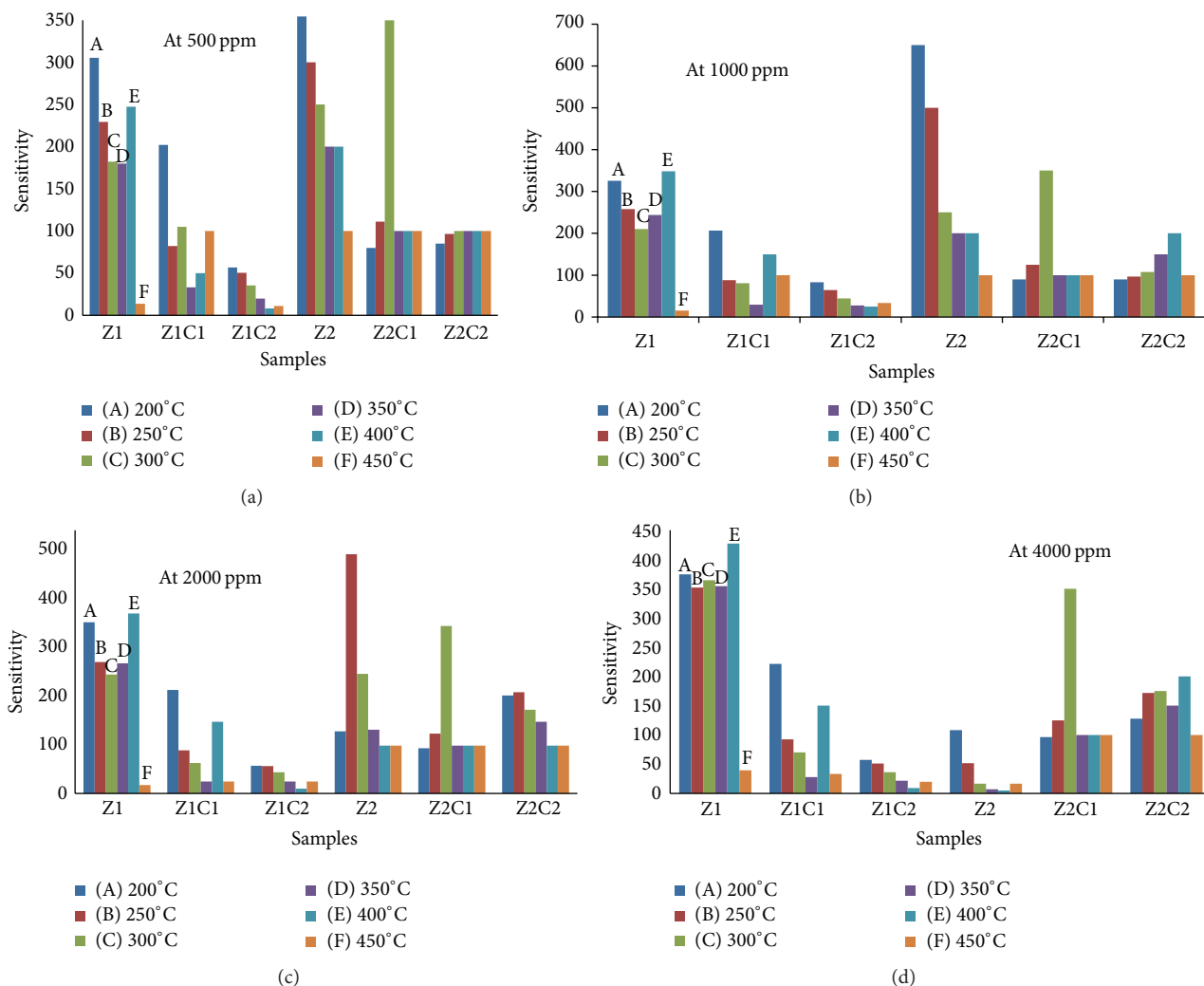


FIGURE 10: (a) Variation of sensitivity of undoped and Cu doped ZnO thin film samples at 500 ppm CO₂ concentration with temperature. (b) Variation of sensitivity of undoped and Cu doped ZnO thin films sample at 1000 ppm CO₂ concentrations with temperature. (c) Variation of sensitivity of undoped and Cu doped ZnO thin films sample at 2000 ppm CO₂ concentrations with temperature. (d) Variation of sensitivity of undoped and Cu doped ZnO thin film samples at 4000 ppm CO₂ concentration with temperature.

maximum at 200°C for all CO₂ concentrations from 500 to 4000 ppm.

Conflict of Interests

The authors declare that there is no conflict of interests regarding the publication of this paper.

References

- [1] A. K. Das, P. Misra, and L. M. Kukreja, "Effect of Si doping on electrical and optical properties of ZnO thin films grown by sequential pulsed laser deposition," *Journal of Physics D: Applied Physics*, vol. 42, no. 16, Article ID 165405, 2009.
- [2] S. Y. Pung, C. S. Ong, K. Mohd Isha, and M. H. Othman, "Synthesis and characterization of Cu-doped zno nanorods," *Sains Malaysiana*, vol. 43, no. 2, pp. 273–281, 2014.
- [3] B. Allabergenov, O. Tursunkulov, A. I. Abidov, B. Choi, J. S. Wook, and S. Kim, "Microstructural analysis and optical characteristics of Cu-doped ZnO thin films prepared by DC magnetron sputtering," *Journal of Crystal Growth*, vol. 401, pp. 573–576, 2014.
- [4] Y.-Q. Bie, Z.-M. Liao, P.-W. Wang et al., "Single ZnO nanowire/p-type GaN heterojunctions for photovoltaic devices and UV light-emitting diodes," *Advanced Materials*, vol. 22, no. 38, pp. 4284–4287, 2010.
- [5] P. S. Shewale, V. B. Patil, S. W. Shin, J. H. Kim, and M. D. Uplane, "H₂S gas sensing properties of nanocrystalline Cu-doped ZnO thin films prepared by advanced spray pyrolysis," *Sensors and Actuators B: Chemical*, vol. 186, pp. 226–234, 2013.
- [6] A. T. Marin, D. Muñoz-Rojas, D. C. Iza, T. Gershon, K. P. Musselman, and J. L. MacManus-Driscoll, "Novel atmospheric growth technique to improve both light absorption and charge collection in ZnO/Cu₂O thin film solar cells," *Advanced Functional Materials*, vol. 23, no. 27, pp. 3413–3419, 2013.

- [7] J.-H. Jeon, S.-Y. Jeong, C.-R. Cho et al., "Heteroepitaxial relation and optical properties of Cu-doped ZnO films grown by using pulsed laser deposition," *Journal of the Korean Physical Society*, vol. 54, no. 2, pp. 858–862, 2009.
- [8] M. Bedir, M. Öztas, A. N. Yazici, and E. V. Kafadar, "Characterization of undoped and Cu-doped ZnO thin films deposited on glass substrates by spray pyrolysis," *Chinese Physics Letters*, vol. 23, no. 4, pp. 939–942, 2006.
- [9] M. B. Rahmani, S. H. Keshmiri, M. Shafiei et al., "Transition from n- to p-type of spray pyrolysis deposited Cu doped ZnO thin films for NO₂ sensing," *Sensor Letters*, vol. 7, no. 4, pp. 621–628, 2009.
- [10] S. Dixit, A. Srivastava, A. Srivastava, and R. K. Shukla, "Effect of toxic gases on humidity sensing property of nanocrystalline ZnO film," *Journal of Applied Physics*, vol. 102, no. 11, Article ID 113114, 2007.
- [11] B. Allabergenov, S.-H. Chung, S. M. Jeong, S. Kim, and B. Choi, "Enhanced blue photoluminescence realized by copper diffusion doping of ZnO thin films," *Optical Materials Express*, vol. 3, no. 10, pp. 1733–1741, 2013.
- [12] K. P. Misra, R. K. Shukla, A. Srivastava, and A. Srivastava, "Blueshift in optical band gap in nanocrystalline Zn_{1-x}Ca_xO films deposited by sol-gel method," *Applied Physics Letters*, vol. 95, no. 3, Article ID 031901, 2009.
- [13] C.-H. Hsu, L.-C. Chen, and X. Zhang, "Effect of the CU source on optical properties of CuZnO films deposited by ultrasonic spraying," *Materials*, vol. 7, no. 2, pp. 1261–1270, 2014.
- [14] C. Wang, Z. Chen, Y. He, L. Li, and D. Zhang, "Structure, morphology and properties of Fe-doped ZnO films prepared by facing-target magnetron sputtering system," *Applied Surface Science*, vol. 255, no. 15, pp. 6881–6887, 2009.
- [15] V. S. Kalyamwar, F. C. Raghuvanshi, N. L. Jadhao, and A. J. Gadewar, "Zinc oxide nanostructure thick films as H₂S gas sensors at room temperature," *Journal of Sensor Technology*, vol. 3, no. 3, pp. 31–35, 2013.
- [16] F. K. Shan, B. I. Kim, G. X. Liu et al., "Blue shift of near band edge emission in Mg doped ZnO thin films and aging," *Journal of Applied Physics*, vol. 95, no. 9, pp. 4772–4776, 2004.
- [17] D. Mishra, A. Srivastava, A. Srivastava, and R. K. Shukla, "Bead structured nanocrystalline ZnO thin films: synthesis and LPG sensing properties," *Applied Surface Science*, vol. 255, no. 5, pp. 2947–2950, 2008.
- [18] G. Shanmuganathan and I. B. Shameem Banu, "Influence of codoping on the optical properties of ZnO thin films synthesized on glass substrate by chemical bath deposition method," *Advances in Condensed Matter Physics*, vol. 2014, Article ID 761960, 9 pages, 2014.
- [19] P. S. Patil, "Versatility of chemical spray pyrolysis technique," *Materials Chemistry and Physics*, vol. 59, no. 3, pp. 185–198, 1999.
- [20] P. Samarasekara, N. U. S. Yapa, N. T. R. N. Kumara, and M. V. K. Perera, "CO₂ gas sensitivity of sputtered zinc oxide thin films," *Bulletin of Materials Science*, vol. 30, no. 2, pp. 113–116, 2007.
- [21] T. M. Hammad, J. K. Salem, R. G. Harrison, R. Hempelmann, and N. K. Hejazy, "Optical and magnetic properties of Cu-doped ZnO nanoparticles," *Journal of Materials Science: Materials in Electronics*, vol. 24, no. 8, pp. 2846–2852, 2013.
- [22] G.-H. Zhang, X.-Y. Deng, H. Xue, and G. Xiang, "Engineering of electronic and optical properties of ZnO thin films via Cu doping," *Chinese Physics B*, vol. 22, no. 4, Article ID 047803, 2013.
- [23] A. Srivastava, N. Kumar, K. P. Misra, and S. Khare, "Blue-light luminescence enhancement and increased band gap from calcium-doped zinc oxide nanoparticle films," *Materials Science in Semiconductor Processing*, vol. 26, no. 1, pp. 259–266, 2014.
- [24] A. Ashour, M. A. Kaid, N. Z. El-Sayed, and A. A. Ibrahim, "Physical properties of ZnO thin films deposited by spray pyrolysis technique," *Applied Surface Science*, vol. 252, no. 22, pp. 7844–7848, 2006.
- [25] J. P. Upadhyay, S. R. Vishwakarma, and H. C. Prasad, "Studies of electrical and optical properties of SnO₂:P films," *Thin Solid Films*, vol. 169, no. 2, pp. 195–204, 1989.
- [26] R. S. Khadayate, R. B. Waghulde, M. G. Wankhede, J. V. Sali, and P. P. Patil, "Ethanol vapour sensing properties of screen printed WO₃ thick films," *Bulletin of Materials Science*, vol. 30, no. 2, pp. 129–133, 2007.
- [27] P. Mitra, A. P. Chatterjee, and H. S. Maiti, "ZnO thin film sensor," *Materials Letters*, vol. 35, no. 1-2, pp. 33–38, 1998.
- [28] N. Yamazoe, J. Fuchigami, M. O. Kishikawa, and T. Seiyama, "Interactions of tin oxide surface with O₂, H₂O and H₂," *Surface Science*, vol. 86, pp. 335–344, 1979.
- [29] N. Barsan, M. Schweizer-Berberich, and W. Göpel, "Fundamental and practical aspects in the design of nanoscaled SnO₂ gas sensors: a status report," *Fresenius' Journal of Analytical Chemistry*, vol. 365, no. 4, pp. 287–304, 1999.
- [30] N. Bârsan and U. Weimar, "Understanding the fundamental principles of metal oxide based gas sensors; the example of CO sensing with SnO₂ sensors in the presence of humidity," *Journal of Physics: Condensed Matter*, vol. 15, no. 20, pp. R813–R839, 2003.